Dynamical System Approach to the Potential Intensity of Tropical Cyclones

Dissertation

Zur Erlangung des Doktorgrades der Naturwissenschaften
an der Fakultät für
Mathematik, Informatik und Naturwissenschaften

Fachbereich Geowissenschaften
der Universität Hamburg

vorgelegt von
Daria Schönemann
aus
Berlin

Hamburg, 2014

Eidesstattliche Versicherung

Hiermit erkläre ich an Eides statt, dass ich die vorliegende Dissertationsschrift selbst verfasst und keine anderen als die angegebenen Quellen und Hilfsmittel benutzt habe.

Daria Schönemann

Kurzfassung

Das dynamische Systemverhalten tropischer Zyklone und ihrer potentiellen Intensität wird im Hinblick auf einige klimatologische Parameter mittels eines konzeptionellen Modells, sowie innerhalb des hochauflösenden Wolkenmodells HURMOD untersucht. Beide Modelle weisen Verzweigungen, oder sogenannte Bifurkationspunkte auf, an denen eine plötzliche Änderung der Intensität der tropischen Zyklone durch Vorgabe einer infinitesimal kleinen Änderung in der Ozeanoberflächentemperatur eintritt. Die Art der Verzweigungen, die im jeweiligen Modell auftreten, unterscheiden sich voneinander, wohingegen das Verhalten der Änderung bzw. Verschiebung von Bifurkationspunkten unter veränderten thermodynamischen Bedingungen in beiden Modellen qualitativ sehr ähnlich ist. Weiterhin stimmen die Modelle in Hinblick auf die Tendenzen der Änderung der potentiellen Intensiät in Abhängigkeit von den untersuchten Parametern weitgehend überein.

Im konzeptionellen Modell wird die tropische Zyklone in drei Regionen unterteilt, das Auge, den Augenwall und die Umgebungsregion. Das Modell stellt ein dynamisches System dar, welches durch drei gewöhnliche Differentialgleichungen beschrieben wird. Für Parametereinstellungen, die in etwa Bedingungenen über tropischen Ozeanen entsprechen, besitzt das System bis zu vier nicht-triviale stationäre Lösungen. Zwei dieser Lösungen sind mit einem stabilen und die anderen zwei mit einem instabilen Gleichgewichtszustand verbunden. Verzweigungsdiagramme liefern eine Erklärung dafür, weshalb sich bei Ozeanoblerflächentemperaturen, die unterhalb eines kritischen Wertes liegen, nur Anfangsstörungen oberhalb einer gewissen Amplitude zu Wirbelstürmen mit der Stärke tropischer Orkane ausbilden können. Neben der Ozeanoberflächentemperatur stellt die relative Feuchte der Umgebungsregion einen wichtigen Modellparameter dar, da diese Größe das Einströmen von Luft mit niedriger Entropie in die Zustromschicht der tropischen Zyklone stark beeinflusst. Die Flächen, durch die die Gleichgewichtszustände im Verzweigungsdiagramm als Funktion der Ozeanoberflächentemperatur und der relativen Feuchte beschrieben sind, legen die Existenz einer Spitzenkatastrophe offen. Am Katastrophenpunkt spaltet sich das stabile der beiden Gleichgewichte in drei Gleichgewichte auf. Innerhalb des Modellregimes, in dem vier Gleichgewichtslösungen existieren, wird die Zyklogenese aufgrund der jeweils abstoßenden und anziehenden Wirkung der beiden zusätzlichen Gleichgewichte sehr unwahrscheinlich.

In Übereinstimmung mit dem konzeptionellen Modell, deuten die Ergebnisse der HURMOD-Simulationen auf die Existenz eines Fixpunktattraktors hin, der mit einem starken tropischen Wirbelsturm assoziiert ist. Außerdem stellt die Stärke der Anfangsstörung eine Amplitudenschwelle bezüglich der Zyklogenese dar. Oberhalb dieser Schwelle sind Ausdehnung, gemessen am Radius des Maximalwindes, sowie Intensität der Modellzyklone im ausgreiften Stadium unabhängig von der Stärke und horizontalen Ausdehnung der Anfangsstörung. Unterhalb der Amplitudenschwelle kommt es nicht zur Zyklogenese und das System strebt einem atmosphärischen Ruhezustand entgegen. Unter Voraussetzung einer fortwährenden feucht-neutralen Relaxation der Troposphäre weist der tropische Wirbelsturm im Modell keine Änderung seines dynamischen Verhaltens im Bereich tropischer Ozeanoberflächentemperaturen auf, d.h. es existieren keine Verzweigungen und die tropische Zyklone schwächt sich lediglich mit abnehmender Ozeanoberflächentemperatur ab. Dies liegt in Übereinstimmung mit den Ergebnissen einer feucht-neutralen Konfiguration des konzeptionellen Modells. Im Falle der Annahme, dass die troposphärische Schichtung vom feucht-neutralen Zustand abweicht, zeigen die HURMOD-Ergebnisse die Existenz von Bifurkationen in Verbindung mit Änderungen in der Ozeanoberflächentemperatur an: Mit abnehmender Ozeanoberflächentemperatur wird die Zyklone stetig schwächer, bis sich der Fixpunktattraktor entsprechend einer Hopf-Bifurkation zunächst in einen Grenzzyklus wandelt und dann in einen schwächeren stationären Zustand fällt, bis die Oszillationen der Intensität chaotisch werden und sich der tropische Wirbel schließlich auflöst.

In beiden Modellen sind sowohl die Amplitudenschwelle als auch der Ozeanoberflächentemperaturbereich, in dem das System Verzweigungspunkte aufweist, sensitiv gegenüber Veränderungen der relativen Feuchte und der troposphärischen Temperaturschichtung der Umgebung. Die Ergebnisee beider Modelle lassen darauf schließen, dass sich der Schwellenwert der Ozeanoberflächentemperatur, oberhalb dessen Stürme mit der Intensität tropischer Orkane auftreten können, mit zunehmender Tropopausentemperatur, abnehmendem vertikalen troposphärischen Temperaturgradienten, sowie abnehmendem Feuchtegehalt der Umgebungsluft hin zu höheren Werten verschiebt. Dieser Befund deutet darauf hin, dass der beobachtete Ozeanoberflächentemperaturschwellenwert vom Klimazustand abhängt. Es ist daher anzunehmen, dass sich der Schwellenwert unter globalem und regionalem Wandel des Klimas entsprechend verschiebt.

Abstract

The dynamical system behaviour of tropical cyclones and their potential intensity with view to several climatological parameters is investigated by means of a conceptual tropical cyclone model and within the axisymmetric high-resolution cloud model HURMOD. Both models possess bifurcation points, which are associated with a sudden change in tropical cyclone intensity towards an infinitesimal change in the prescribed sea surface temperature. The type of bifurcations, which occur in the respective model are different from each other, while the change-behaviour or shifting of bifurcation points in response to changes in the thermodynamic conditions is in good qualitative agreement among the two models. Moreover, the models are largely concordant with regard to the tendencies of potential intensity changes as a function of the parameters studied herein.

In the conceptual model, the tropical cyclone is divided into three regions, the eye, eyewall and ambient region. The model forms a low-order dynamical system of three ordinary differential equations. For tropical ocean parameter settings, the system possesses up to four non-trivial steady state solutions. Two steady states are unstable while the two remaining states are stable. Bifurcation diagrams provide an explanation why only finite-amplitude perturbations can transform into storms of tropical cyclone strength below a critical sea surface temperature. Besides sea surface temperature, relative humidity of the ambient region forms an important model parameter as it considerably affects the entrainment of low-entropy air into the inflow region of the tropical cyclone. The surfaces that describe equilibria as a function of sea surface temperature, and relative humidity reveal the existence of a cusp-catastrophe. At the catastrophe point the stable one of the two equilibria splits into three equilibria. Within the model regime of four equilibria, cyclogenesis becomes very unlikely due to the repelling and attracting effects of the two additional equilibria.

In accordance with the conceptual model, the results from HURMOD simulations exhibit the existence of a fixed point attractor associated with a strong tropical cyclone. Moreover, the initial vortex strength poses an amplitude threshold to cyclogenesis. Above this threshold, the size of the modelled tropical cyclone measured by the radius of maximum winds, and its intensity in the mature stage are independent of the initial vortex strength and its horizontal extent. Below the amplitude threshold, cyclogenesis does not occur and the system approaches an atmospheric state of rest. If the troposphere is relaxed to moist-neutral conditions, the dynamical behaviour of the

modelled tropical cyclone does not change within the range of tropical sea surface temperatures, i.e. there are no bifurcations and the tropical cyclone weakens only slightly with decreasing sea surface temperature. This is in agreement with the result from a moist-neutral configuration in the conceptual model. In case we presume a deviation of the tropospheric stratification from moist-neutral conditions, HURMOD results reveal the existence of bifurcations in association with changes in the sea surface temperature: With decreasing sea surface temperature, the tropical cyclone steadily weakens, until the fixed point attractor turns first into a limit cycle indicating a Hopf bifurcation, and then gives way to a lower steady state, before the intensity oscillation becomes chaotic, and finally the tropical storm dies off.

In both models, the amplitude threshold and the surface temperature range, within which the system exhibits bifurcation points, are sensitive to the environmental relative humidity and the tropospheric temperature stratification. The models' results infer that the value of the sea surface temperature threshold, above which storms of tropical cyclone intensity may occur, rises to higher values with increasing tropopause temperature; decreasing temperature lapse rate; and decreasing environmental moisture content. These findings indicate that the observed sea surface temperature threshold for cyclogenesis depends on the climate state, and thus can be expected to shift in response to global and regional climate change.

List of Abbreviations

CAPE .... Convective available potential energy
CISK .... Conditional instability of the second kind
LFC .... Level of free convection
lhs .... left hand side
LNB .... Level of neutral buoyancy
PI .... Potential intensity
PRMW .... Potential radius of maximum winds
rhs .... right hand side
RMGW .... Radius of maximum gradient winds
RMW .... Radius of maximum winds
SCAPE .... Slantwise convective available potential energy
SSHS .... Saffir-Simpson hurricane wind scale
SST .... Sea surface temperature
TC .... Tropical cyclone
WISHE .... Wind induced surface heat exchange

Contents

1 Introduction

1.1 Large-scale structure and flow-features of tropical cyclones

Tropical cyclones (TCs) are atmospheric low pressure systems characterised by deep convective clouds, which may reach a vertical extent of more than fifteen kilometres, spanning the entire troposphere. They form over tropical oceans as air spirals in from the surrounding region towards the low pressure core of the cyclone. In the core, a mature tropical cyclone of a certain strength develops a wall of clouds which encircles a relatively calm, warm and dry, cloud-free area characterised by slow subsidence, known as the eye. The region of deep convection, which surrounds the eye, is referred to simply as eyewall (Anthes, 1982). The motion within the eyewall updraft exhibits an outward component, so that the eyewall takes a shape similar to that of a funnel that tapers downward around the eye. At higher levels, near the top of the storm in the upper troposphere, the laterally outward motion becomes dominant, and therefore this part is often termed as the outflow layer of the TC. The outflow layer forms a dense cirrus shield, which covers an area of several hundred kilometres around the core (Frank, 1977). Within the outflow layer, the rotational sense of motion reverses, and the flow becomes anticyclonic.

Besides deep convection, which is associated with a high vertical wind velocity on the order of several metres per second, the eyewall is characterised by the highest tangential wind velocity that occurs throughout the entire domain of a TC. The horizontal flow usually reaches its maximum strength at the base of the eyewall at an altitude of a few hundred metres above the sea level. Outside the eyewall region, the tangential velocity decreases gradually with radial distance to the centre, and cloud activity is primarily confined to spiral rainbands, which form a non-axisymmetric feature within the, on the whole, approximately axisymmetric entity of a tropical cyclone. At a further radial distance a few hundred kilometres away from the core, and outward from the area of convective activity associated with spiral rainbands, convective motion largely abates and the mid-tropospheric flow shows, on average, a slight tendency to inward and downward-directed motion (Frank, 1977). Beyond this so-called moat region, mean-environmental conditions are approached. The large-scale flow can be subdivided into the primary (swirling or vortical) circulation, which represents the azimuthal flow; and the secondary (or toroidal) circulation, which comprises the radial and vertical flows (Ooyama, 1982; Wirth and Dunkerton, 2009). A vertically exaggerated cross-section through a TC and some of its flow characteristics described above is sketched in Fig. 1.1.
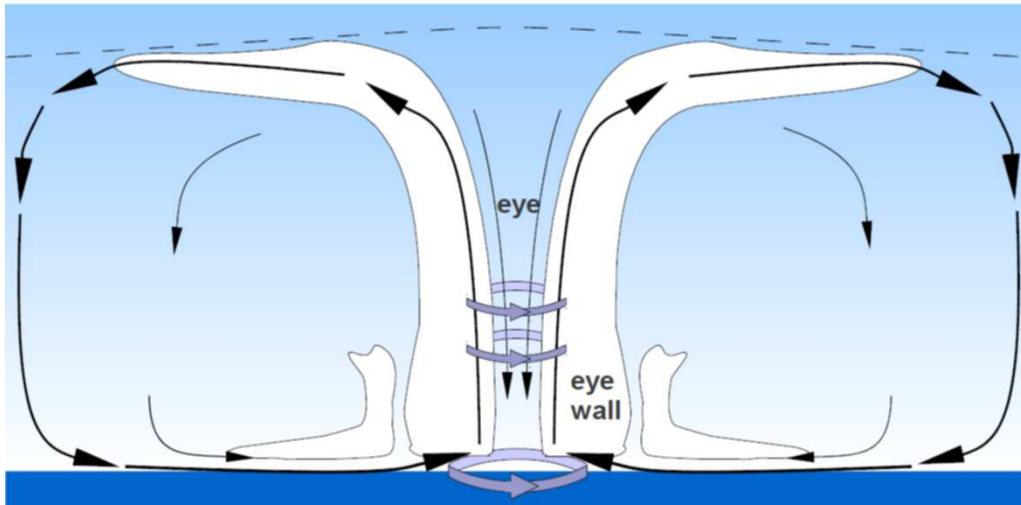
Figure 1.1: Vertically exaggerated, schematic representation of a tropical cyclone in the radial-vertical plane. The flow within the secondary circulation is represented by black arrows. The cyclonic primary flow within the eyewall region is sketched by purple filled arrows. Deep convection within the eyewall can reach up to the tropopause; inflow and outflow layers extend over a radial distance of several hundred kilometres.

1.2   Classification and climatology of tropical cyclones

Besides the generic definition given above, the term "tropical cyclone" is also used in a more specific sense to describe a low-pressure system, which displays a relatively high vortex strength or intensity in addition to the properties and features comprised by the generic definition. The square of either the maximum tangential velocity or, more generally, the maximum horizontal wind speed, serves as a measure for the intensity of a tropical cyclonic low-pressure system (Emanuel, 2003). TCs are commonly classified according to their maximum sustained wind speed, V_{smax}, into tropical depressions or non-developing cloud clusters ($V_{smax} < 17$ m/s), tropical storms (17 m/s $\leq V_{smax} < 33$ m/s), and tropical cyclones ($V_{smax} \geq 33$ m/s). Another frequently used measure of tropical cyclone intensity is their central minimum pressure. Results from both observational and modelling studies show that minimum pressure and maximum wind speed are closely correlated. Generally it is found that the higher the maximum wind speed, the lower the pressure in the core. The classification used by the National Hurricane Center (NHC)[1] of the USA follows the Saffir-Simpson hurricane wind scale (SSHWS or SSHS), which sorts tropical cyclones of hurricane strength into five categories on the basis of their maximum one-minute sustained wind speed. Note however that different meteorological agencies may use different tropical cyclone scales. For example, the Bureau of Meteorology, which is subordinate to the Australian government, classifies TCs according to their maximum ten-minute sustained wind speed, and does not

---

[1]http://www.nhc.noaa.gov/aboutsshws.php

distinguish between tropical storms and tropical cyclones in terms of intensity, but instead groups the TCs into tropical cyclones for maximum sustained wind speeds above 17 m/s, and severe tropical cyclones for 46 m/s $\leq V_{smax}$.[2] Up to now, the most intense, and also one of the most devastating TCs ever recorded at landfall was typhoon Haiyan (2013). Haiyan originated over Micronesia in the tropical Northwest Pacific and reached, according to estimates by the Joint Typhoon Warning center (JTWC), maximum one-minute sustained wind speeds of about 87.5 m/s.

Global records show that cyclogenesis is largely confined to tropical ocean regions with relatively warm surface waters. Moreover, TCs hardly ever form near the equator indicating that the Coriolis force is an important factor for cyclogenesis. The ocean basins, where TCs form on a regular basis are sketched in different colours in Fig. 1.2. The nomenclature of intense tropical cyclones also differs from region to region: in the North Atlantic and East Pacific basins TCs are referred to as hurricanes; in the Northwest Pacific as typhoons; in the North Indian Ocean as severe cyclonic storms; and in the other regions simply as tropical cyclones. Besides sufficiently warm temperatures in the ocean mixed-layer, and a non-zero Coriolis force, which is required for the spin-up of TCs, there are several other thermodynamic and dynamic factors that either favour or impede cyclogenesis. On the basis of extensive global observational studies of tropical cyclones, tropical storms and non-developing cyclonic disturbances (as defined by the SSHS), Gray (1979) outlined six climatological parameters, which may contribute to, whether a tropical cyclone develops or not. These genesis parameters, comprising the foregoing two, are: 1) low-level relative vorticity; 2) the Coriolis parameter; 3) the inverse magnitude of ventilation controlled by the environmental vertical shear of horizontal wind between the lower and upper troposphere; 4) ocean thermal energy as reflected by the sea surface temperature excess above 26°C in a layer of at least 60 m depth; 5) the vertical gradient of equivalent potential temperature in the lower and mid-troposphere as a criterion for convective instability; 6) environmental relative humidity at mid-tropospheric levels. As pointed out by Ooyama (1982), the synoptic and thermodynamic environmental conditions do not directly determine the process of cyclogenesis, but influence its probability, and in turn the frequency of occurrence of TCs.

Some climatological parameters affect both tropical cyclone intensity and their frequency of occurrence, such as environmental shear (Tang and Emanuel, 2012a), and, of course, the sea surface temperature (Holland, 1997; Mann and Emanuel, 2006; Ma et al., 2013). Though, there is observational evidence that the intensity and overall activity of TCs in response to changes in sea surface temperature (SST) exhibit a highly nonlocal character (Swanson,

---

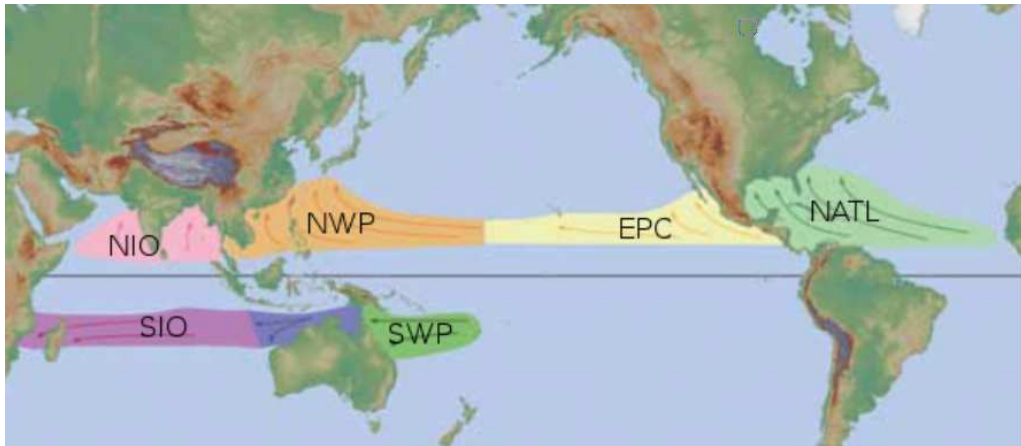[2]More information on intensity based classification and different scales for tropical cyclones can be found here: `http://www.bom.gov.au/cyclone/about/intensity.shtml`

Figure 1.2:   Tropical cyclone main development regions and mean tracks, with
kind permission of NOAA (`http://www.nhc.noaa.gov/climo/images/tcformation.png`,
`http://www.srh.noaa.gov/jetstream/tropics/tc_basins.htm`).   The thin grey line
marks the equator, and the acronyms stand for the major tropical cyclone formation basins
[cf. Table 2 in Yu et al. (2010)]: North Atlantic (NATL), Eastern Pacific (EPC), Northwest
Pacific (NWP), North Indian Ocean (NIO), South Indian Ocean (SIO), and Southwest Pa-
cific (SWP) basin. The Southeast Indian Ocean basin (coloured in dark-blue) is sometimes
considered separately from the SIO basin, and the NIO basin may be further subdivided
into the Bay of Bengal and the Arabian Sea basin [e.g. Gray (1968)].

2008). This means that seasonal tropical cyclone activity in a certain basin does not only
depend on local SST changes within the respective main development region but is corre-
lated to the relative SST (i.e. local minus tropical-mean SST), since the free-tropospheric
temperatures at higher levels tend to follow tropical-mean SSTs (Zhao et al., 2009; Yu et al.,
2010; Camargo et al., 2013). This indicates that besides sea surface temperature the tropo-
spheric temperature stratification, as well as upper-level tropospheric temperatures have a
considerable impact on tropical cyclone activity and intensity.

1.3   Motivation and outline

On the whole, the destructive power of storms rises with their sustained wind speeds and
associated strong wind gusts. Therefore, research on the theoretical maximum intensity of
TCs is clearly relevant, not the least for tropical cyclone hazard assessment. As pointed
out by Ooyama (1982), a tropical cyclone is a rather complex system, being a phenomenon
which involves multiscale motions, from cloud microphysics and turbulent mixing on the
microscale end, to general circulation patterns of the tropics on the macroscale end. To
quote Ooyama (1982) once again, its complete description would have to cover nearly all
subjects in meteorology. Though it is possible today to simulate TCs in numerical models
quite accurately, only little is known about their dynamical system characteristics. Moreover,

it remains an open question how tropical cyclones react to global warming.[3] Knowledge on the dynamical system properties of TCs is required to understand and judge the impact of changes in regional and global climate on their potential intensity (PI) and frequency of occurrence.

A notable characteristic of TCs is their longevity in comparison to other severe weather systems, such as tornadoes (Etling (2008), Chap. 15). The observation that a tropical cyclone, as a whole, forms a relatively stable system under favourable environmental conditions (Ooyama, 1982), gives rise to the conception of a tropical cyclone as an autonomous dynamical system. Though this certainly is an idealised view, it provides, in the first instance, a useful ansatz for the description of tropical cyclones by means of numerical modelling. On this basis, Emanuel and Nolan (2004) hypothesised that tropical cyclones can be understood as a stable branch occurring beyond a sub-critical saddle node bifurcation at a certain sea surface temperature. The other unstable branch after the bifurcation is associated with smaller but finite wind speeds that must be exceeded initially for tropical cyclogenesis to set in. This can possibly explain, why not all initial perturbations develop into TCs.

It remains to be further investigated, why such a bifurcation occurs and what physical processes are responsible for this. Tang and Emanuel (2010) have shown that entrainment of low-entropy air into the centre may represent an obstruction to TC formation and intensification. The low-entropy air entrainment in their model is prescribed in a way representative of what would occur in real storms due to vertical wind shear. Hence, their result may provide an explanation for the relevance of one of Gray's genesis parameters (see above). In a conceptual model, they found a ventilation threshold, i.e. a bifurcation. Further evidence for the existence of such a threshold is given in a follow-up study (Tang and Emanuel, 2012b), where it is shown that the bifurcation is also visible in a non-hydrostatic axisymmetric convective model[4]. Emanuel (1989) demonstrated with a simplified axisymmetric model that mixing of low-entropy air into the boundary layer by shallow clouds or precipitation induced downdrafts can provide reasons for the finite amplitude nature of tropical cyclogenesis. Frisius and Hasselbeck (2009) showed with more complex models the importance of precipitating downdrafts in suppressing initial perturbations. Therefore, it is likely that such processes are an essential ingredient for realistic dynamical system characteristics of TCs.

---

[3]According to the fourth assessment report of the IPCC (Intergovernmental Panel on Climate Change), an increase in TC intensity appears to be more likely than not (Hegerl et al., 2007), i.e. the likelihood of TCs to become more intense in response to enhanced greenhouse gas forcing is estimated to be between 50% and 66%.

[4]In the context of numerical studies on TCs, models with a resolution sufficiently high to resolve convective motion are often referred to as "cloud-resolving", "convection-resolving", or simply "convective models" or "cloud models".

So as to contribute to a better understanding of tropical cyclone system dynamics with
regard to their potential intensity, two numeric axisymmetric models of different complexity
were employed in this study. We concentrate on the investigation of the sensitivity of the
maximum potential intensity of TCs to certain thermodynamic environmental parameters
comprising the SST, the tropospheric temperature stratification, and the tropospheric mois-
ture content in terms of environmental relative humidity. It must be stressed that there
are a number of physical processes related to asymmetric structures occurring in tropical
cyclones that have important implications for their formation and achievable strength, which
either cannot be resolved or are only poorly represented in axisymmetric models. However,
in the light of the near axisymmetry of most mature tropical cyclones, we share the view
that the axisymmetric approximation provides a useful basis for analytical and numerical
investigations on the maximum potential intensity of TCs as a function of their environment
(Rotunno and Bryan, 2012). Furthermore, it has been shown that the enforcement of an
asymmetric structure, due to vertical shear of the large-scale environmental flow as well as
a high translational speed of the storm, acts to lower TC intensity (Zeng et al., 2007, 2008).
This supports the view that axisymmetric models are suitable for the study on a theoretical
upper limit to TC intensity. Apart from this, a rather obvious advantage of the axisymmet-
ric idealisation in numerical studies is that the neglect of azimuthal variations allows one to
reduce the three-dimensional to a two-dimensional problem in cylindrical coordinates. This
lowers the computational costs by one or more orders of magnitude as compared to those
required to run a convection-resolving 3-D model.

In a first step, dynamical system properties are analysed within an idealised axisymmetric
modelling framework. In the conceptual model, the processes relevant to the dynamics of
TCs, some already mentioned above, are parameterised on the grounds of many simplifying
assumptions. In order to be able to further specify and capture physical processes on smaller
scales, such as convective motion, a model with a higher resolution is required. For this rea-
son, investigation of sensitivity of the potential intensity and phase space equilibria in terms
of the respective climatological parameters will be also performed with the high-resolution ax-
isymmetric cloud model HURMOD (Frisius and Wacker, 2007; Frisius and Hasselbeck, 2009).
The output of the conceptual model is not expected to be in excellent quantitative agreement
with the output of a model of relatively high complexity, with more processes resolved, or at
least incorporated via a comparatively sophisticated parameterisation. In fact, the principal
motivation behind the choice of our modelling approach[5] is the question, whether it is pos-
sible to distill a few processes that prevalently determine the dynamical system character of

---

[5]By modelling approach we mean the development and dynamical system analysis of the low-order TC
model and the subsequent intercomparison to the dynamical system properties of the high-resolution model
HURMOD.

a TC with regard to the climatological parameters in focus of this study. For this purpose, we test to what extent the conceptual model is able to reproduce the dynamical system behaviour of a convection-resolving model of intermediate complexity. The combined approach via conceptual, and axisymmetric convection-resolving models has proven to be valuable in for research on the upper bound of TC intensity as well as the controlling mechanisms for TC intensification in the recent past to the present [see e.g. Emanuel (1986); Rotunno and Emanuel (1987); Bryan and Rotunno (2009c,a); Frisius and Schönemann (2012)].

This study is organised as follows: An overview over different theoretical concepts and approaches to the maximum intensity of mature tropical cyclones from past to present is provided in chapter 2. The dynamical system analysis of a conceptual tropical cyclone model is discussed in chapter 3. Note that most of the contents presented in chapter 3 are identical to those that were published in the corresponding study by Schönemann and Frisius (2012). The conceptual model and the processes included are introduced in section 3.2. An estimate on the mature TC state is provided in section 3.3. The low-order model's equilibria, their stability and bifurcations with regard to different parameters are shown and discussed in section 3.4. In section 3.5, cyclogenesis mechanisms in the conceptual model and its transient dynamics are investigated, and finally major results from the low-order model and their implications are summarised and discussed in section 3.6. Parameter sensitivity and the dynamical system behaviour of the convective model HURMOD is investigated in chapter 4. Note also that the contents of chapter 4 have been submitted as a separate study to Tellus A (Schönemann and Frisius, 2014). Section 4.2 contains a brief introduction to the model and the experiments, which were designed and applied within the framework of this research project. The sensitivity of the vortex to several climatological parameters in HURMOD is investigated in section 4.3. The dynamical system behaviour of the tropical cyclone in HURMOD is depicted in section 4.4. A discussion of the results from HURMOD in comparison to those of the conceptual model is given in section 4.5. An overall summary and concluding remarks, and an outlook to remaining tasks and perspectives in the context of this study is given in chapter 5.

2   Different concepts of potential intensity in mature tropical cyclones

2.1   Introduction

The theory of potential intensity (PI), also referred to as maximum possible intensity (MPI)[6] is dedicated to the investigation of possible mechanisms that set an upper bound to tropical cyclone intensity. Since the middle of the 20th century, as observational data on tropical cyclones became more abundant, a number of different concepts and models have been proposed to assess a theoretically upper limit to TC intensity, which have provided the basis for much of the discussion that continues to today. Numerical models may provide another tool to bridge the gaps in data coverage, and to test certain hypotheses and either to substantiate or to invalidate the assumptions underlying them. Of course, any numerical model is ultimately only a more or less crude approximation to nature or reality, and can therefore never provide any definite, irrevocable proof.[7] Notwithstanding, numerical models can be applied to evaluate theoretical models, which cannot be solved analytically waiving fundamental simplifying assumptions and approximations, or for which an analytical solution has not been found, yet. The steady non-linear increase in computational power opened the possibility to conduct simulations with a grid-spacing sufficiently fine to resolve convective motion (Yamasaki, 1975). In turn, convection-resolving numerical models became increasingly applied in tropical cyclone research, and to investigate maximum possible intensity of TCs since the late 1970s (Yamasaki, 1977; Rosenthal, 1978; Rotunno and Emanuel, 1987). This chapter is dedicated to provide an overview over several theoretical concepts and practical approaches to the maximum possible intensity that were put forward by different authors since the 1950s until today. As pointed out in the introduction chapter, we will concentrate on concepts within an idealised axisymmetric framework.

---

[6]Note, both acronyms MPI and PI are used synonymously in scientific publications on tropical cyclone intensity of the past decades. In some earlier works, the term "maximum intensity" seemed to be more common [e.g. (Miller, 1958; Emanuel, 1988)], while later on the terms "maximum potential intensity" or "maximum possible intensity" came more frequently into use [e.g. (Emanuel, 1986; Holland, 1997; Camp and Montgomery, 2001; Bryan and Rotunno, 2009b)]. Many of the more recent works omit the word "maximum" as it is actually redundant in combination with the word "potential" and simply use the term "potential intensity" [e.g. (Bister and Emanuel, 2002; Smith et al., 2008; Bryan and Rotunno, 2009c,a)].

[7]In the study at hand, the term realistic related to the practise of modelling is used in a comparative way in two senses: Models that 1) either rely on fewer approximations in the sense that more physical processes can be resolved, or are accounted for via a refined parameterisation, or 2) models that yield results in closer agreement with those gained from observational data are referred to as more realistic. These two criteria do not necessarily coincide, as a parameterisation of a process is generally based on assumptions. If these assumptions are incorrect or rather inaccurate, there is still the possibility that they offset each other in their effect.

2.2 The concept by Kleinschmidt: Combination of dynamics and energetics

Kleinschmidt (1951) formulates his theory on mature TCs on the basis of essentially four simplifying assumptions: 1) axisymmetry, i.e. neglect of any azimuthal variations, which, inter alia, implies that the Coriolis parameter is considered to take a constant value, 2) neglect of the horizontal component of the Earth's angular velocity, 3) validity of hydrostatic balance, and 4) gradient wind balance above the frictional boundary layer. Gradient wind balance defines a stationary atmospheric flow, in which there is a balance between the Coriolis force, the centrifugal force and the pressure gradient force. A flow, characterised by this balance, is also referred to as gradient wind. The gradient wind equation in cylindrical coordinates can be written as:

$$\frac{v^2}{r} + fv = \frac{1}{\rho}\frac{\partial p}{\partial r}, \tag{2.1}$$

where v denotes the azimuthal velocity (also referred to as tangential or circumferential velocity), r the radial distance to the centre of a circular flow, f the Coriolis parameter, ρ the density, and p the pressure. In case of a cyclonic flow, the centrifugal acceleration (represented by the 1st term on the lhs) and the Coriolis acceleration (2nd term on the lhs) act outward, and are balanced by the pressure gradient acceleration (rhs of Eq. (2.1), which acts towards the pressure minimum in the centre of the tropical cyclone.

The absolute angular momentum m per unit mass of air with respect to the axis of the tropical cyclone is given by the sum of relative angular momentum with respect to the storm's rotation, and that related to the Earth's rotation:

$$m = vr + \frac{f}{2}r^2. \tag{2.2}$$

With this, the gradient wind equation (2.1) can be expressed as a function of m:

$$\frac{m^2}{r^3} - \frac{f^2}{4}r = \frac{1}{\rho}\frac{\partial p}{\partial r}. \tag{2.3}$$

As the flow above the boundary layer is presumed to be inviscid, m is a conserved property of individual parcels of air in the outflow. The observed pressure distribution infers that Eq. (2.3) is fulfilled when the outflowing air follows a slantwise course. Moreover, the air in the outflow of a mature TC, above the boundary layer is presumed to be in a dynamically moist-indifferent state[8]. This means that a parcel of air stays in equilibrium when it is displaced along its original streamline, and implicates that absolute angular momentum is

---

[8]As noted by Kleinschmidt, the assumption of zero internal friction within the outflow layer is idealised, and he presumes that a slight dynamical lability is required to overcome frictional effects in real storms.

conserved along moist isentropes, i.e. isopleths of equivalent potential temperature, θ_e, and entropy, s.[9] As the eyewall slants outward, this state may be also referred to as "slantwise neutral" (Emanuel, 1986) or as "isentropic inertial neutrality" (Holton, 2004). Because moist isentropes and angular momentum isopleths are required to be congruent under moist-neutral conditions, m can be formulated as a function of θ_e [cf. his Eq. (27)].

As also noted by Kleinschmidt (1951), slantwise neutrality requires that the outflow takes place under (moist-)statically stable conditions (i.e. θ_e increases with height). Otherwise, the dynamical indifference could not exist along a slantwise course. He argues dynamical moist-instability in a moist-statically stable environment to be the chief prerequisite for the formation of TCs. Moreover, he points out that the mature stage is highly dependent on the SST and the atmospheric structure in the environmental region, rather than on the initial disturbance. In his view, the latter is just required to contain a dynamical moist instability sufficiently strong to overcome initial resistance to the (outward) motion. Thus, he states that the mature TC is a stable entity, which develops through a transition from an unstable to a stable state: *„Wenn erst die eigentliche Energiequelle - die von der sturmgepeitschten See an die Luft abgegebene Wärme - erschlossen ist, dann strebt der Taifun einem nahezu stationären Zustand zu, der mit der ursprünglichen Labilität nichts gemein hat."*.

Previous observation-based works exhibited the existence of a dry zone surrounding the cyclone at midtropospheric levels. This led Kleinschmidt (1951) to the conclusion that the air from the outflow layer is sinking at a certain distance and then reentering the inflow boundary layer of a TC, indicating a closed circulation within a tropical cyclone. In turn, he argues that the energetics of a TC can be described in terms of a closed thermodynamic cycle as follows: Due to the thermodynamic disequilibrium at the surface, lots of water vapour is evaporated and taken up by the air in the low-level inflow layer from the ocean beneath; In the course of a moist-adiabatic ascent in the inner portion of the outflow layer, air reaches saturation, thereby releasing vast amounts of latent heat warming the upper core with respect to its surroundings; This results in a decreasing radial pressure gradient with height, which vanishes or even reverses at higher tropospheric levels; Furthermore, he postulates that the air, which finally leaves the outflow at higher levels in the far-field environment, becomes subject to radiative cooling, while it slowly sinks back down to the surface, thereby closing the cycle. A scheme indicating the corresponding branches of a Carnot cycle within a tropical cyclone is illustrated in Fig. 2.1. Kleinschmidt (1951) considers the processes that take place in the surrounding far-field environment, and in the eye of the TC to be of minor importance to the energy balance, and emphasises that latent heat gained from air-sea interaction is the

---

[9]Entropy and equivalent potential temperature are directly related as $s = c_p ln\theta_e + const$. Therefore, θ_e is representative for s, and vice versa. A very detailed elaboration of these terms can be found in Emanuel (1994), Chap.4, and a more concise description is provided in Bryan (2008).
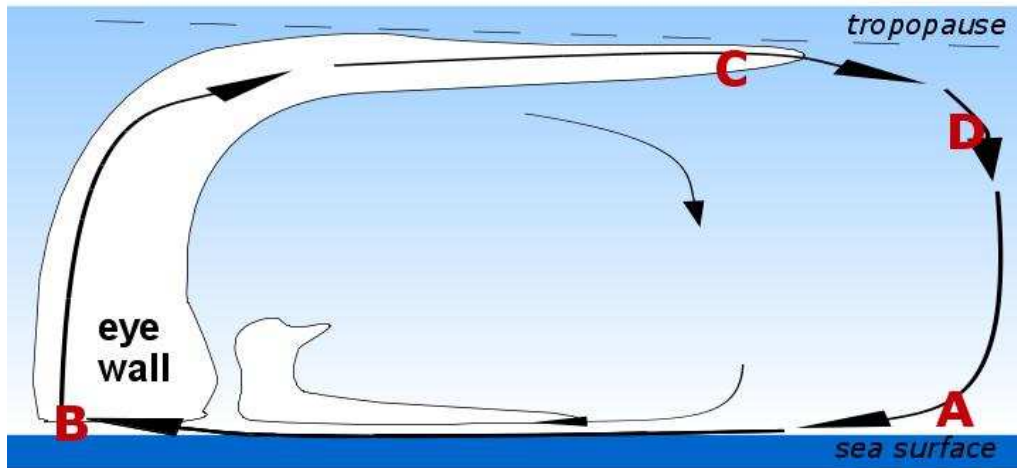
Figure 2.1: Idealised conception of a mature tropical cyclone as a Carnot engine: 1) isothermal expansion in the inflow (A to B); 2) adiabatic expansion in the eyewall updraft and ouflow (B to C); 3) isothermal compression via radiative cooling (C to D); 4) adiabatic compression in the course of far-field subsidence (D to A).

major source of energy for the mature storm. He formulates an equation for the maximum wind speed in the eyewall as a function of the net energy gain related to the thermodynamic cycle associated with the secondary circulation of the TC as described above.

2.3 An empirical thermodynamic approach to minimum central pressure by Miller

Miller (1958) investigated the potential intensity of TCs with regard to the minimum pressure that may be achieved within them. Miller's approach is rather phenomenological, not underpinned by an elaboration of an analytical theory [in difference to that of Kleinschmidt (1951)]. He proposes that the minimum possible pressure in the core of a hurricane depends on the sea surface temperature; relative humidity near the surface; the lapse rate within the storm; and the height and equivalent potential temperature at the top level of the vortex from which air can drop into the eye. Based on earlier theoretical and observational studies [cf. Miller (1958) and references], he carves out basic mechanisms and assumptions that need to be made to estimate the minimum possible pressure in the core of a TC. In this context, he stresses the role of motion and resulting temperature and relative humidity distribution within the inner portions of the TC. In accordance with earlier works [e.g. (Riehl, 1950)], he considers the air to rise moist-adiabatically as it approaches the core of the tropical cyclone[10].

---

[10]Note, Miller (1958) does not use the term "eyewall" in this context, but rather circumscribes an inner portion of a tropical cyclone, which is surrounding the eye and characterised by moist-adiabatic ascent associated with release of latent heat in air at (or close to) saturation. In principle, this corresponds to what is commonly referred to as the eyewall of a TC.

This results in a warming of the upper tropospheric layers in the core, and hence induces a lateral (warm core) temperature anomaly at higher levels.

Supposing the existence of an efficient high-level outflow mechanism, and assuming hydrostatic equilibrium, the warming of the core leads to a decrease in the central surface pressure. Miller points out, however, that the warming from parcel ascent and associated hydrostatic adjustment is insufficient to achieve pressures as low as they are observed within mature cyclones. He argues that warming by subsidence within the eye is the only mechanism able to provide the additional warming which is necessary to explain the low pressures in the eye; a view which is shared in other studies [e.g. Malkus (1958)]. As a first approach to account for the high temperature anomaly observed down to mid-levels, the air is presumed to subside into the eye from the top-level, at which the radial pressure gradient disappears (or changes sign). The occurrence of dry-adiabatic descent in the eye has also been postulated in an earlier study by Riehl (1948). Moreover, Miller indicates that observational data of the inner core structure delivers some more constraints or conditions that have to be considered to obtain a fairly realistic estimate of the minimum eye pressure: The eye is a calm region with low wind speeds on one hand, and relative humidity values well in excess of that which would result, if the air originated entirely from dry adiabatic descent from the top-level. This leads him to the conclusion that some lateral mixing of the surrounding moist air into the eye must take place.

To test the validity of his hypotheses on eye formation, Miller (1958) synthesises an eye sounding which is compared to observational data. He proposes an empirically derived relationship for the height-dependent fraction of moist air from lateral mixing of the eye with its surroundings, represented by a certain vertical distribution of relative humidity in the eye [cf. his Eq. (3)], which is attuned to available observational data and delivers rather realistic values for the minimum surface pressure. Miller points out that the proposed relationship is more representative for strong rather than for moderate tropical cyclones, which exhibit different mean relative humidities; as expected from the previous reasoning, the core of very intense TCs are much drier and warmer than those of moderate or weak tropical storms. Moreover, Miller approximates the surface pressure; relative humidity of surface air; and surface air temperature (assumed to be equal to the SST) to take a constant value before the onset of moist-adiabatic ascent. He carefully adverts the reader to the fact that this latter approximation implicates that the transfer of sensible heat arising by turbulent mixing related to the low-level inflow is disregarded in his model. With this, and the empirically derived relative humidity sounding of the eye, the temperature distribution in the eye and resulting minimum surface pressure (under hydrostatic adjustment) are determined iteratively. His model results indicate that TC intensity rises with sea surface temperature (cf. his Fig. 3).

2.4 The role of eye recirculation and thermodynamic far-field conditions in a conceptual model by Carrier et al.

In contrast to Kleinschmidt (1951) and Emanuel (see below), and similar to Miller (1958), Carrier et al. (1971) emphasise the role of the frictionally-driven recirculation in the eye to maintain an intense storm. To describe and capture the main features of a mature hurricane, they subdivide the hurricane into four regions: 1) The boundary-inflow layer; 2) the free troposphere above the inflow-layer (or ambient region), which is inward and upward bordered by 3) the eyewall region, characterised by upward and outward motion; and 4) the calm eye in the centre (cf. their Fig. 1). Carrier et al. (1971) presume that the gradient wind balance is valid in the ambient region and that the radial extent of the eyewall in the lower troposphere is negligible in comparison to the radial distance between the outer eyewall boundary and the radius of vanishing azimuthal velocity, r_0. The latter marks the outer boundary of their model. Furthermore, they make use of an empirical relationship for the decline of the tangential wind speed with increasing radial distance to the eyewall within a limited area, i.e. $v = cr^{-\beta}$ (Hughes, 1952), with $c, \beta = const.$, and for the decline exponent $0.5 \leq \beta \leq 1.0$. Assuming the density to be constant in the ambient region just above the boundary layer, and that the Rossby-number (in this context representing the relation between centrifugal and Coriolis force) is high, i.e. $fv << v^2/r$, and hence that the flow is in cyclostrophic balance, they obtain the following estimate for maximum tangential wind velocity [cf. their Eq. (4.1)]:

$$v_{max} = \left(\frac{2\beta}{\rho_0} [p(r_0) - p(r_2)] \right)^{\frac{1}{2}}, \tag{2.4}$$

where p denotes the pressure and r_2 the outer edge of the eyewall. The only variable here is the radial pressure difference between the eyewall and the far-field environment.

For a given environmental low-level pressure, $p(r_0)$, the pressure at the inner edge of the centre can be obtained for an ideal gas, making use of several assumptions. Like in previous studies, Carrier et al. (1971) assume hydrostatic conditions, and suppose that the air originating in the ambient region undergoes a moist-adiabatic expansion during the updraft in eyewall. A further prerequisite is that there is some interaction between the eye and the eyewall, which induces a recirculation in the eye. They hypothesise that this recirculation is largely responsible for maintaining the state of the dry air in the core. Most intense storms would occur, if the air after moist-adiabatic rise and associated expansion in the eyewall, were recompressed dry-adiabatically during its subsidence in the eye. In this view, the unknowns in the proposed calculation of the maximum tangential wind speed are reduced to the environmental (far-field) thermodynamic conditions, and the decline exponent β. Hence, the central pressure could be calculated from a given (low-level) pressure and temperature in

the far-field, by first calculating the temperature value from a moist-adiabatic ascent at the pressure-level on top of the eyewall, and then the temperature and pressure resulting from a dry-adiabatic descent to the surface in the calm, dry eye of the TC. They further note that the assumption of entirely dry-adiabatic descent in the eye results in unrealistically high estimates for v_{max}, and point out that a completely dry-adiabatic filling of the eye cannot be achieved, since there is some exchange with surrounding air and water masses. This is in principle the same conclusion as that drawn by Miller (1958) (see above). Consequently, the value of the pressure drop in the centre must be somewhere in between that gained from moist adiabatic eyewall ascent plus dry adiabatic descent in the eye, and that resulting (as if no eye were existent) from moist adiabatic ascent via hydrostatic adjustment throughout the core.

Beyond that, Carrier et al. (1971) note that the thermodynamic far-field conditions represented by the ambient vertical energy profile in the undisturbed area, on which their estimate of maximum intensity depends, are not static. They argue that the ambient processes to maintain the energy profile in the far-field environment, need to be explicitly included in a model of tropical cyclone energetics. In their energetical analysis, they make an attempt to evaluate the relevance of 1) the ambient air-sea energy conversion cycle, consisting of evaporation at the sea surface (in response to radiative heating of the surface ocean layer); upward transport of the water vapour by turbulent mixing or cumulus convection; atmospheric warming by release of latent heat of condensation; and cooling of the atmosphere by radiation to space, and 2) the boundary-layer flow associated with the TC. Since latent heat release is recognised as the major source of energy of the tropical cyclone, they evaluate the contribution of the boundary-layer inflow of the cyclone and associated turbulent fluxes (which they refer to as "forced convection") to the energy supply by analysing air-sea fluxes of energy. They find that the sea-surface energy flux associated with the motion in the inflow layer of a TC would reach only $\approx 10\%$ of the value that is observed in the undisturbed environment, given that the variation of turbulent diffusivity does not vary by much more than a factor of three. This leads them to the following conclusion: *"There is, therefore, no significant 'oceanic heating' in the sense of substantial additional sensible heat and water vapour transfer due to the wind fields; instead the boundary-layer energetics of the hurricane are dominated by the ambient vertical energy balance (the upward transfer of sensible and latent heat by turbulent mixing and cumulus convection and the radiative cooling) of the tropical atmosphere."*.

2.5 The air-sea interaction theory by Emanuel

In contrast to the concept introduced by Carrier et al. (1971), and in accordance with the principal ideas put forward by Kleinschmidt (1951), Emanuel (1986) presents an idealised

analytical model of a mature TC to show that TC intensification and maintenance entirely depends on an air-sea interaction instability, which relies on a positive feedback mechanism between surface wind speed and energy transfer via evaporation from the ocean to the atmosphere due to a thermodynamic disequilibrium between air and sea. This concept or feedback mechanism is usually referred to as "wind induced surface heat exchange" (WISHE) or air-sea interaction theory (Holton, 2004). Similar to Kleinschmidt (1951), Emanuel (1986) approximates the TC to be axisymmetric, and assumes that above the boundary layer the flow is in hydrostatic and gradient wind balance, and neutral to slantwise convection. For the derivation of the formulas for minimum central pressure and maximum wind speed, he follows the assumptions for the eye and eyewall boundary layer that 1) radial entropy advection is balanced by surface entropy fluxes, and 2) radial advection balances frictional loss of angular momentum. Moreover, Emanuel (1986) neglects effects of latent heat of fusion (i.e. the ice phase) and presumes pseudoadiabatic ascent along angular momentum isopleths (i.e. condensate is instantaneously removed). Following his theoretical approach, he demonstrates that a steady state tropical cyclone can be interpreted in terms of a Carnot heat engine, such as proposed earlier in the study by Kleinschmidt (1951) (cf. section 2.2).

On the basis of his 1986 paper, Emanuel derived a relation for the potential intensity expressed in terms of the squared maximum wind speed proportional to the thermodynamic efficiency,

$$\epsilon = \frac{T_{in} - T_{out}}{T_{in}}, \tag{2.5}$$

where T_{in} denotes the inflow temperature, and T_{out} the ouflow temperature; the thermodynamic disequilibrium between the ocean and atmosphere at the surface; and the ratio between the surface exchange coefficients for entropy (covering heat and moisture fluxes) and momentum. A frequently cited expression of this PI-formula can be found in Emanuel (1997) [cf. Eqs. (3) and (8) therein]:

$$v_{max}{}^2 = \frac{C_H}{C_D} \left(T_s - T_{out} \right) \left(s_{so}^* - s_b \right)|_{r_{max}} \cong \frac{C_H}{C_D} \frac{T_s - T_{out}}{T_s} \left(k_{so}^* - k_b \right)|_{r_{max}}, \tag{2.6}$$

where v_{max} is the maximum wind speed, the variables s and k denote specific entropy and enthalpy, respectively, which are evaluated in the eyewall region near the radius of maximum wind speed, r_{max}. T denotes absolute temperature, and C_H and C_D are the surface exchange coefficients for heat and momentum, respectively. We note, if the pressure and temperature in the boundary layer are assumed to be equal to that at the sea surface, the enthalpy difference is equal to the entropy difference divided by the surface temperature, T_s, i.e. $k_{so}^* - k_b = (s_{so}^* - s_b)/T_s$, which follows from the first law of thermodynamics. The surface exchange coefficient for heat is presumed to be equal to that for moisture, hence C_H represents

both air-sea temperature and moisture fluxes[11]. The indexes s, so, and b indicate evaluation at the surface, at the ocean surface, and in the boundary layer, respectively. T_{out} is the entropy-weighted mean outflow temperature [cf. Eq. (19) in Emanuel (1986)], and the inflow temperature of the low-level air is approximated by T_s. The potential intensity formula given by Eq. (2.6) is based on the further simplifying assumption that gradient wind can be approximated by cyclostrophic wind at the location of maximum surface wind speed.

The relevance of the ratio between the surface exchange coefficients, C_H/C_D, is investigated in Emanuel (1995a). In the analytical approach presented in Emanuel (1986), PI in terms of minimum central pressure is formulated on the grounds of the approximation that the eye and eyewall are dynamically similar. In difference to his original analytical TC model from 1986, Emanuel (1995a) relinquishes this approximation and considers the eye and eyewall to behave dynamically different in the sense that a balance between radial entropy (and momentum) advection in the boundary layer and surface entropy (and momentum) fluxes, as well as slantwise convective neutrality are presumed to be fulfilled in the eyewall, but not in the eye. Instead, the minimum central pressure (in the eye), is calculated based on the hypothesis that the eye develops passively with the eyewall via a viscous adjustment, which acts to preserve the maximum wind speed and relaxes the velocity profile towards a linear dependence on the radius, in principle like in a solid body rotation. This implies the central pressure to be a function of maximum wind speed, and hence to depend as well on the ratio of the surface exchange coefficients. Combination of Eq. (16) of Emanuel (1995b), which basically introduces a new variable as a product of entropy differences and the difference between sea surface and tropopause temperature, and Eq. (13) in Emanuel (1995a), which is almost equivalent to the expression for v_{max} of Eq. (8) in Emanuel (1997), also delivers the PI-formula given above [Eq. (2.6)]. However, the outflow temperature in Emanuel's 1995 papers is approximated by the tropopause temperature T_t [cf. Eq. (16) in Emanuel (1995b)].

2.5.1   The effect of dissipative heating

Emanuel's earlier PI-formula [Eq. (2.6)] was further extended by Bister and Emanuel (1998), who take into account the effect of dissipative heating in the boundary layer of the storm, i.e. they assume entropy advection under the eyewall of a mature TC to be balanced not only by surface entropy fluxes but also by frictional heating within the boundary layer. The dissipation in the atmospheric boundary layer is presumed to heat up the air and not the ocean beneath. Introduction of dissipative heating such as described above to the precursory

---

[11]In the following, we may refer to C_H as the surface exchange coefficient for entropy, enthalpy or simply "heat", as all of these three designations are frequently used for C_H equivalently under the assumption made here that the surface exchange coefficient for sensible heat equals that for latent heat.

theoretical PI model of Emanuel leads to a revised PI formula [cf. Eq. (21) in Bister and Emanuel (1998)], which is similar to that given by Eq. (2.6):

$$v_{max}^2 = \frac{C_H}{C_D} \frac{T_s}{T_{out}} (T_s - T_{out}) (s_{so}^* - s_b)|_{r_{max}} \cong \frac{C_H}{C_D} \frac{T_s - T_{out}}{T_{out}} (k_{so}^* - k_b)|_{r_{max}} . \qquad (2.7)$$

The only difference to Eq. (2.6) arises by the additional factor T_s/T_{out} included in Eq. (2.7). Because $T_s > T_{out}$, T_s/T_{out} is greater than unity. Consequently, as pointed out by Bister and Emanuel (1998), the effect of incorporating dissipative heating is identical to that of increasing the ratio of the surface exchange coefficients, C_H/C_D, by the factor T_s/T_{out}, which in turn is equivalent to an increase of the surface exchange coefficient for heat, C_H. Their results from simulations with the numerical model of Rotunno and Emanuel (1987) exhibit that dissipative heating increases the maximum wind speed by about 20%. Moreover, Bister and Emanuel (1998) present a derivation of Eq. (2.7) from conservation principles and thereby get down to a non-arbitrary definition for the outflow temperature, T_{out}: *"It is the temperature along the angular momentum surface that passes through the locus of maximum winds, at the point at which the tangential velocity, v, vanishes."*.

2.5.2   Self-stratification in the outflow

Emanuel and Rotunno (2011) find that the TC outflow simulated by a convection-resolving axisymmetric model develops its own temperature stratification, unrelated to that of the unperturbed environment. They suggest that the temperature stratification of the outflow layer is set by the requirement that the Richardson number, Ri, which is therein defined by the ratio between buoyancy forces, and vertical shear of the horizontal flow [cf. their Eq. (23)], does not fall below its critical value (close to unity) for the onset of small-scale turbulence. In a first step, the original PI-Formula of Emanuel is rederived on the basis of the thermal wind-equation [cf. their Eq. (11)]; the definition of the outflow temperature according to that given in Bister and Emanuel (1998) (see above), without specifying a fixed value for T_{out}; and the entropy budget equation in steady state [cf. their Eq. (16)]. Three further simplifying assumptions are made: 1) dissipative heating is neglected; 2) in the boundary layer, the radii of angular momentum isopleths are treated as vertically invariant (i.e. m-isopleths are approximately vertical); 3) and entropy is considered to be well-mixed along angular momentum surfaces in the boundary layer. Employing the classical aerodynamic flux formulas [cf. their Eqs. (19) and (20)], and making use of the gradient wind approximation, they arrive at the original PI-formula [Eq. (2.6)]. They concede that gradient wind balance results in an underestimate of actual intensity, as shown in other studies (which is to be outlined below in section 2.7), but they point out that the balance assumption is still appropriate for the

purpose of their study; i.e. to investigate the deficiencies of Emanuel's classical PI theory that are related to previously made assumptions with regard to the outflow temperature.

Emanuel and Rotunno (2011) emphasise that the classic PI formula only yields a closed solution, when T_{out} is known, and put forward that T_{out} is regulated by their proposed self-stratification mechanism in the outflow layer, i.e. by internal storm dynamics rather than an adjustment to the environmental stratification via inward transport of information. This hypothesis is underpinned by the output gained from a simulation with a numerical high-resolution model, in which the free troposphere is relaxed to approach a constant value in saturation entropy in the far-field environment. Their numerical results reveal that only the air along the outflow streamline, which passes through the radius of maximum winds gets close the ambient tropopause temperature, whereas most of the outflow, which originates outside the radius of maximum winds, exhibits higher temperatures at the locus where the azimuthal wind reverses sign. Moreover, the absolute temperature in the outflow layer appears to increase with (outward) decreasing saturation entropy, resulting in an enhanced difference between the vertically averaged outflow temperature and that at the ambient tropopause. They argue that this behaviour is at odds with the assumption of a constant outflow temperature.

They draw the conclusion that on physical grounds, the tropopause temperature, used in previous studies (see above), is actually a poor approximation to the actual outflow temperature. Calculations of the Richardson number over a region in the inner portions of the modelled TC at high levels, where the motion turns radially outward, indicate that Ri gets close to its critical value there (cf. their Fig. 7). With view to this result, they relate the dependence of the outflow temperature on saturation entropy to the critical Richardson number. This closure is applied within the classic PI formula [Eq. (2.6)], to replace the simple approximation of T_{out} by the tropopause temperature T_t, and thus to incorporate the proposed mechanism of self-stratification in the outflow layer. On this basis, Emanuel and Rotunno (2011) release a refined PI formula:

$$v_{max}{}^2 = \frac{C_H}{C_D}\left(T_b - T_t\right)\left(s_{so}^* - s_{env}^*\right)\left(\frac{1}{2}\frac{C_H}{C_D}\right)^{\frac{C_H/C_D}{2-C_H/C_D}},\tag{2.8}$$

where T_b is the absolute temperature of the air in the boundary layer (T_b can be assumed to be equal to or slightly less than the sea surface temperature, T_s). The PI formula given by Eq. (2.8) differs from the classic one [Eq. (2.6)] in the additional factor, which is only a function of C_H/C_D, and in that the entropy of the boundary layer beneath the eyewall is replaced by the saturation entropy of the free troposphere in the ambient region, s_{env}^*. [12]

---

[12] A detailed derivation of Eq. (2.8) can be found in the appendix of Frisius et al. (2013).

2.6   Consideration of a feedback between surface pressure drop and eyewall entropy increase by Holland

As in previous model approaches to TC intensity that were mentioned above, Holland (1997) approximates the structure of a mature TC to be axisymmetric and in hydrostatic balance. In difference to Kleinschmidt and Emanuel, Holland's PI model does not involve any detailed discussion on the energetics of the secondary circulation. Holland's approach is in many ways similar to the concept proposed by Miller (1958). However, an essential amendment across from Miller's concept, consists in the explicit inclusion of an eyewall and the feedback between the surface pressure reduction under the eyewall and surface equivalent potential temperature: As Holland points out, a reduction in the surface pressure beneath the eyewall, with specified values for relative humidity and temperature, must come along with an increase in equivalent potential temperature at the surface; further moist-adiabatic ascent of air with enhanced entropy leads to further upper-level eyewall warming, and hence to a further decrease of the surface pressure via hydrostatic adjustment. The additional entropy for this isothermal expansion must be derived from the ocean. This feedback was not included in the estimate on minimum surface pressure by Miller (1958), and found to be only rather small by Carrier et al. (1971) (see above).

Moreover, Holland (1997) demonstrates that the surface pressure decrease related to this ocean-atmosphere feedback, converges. Consequently, the surface pressure fall in response to moist-adiabatic ascent and the associated entropy increase via oceanic fluxes is also limited, but higher than that, one obtains, if the (local) oceanic feedback under the eyewall is not considered. In addition, similar to Miller (1958), Holland explicitly includes an eye, which is presumed to be filled with both subsided air from the top-level and moist air from lateral mixing with the eyewall, with the latter becoming more prevalent towards lower levels. Furthermore, he postulates that the maximum entropy available to the eye equals that originating at the surface beneath the inner eyewall. Using this constraint, specifying an environmental temperature sounding, and making an estimate on the vertical relative humidity distribution within the eye, he derives the temperature structure in the eye to obtain the central surface pressure; thereby including the effect of subsidence warming. Holland finds that moist-adiabatic eyewall ascent and the related air-sea feedback contributes about twice as much to the total pressure fall than subsidence warming in the eye. Against this background, and in difference to Miller (1958) and Carrier et al. (1971), Holland (1997) concludes that the increase in entropy that can be achieved by atmosphere-ocean interaction beneath the eyewall is most important for the potential intensity of TCs. In this regard, there is some agreement between Holland and Emanuel. However, as Holland (1997) does not make any assumptions on the dynamics of TCs (in the sense of the forces that drive the motion within

them), his concept relies on the application of empirical relationships to estimate maximum wind speeds from minimum central pressure, which he admits to be probably oversimplified.

2.7   Different approaches to superintensity

Emanuel's theory on potential intensity experiences high acceptance, and his PI formula is widely used as a reference in the field of tropical cyclone research [usually in the formulation, which accounts for dissipation as given by Bister and Emanuel (1998), see Eq. (2.7)]. However, as was shown by Persing and Montgomery (2003) and others (Bryan and Rotunno, 2009c,a; Frisius and Schönemann, 2012), simulations with axisymmetric convection-resolving models may deliver wind speeds that are well in excess of that predicted by Emanuel's PI theory. Moreover, as shown by Wang and Xu (2010), superintensity does also arise in 3-D models, which further substantiates the conjecture that maximum intensity may reach higher values than those predicted on the grounds of Emanuel's theory. Persing and Montgomery (2003) introduced the term "superintensity" to refer to the exceedance of Emanuel's potential intensity in terms of maximum wind speed in convection-resolving models.

2.7.1   The possible role of low-level eye entropy versus horizontal mixing

Persing and Montgomery (2003) argue that the assumption of moist-neutral ascent in the eyewall, and the neglect of eye-eyewall interaction are chiefly responsible for an underestimate of PI by Emanuel's theory. They find that superintensity increases with increased model resolution, until the resolution is sufficiently high to capture the relevant inner core interaction processes. A feature of the eye circulation, which is crucial to their explanation for the observed sensitivity of superintensity to model resolution, is the concentration of eye subsidence in a narrow column next to the inner eyewall, accompanied by a weaker descent in the inner parts of the eye compared to that obtained at lower resolution. This serves as a possible explanation for the entropy distribution, they obtain within the eye in high resolution simulations ($\Delta r \leq 3.75$ km), i.e. a locally enhanced entropy in close proximity to the eyewall on one hand, and a mid-level entropy minimum in the central part of the eye on the other hand.

Similar to Miller (1958) (see above), Persing and Montgomery (2003) consider the local entropy increase in the downdraft next to the eyewall to be a result of a combination of dry subsidence and turbulent (subgrid-scale) inward mixing from the saturated eyewall into the eye, with the latter acting to lower the entropy. Moreover, they depict that the negative entropy anomaly in the innermost part of the eye can be ascribed to the very low moisture content of the slowly subsiding air, which locally enhances the air-sea thermodynamic disequilibrium with regard to moisture, and leads to increased latent heat fluxes from the ocean

into the subsaturated eye. They note that the warming of the eye also leads to a reversed sensible heat flux (i.e. from the atmosphere to the ocean), however, this is outbalanced by far through the strong latent heat fluxes, resulting in a surplus of entropy in the low-level eye. To maintain a steady state under these conditions, there must be an outward directed entropy flux into the eyewall: Persing and Montgomery (2003) suggest that the additional latent heat in the low-level eye is taken up by the air that is subsided in the narrow downdraft at the outer edge of the eye, and than recirculated into the eyewall, thereby further enhancing the eyewall entropy and the storm's intensity. As a measure for the additional heat from the eye that is induced into the updraft as described above, they suggest to compare the equivalent potential temperature at the top of the eyewall updraft, $\theta_{e,out}$, to that at its base, $\theta_{e,surf}$, and to extend Emanuel's PI formula by replacing T_s with the sum of sea surface temperature and the respective difference in θ_e in the eyewall, i.e. $T_s' = T_s + (\theta_{e,out} - \theta_{e,surf})$ [cf. their Eq. (17)].

In the first contribution of their 2009 paper trilogy on PI, Bryan and Rotunno (2009b) confirm that the mechanism that leads to a low-level eye entropy increase as described by Persing and Montgomery (2003) does exist, but they show that it does not have a considerable effect on the maximum wind speed in an axisymmetric framework. They evaluate the influence of the enhanced low-level eye entropy on intensity in axisymmetric convection-resolving models by switching off its source, i.e. simulations are conducted in which surface entropy fluxes beneath the eye (and in the innermost part of the eyewall next to the eye) are set to zero. Regardless of whether the positive low-level entropy anomaly in the eye forms or not, they obtain considerably superintense TCs, i.e. maximum tangential wind speeds well in excess of those predicted by Emanuel's PI theory. Their quantitative model analysis yields that surface entropy fluxes in the eye would have to be one order of magnitude larger to have a notable effect on TC intensity. However, Bryan and Rotunno (2009b) note that such enhanced surface fluxes lead to positive low-level entropy anomalies in their simulations, which are at least twice as high as those reported in observations [see Bryan and Rotunno (2009b) and references]. They conclude that, in reality, surface entropy fluxes in the eye, and subsequent low-level entropy transport into the eyewall are too weak to account for the discrepancy between Emanuel's PI and that found in high-resolution axisymmetric cloud models.

In a follow-up study, Bryan and Rotunno (2009c) show that modelled axisymmetric intensity is rather sensitive to turbulent horizontal diffusion. As a non-axisymmetric subgrid-scale process, turbulent mixing must be parameterised and is assumed to be proportional to a certain mixing length scale, l_h (details on the parameterisation of subgrid-scale processes in an axisymmetric cloud model will be given in subsection 4.2.2). Bryan and Rotunno (2009c)

point out that the mixing length scale should be interpreted as a physical parameter. In contrast, Persing and Montgomery (2003) ascertain that l_h varies linearly with grid-spacing, and hence interpret the turbulent mixing length scale as a resolution-dependent parameter. Bryan and Rotunno (2009c) show that intensity increases with decreasing values in l_h, which correspond to a decrease in turbulent horizontal mixing, and reason that the superintensity found by Persing and Montgomery (2003) in simulations with enhanced resolution can be largely ascribed to their choice for l_h, instead of the originally proposed effect of enhanced low-level eye entropy.

Moreover, the high-resolution modelling approach to maximum intensity presented in Bryan and Rotunno (2009c) gives evidence that, beside inviscid flow in the radial direction, pseudoadiabatic conditions, which they closely put into practise by maximising the fall velocity for liquid water, are most favourable for the development of strong TCs, while a highly viscous radial flow, and reversible cloud-microphysics deliver comparatively weaker TCs. The latter can be explained by the impact of condensate loading on surface pressure in an air column: If all the condensate is assumed to immediately fall out (i.e. to be instantaneously removed from the column), the buoyancy is higher than in the case of reversible adiabatic ascent, in which no condensate is removed via precipitation. A higher buoyancy contributes to a lower surface pressure. As most of the air rises in the eyewall, i.e. in the central portion, this surface pressure effect is expected to be most pronounced beneath the eyewall with the respective effect on storm intensity. Of course, non of these two opposed idealisations meet the conditions in the real troposphere, but the truth is rather in between them.

2.7.2   Gradient wind imbalance

In a third contribution, which consists of a combined numerical modelling and analytical approach, Bryan and Rotunno (2009a) show that the dynamical balance assumptions (i.e. hydrostatic conditions and gradient wind balance), and in particular the assumption of gradient wind balance, results in an underestimate of the actual maximum wind speed. This issue has also been raised by Smith et al. (2008), who point out that superintensity occurs as the tangential wind in the boundary layer becomes supergradient[13] in the inner eyewall region of the tropical cyclone. Smith et al. (2008) argue that a more complete formulation of the boundary layer is required to gather this imbalance and the resulting enhancement in maximum wind speed. Bryan and Rotunno (2009a) confirm that the flow at the location of v_{max} is substantially supergradient in simulated TCs, but the analysis of their numerical

---

[13]The horizontal flow is termed as supergradient, if the outward directed forces per unit mass from centrifugal and Coriolis acceleration exceed the inward directed pressure gradient acceleration [cf. Eq. (2.1)], and is referred to as subgradient in the opposite case.

model results with regard to the boundary layer closure of Emanuel's PI leads them to the conclusion that this closure is sufficiently accurate. However, they note that they only evaluate the final boundary layer closure by Emanuel within their numerical model, rather than judging the different assumptions underlying it.

Instead of trying to estimate supergradient winds in the boundary layer by application of a refined boundary layer closure as suggested by Smith et al. (2008), Bryan and Rotunno (2009a) introduce an unbalanced term in addition to the free-atmosphere component of Emanuel's model. The additional unbalanced flow term represents a lower boundary condition of the free atmosphere to capture superintensity, but it does not deliver any information on the formation mechanism of the supergradient wind. On the basis of conservation principles, following the technique used by Bister and Emanuel (1998), they derive an analytical model, which incorporates the gradient wind imbalance of the eyewall flow, and gives way to the formulation of an extended PI equation [cf. their Eq. (23)]:

$$v_{max}{}^2 = \frac{C_H}{C_D}\frac{T_s}{T_{out}}\left(T_b - T_{out}\right)\left(s_{so}^* - s_{out}\right) + \frac{T_s}{T_{out}}r_{max}\eta_b w_b, \qquad (2.9)$$

where the subscript *out* denotes values that are averaged along the section of the upper-layer eyewall outflow, where the tangential velocity vanishes, following closely the definition for T_{out} given by Bister and Emanuel (1998) (see above); the index b denotes variables that are evaluated at the top of the boundary layer; w is the vertical velocity; and $\eta \equiv \partial u/\partial z - \partial w/\partial r$ is the azimuthal vorticity. The notation of the other variables is the same as in Eqs. (2.6), (2.7), and (2.8), and all variables are evaluated at, or along the streamlines that pass through v_{max}, respectively. Superintensity is represented by the second term on the rhs, which can be seen by comparison to Eq. (2.7). Bryan and Rotunno (2009a) show that their analytical model is in excellent quantitative agreement with the numerical model, and conclude that the refined PI formula [Eq. (2.9)] is very well able to account for the superintensity found in axisymmetric convection-resolving models (cf. their Fig. 12). Yet, they note that it relies on many variables that must be supplied by the numerical output itself, and cannot be derived from environmental conditions, which ideally provide the thermodynamic initial and boundary conditions for the numerical models.

In difference to Bryan and Rotunno (2009a), Frisius et al. (2013) pick up the idea put forward by Smith et al. (2008), and investigate the relation between superintensity and gradient wind imbalance on the grounds of a boundary layer model, in which imbalanced flow is taken into account directly. For this purpose, the classical PI theory by Emanuel is combined with a slab boundary layer model based on that developed by Smith (2003). Frisius et al. (2013) concede that slab boundary layer models, where all properties are assumed to

be vertically independent by definition, and the calculation of surface drag is based on vertically averaged horizontal velocity, were shown to overestimate the radial inflow (Kepert, 2010a,b). Consequently, the use of a slab boundary layer results in too strong supergradient winds. On the other hand, they point out that it is not the major purpose of their study to accurately quantify superintensity invoked by gradient wind imbalance as has been done by Bryan and Rotunno (2009a). Instead, Frisius et al. (2013) aim to contribute to a qualitative understanding of the relation between low-level supergradient winds and superintensity, and argue that the use of a slab boundary layer model is sufficient to this end.

They do not provide an extended PI formula, but investigate the sensitivity of supergradient winds, and the associated superintensity to the independent parameters of the applied slab boundary layer model, in order to delineate the supergradient wind regime. For determination of the unbalanced boundary layer wind, they assume that 1) gradient wind imbalance vanishes at a certain height above the boundary layer; 2) that super- and subgradient winds above that height exactly cancel each other in effect, so that gradient wind imbalance can be neglected there; and 3) that the pressure gradient force is vertically constant between the surface and the assumed height of vanishing gradient wind imbalance. With regard to their second assumption, Frisius et al. (2013) note that it is not clear, whether the effect of gradient wind imbalance actually gets close to zero on vertical average, but they choose to focus on the effect of gradient wind imbalance in the boundary layer against the background that it is most probably the region, where the imbalanced flow is generated.

Frisius et al. (2013) follow the reasoning that the immediate (outward) vorticity increase at the location of maximum tangential wind speed in combination with the inertia of the radial inflow is the major reason for the occurrence of supergradient winds; i.e. the radial wind cannot adjust immediately to the sudden increase in vorticity, resulting in an inward-directed overshoot beyond the radius of maximum gradient winds (RMGW). This is in accordance with their finding that both inflow strength and superintensity are rising with increasing values for the decay exponent β of the tangential wind profile[14] (cf. their Fig. 6), because the vorticity near the radius of maximum gradient wind speed decreases with increasing β values. Furthermore, the model behaviour in response to changes in the RMGW exhibits a horizontal scale-dependence of potential intensity and superintensity, which points to the existence of an upper and a lower bound for the radius of maximum winds in a steady state TC, and gives rise to the conjecture that the optimal RMGW is interrelated to the largest supergradient winds. In this context, Frisius et al. (2013) ascribe the degree of superintensity due to supergradient winds to two competing effects: 1) the inertia of radial inflow, which is

---

[14]The decay exponent β may also be referred to as modified Rankine decay exponent [e.g. Mallen et al. (2005)], and is used to describe the radial decrease of tangential wind speed as noted further above in section 2.4.

conducive to superintensity; and 2) the degree of subgradient wind imbalance in the boundary layer outside the radius of maximum gradient winds, which has a weakening effect on superintensity. As they point out, the latter effect becomes dominant for larger maximum gradient wind radii (cf. their Fig. 3). A combined view reveals that the RMGW value at which maximum superintensity arises increases with decreasing β, which is consistent with the idea that enhanced vorticity may act like a wall to inhibit the inflow.

Further results of the analytical model indicate that superintensity increases with increasing Rossby number, Ro. For fixed values in the RMGW and $v_{g,max}$, the Rossby number only depends on the inverse Coriolis parameter, and therefore, the sensitivity to Ro can be translated into a latitudinal dependence of the degree of superintensity due to gradient wind imbalance. Hence, superintensity is expected to be larger at lower than at higher latitudes. Moreover, they find that the RMGW, which delivers the highest supergradient winds, becomes larger with decreasing Rossby number (cf. their Fig. 7b). According to the supposition that tropical cyclones possess an optimal RMGW, which is related to maximal supergradient winds, they note that the latter result suggests that TCs should be smaller (in their spatial extent) near the equator, than at higher latitudes.

Frisius et al. (2013) show that results from further sensitivity tests, taking into account the effect of horizontal mixing in the slab-boundary layer model, are in good qualitative agreement with those obtained by neglecting horizontal diffusion. The diffusive case exhibits a systematically lower inflow strength and superintensity than the non-diffusive case, as expected with view to the work by Rotunno and Bryan (2012) (cf. their Figs. 7a and 1e). Although Frisius et al. (2013) note that the boundary layer model solution for a very high mixing length ($l_h = 3000$ m) delivers notably different features in the wind-profile than the other cases, and the numerical high-resolution simulations by Rotunno and Bryan (2012). They surmise that this discrepancy is chiefly assignable to the fact that the gradient wind is treated like in the non-diffusive case in their analytical model, and therefore leads to an unrealistic result in case of very strong horizontal diffusion. Except for this, the analytical results by Frisius et al. (2013) exhibit a similar response to variations in the horizontal mixing length, l_h, like that found by Rotunno and Bryan (2012).

Another extension of the slab-boundary layer model is adopted from Smith (2003) to investigate the possible effect of vertical momentum transfer from the free troposphere into the inflow layer of the ambient region. In agreement with Smith (2003), Frisius et al. (2013) find that the entrainment of cyclone-scale subsidence is negligible, whereas entrainment via shallow convection turns out to inhibit superintense flow. They explain that the weakening caused by shallow convection can be understood on the grounds of the effect of the associated

vertical angular momentum transport, which counteracts the tendency of the inflow to conserve angular momentum; This results in a lower inflow strength, and an enhanced vorticity, which forms a resistance towards the overshoot.

Aside from the sensitivity tests within the classical form of Emanuel's PI theory, Frisius et al. (2013) apply the slab-boundary layer model within the extended PI model by Emanuel and Rotunno (2011). This allows to reduce the number of independent model parameters, since the vortex structure in the outer region is determined by the assumption of a constant Richardson number (see subsection 2.5.2), and does therefore not depend on the decay parameter β. Nevertheless, it yields unrealistically high inflow strengths and superintensities. With view to this result, they concede that a more realistic outcome may be attained for a less simplified boundary layer model, as advocated by Kepert. Despite the considerable quantitative mismatch, the sensitivity to the Rossby number and the RMGW are qualitatively similar to those gained in the classical PI framework. Overall, Frisius et al. (2013) conclude that superintensity due to supergradient winds can be described as an extension of the classical PI model of Emanuel by application of a slab boundary layer model.

2.7.3   *Slantwise convective available potential energy*

Frisius and Schönemann (2012) proposed to extend Emanuel's PI by consideration of the existence of slantwise convective available potential energy (SCAPE) in the ambient region. In general, convective available potential energy (CAPE) is defined as the amount of energy available for the convection of a particular parcel of air [e.g. Emanuel (1994); Holton (2004); Kraus (2004)]. It is usually taken as a measure of the kinetic energy that a statically unstable parcel can acquire, and is therefore sometimes also referred to as "lability energy" (Kraus, 2004). Under hydrostatic conditions, CAPE for a parcel rising from some initial pressure level, p_{init}[15], to the level of neutral buoyancy (LNB) can be expressed by

$$CAPE = \int\limits_{p_{LNB}}^{p_{init}} (\alpha_{parc} - \alpha_{env})\, dp, \qquad (2.10)$$

where α_{parc} denotes the specific volume (i.e. volume per unit mass) of the parcel, and α_{env} that of the environment. As demonstrated by Emanuel (1994), CAPE may also be evaluated

---

[15]In a conditionally unstable atmosphere, a parcel is only potentially statically unstable, i.e. it has to be lifted via forced ascent until it becomes less dense than its surroundings, and hence positively buoyant, at the so-called level of free convection (LFC). Therefore, p_{init} is specified by the pressure at the LFC in the definition of CAPE (e.g `http://glossary.ametsoc.org/wiki/Convective_available_potential_energy`)

by a function of the difference in saturation entropy between a parcel and its environment [cf. Eq. (6.4.2) in Emanuel (1994)]:

$$CAPE \simeq \int_{T_{LNB}}^{T_{init}} \left(s_{parc}^* - s_{env}^* \right) dT. \tag{2.11}$$

The relation given by Eq. (2.11) is based on the assumption of a pseudoadiabatic ascent[16], and neglect of the effect of water substance on density. Slantwise CAPE (SCAPE) is determined analogously to CAPE by integration along angular momentum isopleths, hence accounting for the combined effect of static and inertial instability. Now, presuming that air reaches saturation if it rises adiabatically from the well-mixed boundary layer up into the free troposphere, allows us to evaluate SCAPE as a function of the difference between boundary layer entropy, s_b, and saturation entropy in the free troposphere, s^*. Moreover, if the saturation entropy in the free troposphere is assumed to be constant along angular momentum isopleths and saturation arises at the LFC, SCAPE arises when $s_b > s^*$, and vanishes exactly when $s_b = s^*$. The latter case (with zero SCAPE) establishes slantwise neutral conditions. The mere evaluation, whether SCAPE exists or not, is to follow this simplified view in Frisius and Schönemann (2012), and in the study at hand, but for an accurate quantification of SCAPE under hydrostatic conditions, Eq. (2.10) is applied along angular momentum isopleths.

In the analytical model presented by Frisius and Schönemann (2012), the radial profiles of boundary layer entropy are formulated in a similar manner as in Emanuel (1995a), taking into account sea surface fluxes of momentum and entropy, and presuming the eye to be in solid body rotation with zero SCAPE in the inner core. On the other hand, Frisius and Schönemann (2012) introduce a further refinement to Emanuel's concept through a distinction between the eye and the eyewall by application of different relations for entropy and velocity profiles, respectively. In their model, the frontal character of the eyewall, or the sharpness of that front, is allowed to be more pronounced than in Emanuel's model, which implies steeper radial gradients within the eyewall updraft. The entropy profile in the ambient region is formulated in a way to match that of the eyewall at the radius of maximum winds, and such that entropy decreases outward with increasing radial distance to the radius of maximum tangential wind. Moreover, the saturation entropy in the ambient region is assumed to become equal to the boundary layer beneath at a certain radius located outside the eyewall. Beyond this radius, the entrainment of air from the free troposphere into the boundary layer is assumed to lead to a neutral stratification (i.e. $s^* = s_b$) as presumed by Emanuel.

---

[16]Entropy defined through pseudoadiabatic ascent is equal to or smaller than the reversibly defined entropy, because only the latter accounts for the heat carried by condensed water (see Emanuel (1994), Chap. 4).

In turn, in the model of Frisius and Schönemann (2012), SCAPE may arise in the ambient region over an area limited by the assumed radius of neutral stratification. SCAPE is also coupled to the width of the eyewall updraft, because the narrower the updraft, the lower becomes the saturation entropy of the air near and outside the radius of maximum tangential wind relative to that in the boundary layer beneath. As the boundary layer entropy profile applied by Frisius and Schönemann (2012) is assumed to be like that in Emanuel (1995a), the dependence of superintensity on SCAPE can be expressed by [cf. their Eq. (29) and (1)]:

$$\frac{v_b^2 - v_{b,EPI}^2}{m} = \frac{\partial E_C}{\partial m},\tag{2.12}$$

where m is the specific angular momentum, $v_{b,EPI}$ denotes the tangential wind velocity at the top of the boundary layer according to Emanuel's PI theory, and $E_C \cong (T_s - T_t)(s_b - s^*)$. Given that $s_b \geq s^*$, E_C may be approximately identified with SCAPE, as noted by Frisius and Schönemann (2012), and explicated in the previous paragraph (see above). According to Eq. (2.12), superintensity is a function of the SCAPE gradient perpendicular to angular momentum isopleths. Note, as the angular momentum is rising outward with increasing radial distance outside the core, it can be also inferred from Eq. (2.12) that superintensity is a function of the radial SCAPE gradient.

The analytical model of Frisius and Schönemann (2012) generates maximum values of SCAPE generally a few kilometres outside the radius of maximum tangential wind, with a rapid decline towards the inner edge of the eyewall, and a comparatively moderate and uniform decline outward, in the direction towards the radius of neutral stratification (cf. their Fig. 3c). The analytical solutions of their model exhibit that superintensity rises monotonically with increasing amounts of SCAPE, which depends on the choice of the radius of neutral stratification relative to the radius of maximum wind speed, and the width of the eyewall updraft. The latter mainly determines the radial SCAPE gradient in vicinity of the eyewall (cf. their Figs. 2c and 3c), and is related to the prescribed radial entropy increase within the eyewall, and the ratio between the outer radius of the eye and the radius of maximum wind speed. The radius of neutral stratification, and the increase exponent, κ, which chiefly determines the entropy increase in the eyewall, are crucial parameters to invoke the occurrence of SCAPE. If either the radius of neutral stratification is set equal to the radius of maximum tangential wind, or κ is assumed to take the same value as calculated for the entropy increase exponent in Emanuel's PI (which we may refer to as ν), the eye vanishes in the sense that the distinction between entropy and momentum profiles between the eye and the eyewall is cancelled or breaks down, and SCAPE becomes zero throughout the entire domain. On the other hand, if the eye radius is set to zero, but κ is still presumed to take higher values than

in Emanuel's PI (i.e. $\kappa > \nu$), and the radius of neutral stratification is chosen to be higher than r_{max} as well, smaller amounts of SCAPE and associated superintensity do arise.

The existence of an eye is beneficial, but neither necessary nor sufficient for the generation of SCAPE outside the core. Since the eye is assumed to be in solid body rotation, saturation entropy must increase radially inward as has been shown in previous studies (Smith, 1980; Emanuel, 1997). Frisius and Schönemann (2012) point out that for $\kappa > \nu$, and a non-vanishing eye radius, the inward increase of saturation entropy in the eye becomes higher than the increase in the eye boundary layer entropy, i.e. saturation entropy in the eye exceeds the low-level value. This implicates that the eye warming is considerably stronger than what would occur from moist-adiabatic ascent in case of a vanishing eye radius. The enhanced eye entropy induces a higher entropy gradient in the eyewall, which is translated into a further narrow down of the eyewall front, leading to enhanced SCAPE. As noted by Frisius and Schönemann (2012), for small eye diameters, a further adjustment is required in their analytical model to assure that the saturation entropy in the eyewall does not exceed the boundary layer entropy beneath, where the air rises, which feeds the eyewall. Otherwise, if $s^* > s_b$ in the eyewall region, an additional artificial entropy source within the eyewall updraft would be required, yielding an unphysical solution. Results from the analytical model exhibit that SCAPE, and superintensity reach their hypothetical maximum values, when an eye exists, and the eyewall is assumed to collapse to an infinitely thin discontinuity (i.e. $r_{eye} = r_{max}$), and the radial extent of the inflow area becomes infinitely large, which results in a high value for the radius of neutral stratification. On the other hand, when SCAPE is reduced to zero, the model equations reduce to those that form Emanuel's theory, i.e. no superintensity arises.

The results from model experiments with an axisymmetric convective model shown in Frisius and Schönemann (2012) confirm both the relevance of SCAPE as inferred by their balanced analytical model and the importance of gradient wind imbalance with regard to superintensity, as investigated by Bryan and Rotunno (2009a). They find that, beside gradient wind imbalance, the maximum of superintensity in simulated TCs is also associated with large radial SCAPE gradients, which arise at the outer eyewall, where gradient wind balance appears to be fulfilled fairly well (cf. their Fig. 10). This is in qualitative accordance with Eq. (2.12), though the authors concede that the numerical evaluation of their analytical model returns systematically higher values for superintensity of maximum gradient wind than the numerical modelling results themselves. They note that this quantitative disagreement among the analytical and the numerical model hints at a problem with the underlying assumptions of Eq. (2.12), which needs further investigation. Apart from the quantitative discrepancies, the major conclusions drawn from their analytical model appear to be valid

in high-resolution simulations, i.e. SCAPE outside the eyewall, a steep radial entropy gradient within the eyewall, and the existence of an eye are conducive to the intensity and superintensity of tropical cyclones.

2.8   Summary

Over the past seven decades, several theoretical concepts and approaches to an upper bound of the intensity in mature tropical cyclones have been developed, some of which follow the idea that a tropical cyclone energetically resembles a Carnot-heat cycle (Kleinschmidt, 1951; Emanuel, 1986). This concept involves the view that the primary and secondary circulation are energetically linked, and that the TC circulation follows a closed path. The latter view is opposed by Frank (1977), who points out that the assumption of a closed circulation does not seem to be justified on the basis of observational results. Following the original energetic concept by Riehl (1950), Frisius and Schönemann (2012) argue that a TC may be considered as a flow heater, rather than a Carnot cycle. Unlike Emanuel, they allow for the existence of convective available energy in the surroundings of the eyewall, which acts to enhance TC intensity. The theoretical concept of Carrier et al. (1971) is even further divergent from the Carnot engine view, as the possible energetic link between primary and secondary circulation is considered as irrelevant. In that sense, their model is entirely dependent on environmental SCAPE. Beside a different evaluation of the possible role of convective available potential energy, the relevance of recirculation within the eye is viewed rather differently. While Carrier et al. (1971), and Persing and Montgomery (2003) argue that the latter is of high importance to potential intensity, the eye plays only a passive role in Emanuel's theory. However, there are a few fundamental ideas and idealisations in common to all these different theoretical approaches, i.e. the assumption of adiabatic moist-neutral ascent in the eyewall, which implies the congruence of isentropes and angular momentum isopleths in the updraft region, and the assumption that maximum wind speed can be determined on the basis of gradient wind balance. The latter view is attacked by Smith et al. (2008), and further challenged by Bryan and Rotunno (2009a), who show that Emanuel's PI model provides a good estimate for maximum gradient wind speed, but notably underestimates the imbalanced maximum wind speed, which is found in high-resolution models.

3 Dynamical system analysis of a low-order tropical cyclone model

3.1 Introduction

A tropical cyclone can be considered in an idealised sense as an autonomous dynamical system. Although it is possible to simulate TCs in numerical models quite accurately, only little is known about their dynamical system characteristics. These characteristics are important in order to find out how often tropical cyclones may appear and which intensity they may reach under different climate conditions.

In this chapter, the dependency of tropical cyclone intensity on sea surface temperature; tropospheric temperature stratification; and two different factors that determine the entrainment of low-entropy air, namely the relative humidity in the catchment area of a TC and shallow convection within the ambient region, is investigated within a conceptual model. The low-order model is formulated on the grounds of the perception of a TC as an autonomous dynamical system, whose state can be fully described by a number of exogeneous parameters. With regard to the SST, it is found that the low-order model indeed reproduces a sub-critical bifurcation as hypothesised earlier by Emanuel and Nolan (2004). Furthermore, an amplitude threshold for the generation of a TC is detected within a certain regime depending on SST and the mentioned entrainment factors. The threshold disappears for enhanced SST values and decreased entrainment of low-entropy air via the secondary circulation in the vertical-radial plane. In turn, TCs of relatively high intensity can develop from an initial state very close to that at rest in the conceptual model. The whole regime also proves to be sensitive to parameters constituting the convective exchange within the catchment area in the environment of the storm. The intensity exhibits a sensitivity to SST, atmospheric moisture content, and temperature lapse rate.

Beside the focus on steady state behaviour, the initial growth of TCs within the conceptual model is analysed with regard to two principal feedback mechanisms, whose relevance is still under scientific debate: "conditional instability of the second kind" (CISK) (Charney and Eliassen, 1964), and WISHE or air-sea interaction theory [(Emanuel, 1986), see section 2.5]. CISK postulates the role of constructive interaction between latent heat release related to cumulus convection and the large scale frictional low-level convergence towards the centre of a tropical cyclone as follows (Anthes, 1982; Holton, 2004): The convergence of air masses leads to a forced parcel ascent in the centre; If this forcing is strong enough, air may reach the LFC, where the air parcels become positively buoyant giving rise to cumulus convection and release of latent heat; The warming results in a further pressure decrease in the centre and thus an increased radial pressure gradient and enhanced convergence in the boundary

layer. On the other hand, WISHE explains TC intensification in terms of a positive feedback mechanism between surface wind speed and energy transfer via evaporation from the ocean to the atmosphere due to a thermodynamic disequilibrium between air and sea. Which of these two feedback mechanisms is the dominant one, may be also investigated by means of numerical simulations, for it is largely reflected in the ratio of the exchange coefficients for entropy and momentum, C_H and C_D (Craig and Gray, 1996). An idealised analysis in the conceptual model indicates that the TC intensification arises by a combination of CISK and WISHE.

This chapter is organised as follows: The conceptual model and the processes included are presented in section 3.2. In section 3.3, the tropical cyclone state of the model is estimated and analysed. The model's equilibria, their stability and bifurcations with regard to different parameters are examined in section 3.4. In section 3.5, cyclogenesis mechanisms in the conceptual model and its transient dynamics are investigated. Concluding remarks are given in section 3.6.

3.2   Model formulation

The model is based on the assumption of an axisymmetric vortex, i.e. azimuthal variations are entirely neglected, and is formulated in cylindrical coordinates. The tropical cyclone is divided into three regions above the boundary layer: i) eye; ii) eyewall; and iii) outer region (see Fig. 3.1). The dynamical system is described by three ordinary differential equations and contains inhibiting processes, such as diabatic cooling and convective damping in the ambient region. Therefore, not only the most intense states are considered but also the transient dynamics of development. The eye is assumed to develop passively with the eyewall and is treated as a solid body in rotation. Angular momentum surfaces form the boundaries of the eyewall. Within the Ekman layer, the outer eyewall boundary is located at the radius of maximum winds (RMW). For the model formulation, it is useful to apply the so-called potential radius:

$$R = \sqrt{r^2 + \frac{2vr}{f}} = \sqrt{\frac{2m}{f}}, \tag{3.1}$$

where r denotes the physical radius, v the tangential velocity, f the Coriolis parameter, and m the specific angular momentum[17] as given by Eq. (2.2). The potential radius was introduced by Schubert and Hack (1983) in an axisymmetric vortex model. For $f = const.$, R varies only with m, and can therefore be considered as a measure of angular momentum. R is defined in a manner so that, if the absolute angular momentum is conserved and $r = R$, the tangential

---

[17]In the following, we may sometimes refer to the angular momentum per unit mass simply as angular momentum, skipping the designation "specific". Note that m denotes the angular momentum per unit mass (angular mometum density) throughout this chapter.
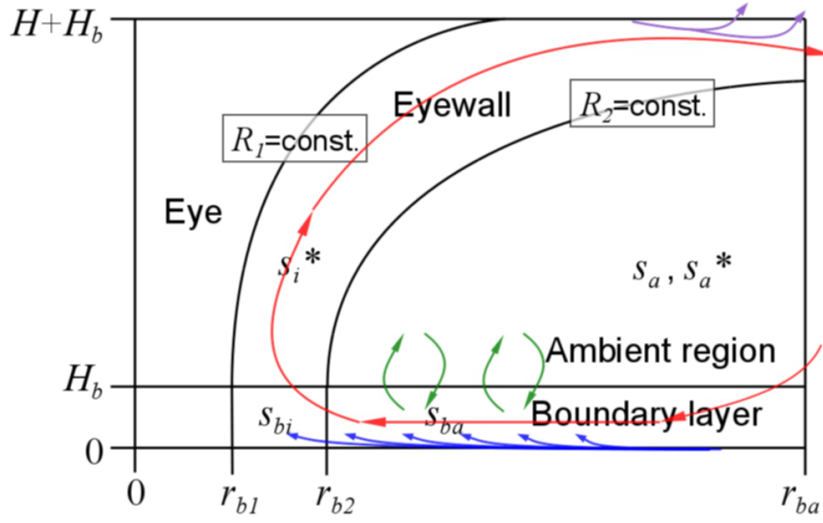
Figure 3.1: Sketch of the low-order tropical cyclone model, where s denotes specific entropy, R the potential radius and r the physical radius. The indexes b, i and a stand for boundary layer, inner and ambient region, respectively. Evaluation at saturation is indicated by an asterisk. Further notation is given in the text. The driving exchange processes are sketched with coloured arrows: Mass transfer along the secondary circulation (red arrows), air-sea interaction (blue arrows), shallow convection within the ambient region (green arrows), and radiative cooling (purple arrows).

velocity vanishes. In other words, the tangential wind v of an air parcel is changed to zero by moving it to R along isopleths of absolute angular momentum. We may interpret the model as a box-model since the boundaries between the three regions are fixed in potential radius space.

3.2.1   Boundary layer flow

The dynamical equations are subject to the hydrostatic and the Boussinesq approximations. The latter leads to non-divergence of the radial-axial flow, i.e.:

$$\frac{1}{r}\frac{\partial}{\partial r}\left(ru_b\right) + \frac{\partial w_b}{\partial z} = 0, \tag{3.2}$$

where u_b is the radial velocity, w_b the vertical velocity within the boundary layer, and z the height. In a non-divergent flow, the velocity field is reduced to its rotational part, described by the vector potential $\boldsymbol{\Upsilon}$:

$$\mathbf{v} = \mathbf{rot}\,\boldsymbol{\Upsilon} = \begin{pmatrix} \frac{1}{r}\frac{\partial \Upsilon_z}{\partial \varphi} - \frac{\partial \Upsilon_\varphi}{\partial z} \\ \frac{\partial \Upsilon_r}{\partial z} - \frac{\partial \Upsilon_z}{\partial r} \\ \frac{1}{r}\frac{\partial (r\,\Upsilon_\varphi)}{\partial r} - \frac{1}{r}\frac{\partial \Upsilon_r}{\partial \varphi} \end{pmatrix}. \tag{3.3}$$

As we presume the flow to vary only in the direction of r and z, the non-divergent flow field in the radial-vertical plane, which describes the secondary circulation, can simply be expressed in terms of a scalar property, we refer to as stream function Υ_φ:

$$u = -\frac{\partial \Upsilon_\varphi}{\partial z}, \; w = \frac{1}{r}\frac{\partial (r\,\Upsilon_\varphi)}{\partial r}, \tag{3.4}$$

which satisfies the continuity equation (3.2). The integrated mass transport along the secondary circulation Ψ can then be calculated at any point x from the azimuthally integrated product of density ρ and Υ_φ after reorganising Eq. (3.4), which gives

$$\Psi(r_x, z_x) = \int_0^{2\pi} \rho\,\Upsilon_\varphi r d\varphi = -\int_{z_0}^{z_x}\int_0^{2\pi} \rho u r d\varphi dz \bigg|_{r=r_x} = \int_{r_0}^{r_x}\int_0^{2\pi} \rho w r d\varphi dr \bigg|_{z=z_x}, \tag{3.5}$$

where $r_0 = 0$ denotes the inner lateral domain boundary, and $z_0 = 0$ the bottom of the cylindrical domain. Presuming a uniform density ρ_b within the boundary layer, we obtain a boundary layer mass stream function Ψ_b with the following properties:

$$2\pi r \rho_b u_b = -\frac{\partial \Psi_b}{\partial z}, \qquad 2\pi r \rho_b w_b = \frac{\partial \Psi_b}{\partial r}. \tag{3.6}$$

The boundary layer is chosen to be of a constant height H_b, and a simple vertically averaged model, also referred to as a "slab" boundary layer model, is used. We adopt the model of Schubert and Hack (1983), in which a simplified aerodynamic drag law as a function of the balanced tangential wind at the boundary layer top ($z = H_b$) is assumed. The equation for boundary layer tangential wind v_b becomes

$$\zeta_b u_b = -\frac{C_D}{H_b}\mid v_b \mid v_b \,, \tag{3.7}$$

where C_D is the surface exchange coefficient for momentum (cf. section 2.5) also called drag coefficient, and ζ_b is the absolute vorticity of gradient wind, which is given by:

$$\zeta_b = \frac{\partial v_b}{\partial r_b} + \frac{v_b}{r_b} + f. \tag{3.8}$$

The index b symbolises evaluation at $z = H_b$. Using this closure and ignoring vertical variation of the horizontal wind components, we obtain the vertical velocity w_b at $z = H_b$ by vertical integration of the continuity equation (3.2). A comparison to Eq. (3.6) leads to the following expression for the mass stream function at the top of the boundary layer:

$$\Psi_b = 2\pi r_b \rho_b C_D \frac{|v_b| v_b}{\zeta_b}. \tag{3.9}$$

We are aware of the limitations of this simple balanced boundary layer model (cf. Smith and Montgomery (2008), and subsection 2.7.2) but think it is, at first instance, appropriate in the context of a low-order model.

3.2.2 The eye

In the eye, we assume solid body rotation. Therefore, the tangential wind becomes

$$v_b = v_e \frac{r_b}{r_{b1}} = v_e \frac{R}{R_1} \ , \tag{3.10}$$

where r_{b1} and R_1 denote the physical radius and potential radius of the eye boundary, respectively (see Fig. 1). The velocity v_{b1} coincides with the eyewall velocity at $R = R_1$. The eye plays only a passive role in the present box-model. This means, we neglect energy and mass fluxes from the eye into the eyewall. Hence, the model is not designed to investigate the role of eye-eyewall interaction processes. We skip this option because in this way, it is not necessary to determine mass fluxes, radial wind and entropy in the eye, and the thermodynamic budget equations to describe the system can be reduced to a number of three, as developed and defined in the following subsections.

3.2.3 The eyewall

Within the eyewall, we assume validity of the gradient wind balance, saturated pseudoadiabatic ascent and angular momentum conservation. These conditions allow for application of the thermal wind balance equation derived by Emanuel [cf. Eq. (10) in Emanuel (1986), and Eq. (7) in Bister and Emanuel (1998)] which relates specific saturation entropy s^* to angular momentum density m:

$$\frac{T_b - T}{m} \frac{ds^*}{dm} = 2 \frac{T_b - T}{f^2 R^3} \frac{ds^*}{dR} = \frac{1}{r^2} - \frac{1}{r_b{}^2} \ , \tag{3.11}$$

where T denotes the absolute temperature. Note that the saturation entropy s^* is only a function of angular momentum m. In Eq. (3.11), the radius r as well as the temperature T, are considered as a function of potential radius R and height z. The thermal wind balance equation (3.11) delivers the shape of the angular momentum surfaces as a function of R and the saturation entropy gradient at R. It can also be written as:

$$G \left(z - H_b \right) = \frac{1}{r \left(z \right)^2} - \frac{1}{r_b{}^2} \ , \tag{3.12}$$

with

$$G = \frac{2\Gamma}{f^2 R^3} \frac{ds^*}{dR} \ , \tag{3.13}$$

where Γ denotes the temperature lapse rate. The tropopause temperature T_t is presumed to be constant and independent of variations in the sea surface temperature T_s, unless stated otherwise. The vertical temperature profile is approximated as linear with a constant lapse rate Γ throughout the troposphere. Using these assumptions, Γ is simply calculated from the difference between T_t and T_s divided by the tropopause height. This equation is evaluated at the inner and outer eyewall boundary where the potential radius takes the value $R = R_1$ and $R = R_2$, respectively.

We approximate the radial entropy gradient at $R = R_2$ with a finite difference expression

$$\left.\frac{ds^*}{dR}\right|_{R=R_2} \approx -\frac{s_i^* - s_a^*}{\Delta R} \ , \tag{3.14}$$

where ΔR is the characteristic distance between the eyewall region and the outer region, s_i^* and s_a^* the mean saturated moist entropy anomaly of the eyewall and the outer region, respectively. So we obtain at $R = R_2$:

$$G_2 \left(z - H_b\right) = \frac{1}{r_2 \left(z\right)^2} - \frac{1}{r_{b2}^2} \ , \tag{3.15}$$

with

$$G_2 = \frac{2\Gamma}{f^2 R_2^3} \frac{s_a^* - s_i^*}{\Delta R} \ . \tag{3.16}$$

The index 2 indicates evaluation at the outer eyewall boundary and, consequently, $r_2(z)$ denotes the physical radius of the angular momentum surface at $R = R_2$. Eq. (3.15) prescribes the shape of the angular momentum surface at the outer eyewall boundary. However, there are still two unknowns, namely r_2 and r_{b2}. For closure, we assume that the mass M enveloped by this angular momentum surface is conserved [18]. Using the simplifying assumption of a constant density ρ (Boussinesq approximation), the mass M as a function of G_2 and r_{b2} becomes[19]:

$$M = \pi \rho \int_{H_b}^{H+H_b} r_2^2 dz = \frac{\pi \rho}{G_2} ln \left(1 + G_2 r_{b2}^2 H\right) \ . \tag{3.17}$$

---

[18]The reasonability of this assumption is briefly addressed in subsection 3.2.5, and in the appendix of Schönemann and Frisius (2012); Yet, we note that this issue needs to be further investigated as will be discussed in section 4.5.

[19]Note that the coarse assumption of a constant density does not have a large impact on the tangential wind v_b, as detected by (Frisius, 2005). Furthermore, the relation $r_{b2}^2 = (GH)^{-1}$ is almost satisfied for a fully developed tropical cyclone so that the assumption of a constant density is not relevant in the mature state.

A more detailed derivation of Eq. (3.17) is given in Frisius (2005) [cf. their Eqs. (22) and (42)]. With this relation we can determine the physical radius r_{b2} and tangential wind speed v_{b2} [see Eq. (3.1)] at the outer eyewall boundary by the following equations:

$$r_{b2} = \sqrt{\frac{1}{G_2 H} \left[exp \left(\frac{G_2 M}{\pi \rho} \right) - 1 \right]} \,, \tag{3.18}$$

$$v_{b2} = \frac{f}{2} \frac{R_2{}^2 - r_{b2}{}^2}{r_{b2}} \,. \tag{3.19}$$

By combination of Eqs. (3.13), (3.18) and (3.19), v_b can be computed as a function of the radial saturation entropy gradient at given potential radii. It can be seen that v_b decreases with decreasing ds^*/dR (not pictured here). For reasons of simplicity, the maximum wind speed is set equal to the maximum gradient wind speed in the low-oder model. As outlined in subsection 2.7.2, this assumption is expected to result in an underestimate of PI, which has been shown to reach higher values associated with the occurrence of supergradient winds in high-resolution models (Bryan and Rotunno, 2009a). However, it is not clear whether the consideration of gradient wind imbalance is crucial to capture the dynamical system properties of a tropical cyclone in an axisymmetric framework. Therefore, and in light of the aim to keep the complexity of the conceptual model as low as possible in our first approach to this issue, it is appropriate to assume gradient wind balance for the calculation of maximum wind speed. In turn, we consider v_{b2} at R_2 as the maximum tangential velocity. Consequently, the maximal ds^*/dR occurs at R_2 and must be smaller elsewhere. Looking at Eq. (3.14), this condition is fulfilled when the radial entropy gradient at the inner edge of the eyewall ($R = R_1$) is calculated by:

$$\left. \frac{ds^*}{dR} \right|_{R=R_1} = -\frac{s_i^* - s_a^*}{\Delta R} \left(\frac{R_1}{R_2} \right)^{\kappa - 1} \,, \tag{3.20}$$

where R_1 is the potential radius of the inner eyewall and κ is the power of the radial decrease ($\kappa \geq 1$) in saturation entropy with increasing distance from the radius of maximum winds at R_2. In analogy to Eq. (3.16) and under consideration of Eq. (3.20), we obtain at the inner eyewall boundary:

$$G_1 = \frac{2\Gamma}{f^2 R_1{}^3} \frac{s_a^* - s_i^*}{\Delta R} \left(\frac{R_1}{R_2} \right)^{\kappa - 1} \,. \tag{3.21}$$

To avoid that the eyewall forms a discontinuity, the angular momentum surfaces should not cross, i.e. G_2 must be equal to or greater than G_1. This also provides an upper limit for κ [$\kappa \leq 4$, see also (Emanuel, 1997)]. As mass fluxes from the eye into the eyewall are not considered in the box-model (see subsection 3.2.2), we assume the mass of the eye enclosed

by R_1 is conserved. With this simplification and the Boussinesq approximation, the eye mass in the free atmosphere above the boundary layer can be calculated analogously to Eq. (3.17):

$$M_e = \pi\rho \int\limits_{H_b}^{H+H_b} r_1{}^2 dz = \frac{\pi\rho}{G_1} ln \left(1 + G_1 r_{b1}{}^2 H\right) ,$$

(3.22)

From this, we can determine the physical radius r_{b1} and tangential wind speed v_{b1} at the inner eyewall boundary by the following equations:

$$r_{b1} = \sqrt{\frac{1}{G_1 H} \left[exp \left(\frac{G_1 M_e}{\pi\rho}\right) - 1 \right]} ,$$

(3.23)

$$v_{b1} = \frac{f}{2} \frac{R_1{}^2 - r_{b1}{}^2}{r_{b1}} .$$

(3.24)

3.2.4   The ambient region

Ascent does not take place in the ambient region which might be partially sub-saturated. The mean specific entropy s_a is attributed to this region and is smaller than its saturation value s_a^*. These values are treated as constants. We intend to include prognostic equations for these entropies in the future. For the present low-order model, we only need to calculate the boundary layer mass flux from the ambient region into the eyewall region. By Eq. (3.9) it does not only depend upon tangential wind v_{b2} and physical radius r_{b2}, but also on absolute vorticity ζ_{b2}. To determine ζ_{b2}, a wind profile in the vicinity of r_{b2} must be known. We assume the profile to be in the shape of

$$v_b = \frac{v_{b2} r_{b2}{}^\beta}{r_b^\beta} \text{ for } r_b > r_{b2},$$

(3.25)

where the exponent of radial decline β takes a value between 0.5 and 1.

By combination of Eq. (3.8) and Eq. (3.25), the absolute vorticity ζ_{b2} at the outer eyewall boundary becomes

$$\zeta_{b2} = f + (1 - \beta) \frac{v_{b2}}{r_{b2}}.$$

(3.26)

This expression can be substituted in Eq. (3.9) to determine the mass transport into the eyewall region. The mass transport turns out to be sensitive to changes in β. A theoretically determined value by Emanuel (1986) becomes $\beta \approx 0.5$. For such a small value, however, the radial inflow to the eyewall region is too weak when we assume realistic values for the maximum tangential wind and the radius of maximum winds. For example, assuming $v_{b2} = 50$ m/s and $r_{b2} = 10$ km and default values for the other model parameters (Tab. 3.1) gives a

radial wind speed at $R = R_2$ of only about 2 m/s. A maximum value of $\beta = 1$ on the other hand, results in an unrealistically high radial wind even twice as high as the tangential wind.

Notation	Value	Meaning
r_a	420 km	Outer radius where $p_s = p_{ref,s}$
r_{ba}	420 km	Outer radius of the ambient region
τ_E	48 h	Timescale, diabatic cooling
τ_C	4 h	Timescale, convective exchange
C_H	0.003	Transfer coefficient for enthalpy
C_D	0.003	Transfer coefficient for momentum
H	13.5 km	Tropopause height minus boundary layer height
H_b	1.5 km	Boundary layer height
f	$5 \cdot 10^{-5}$ s^{-1}	Coriolis parameter
κ	3	Eyewall entropy profile parameter
δ	0.25	Entrainment parameter
R_1	90 km	Inner potential radius of eyewall
R_2	180 km	Outer potential radius of eyewall
ΔR	30 km	Distance eyewall - outer region
ρ	0.45 kg/m^3	Mean density
ρ_b	1.1 kg/m^3	Mean boundary layer density
T_t	203.15 K	Tropopause temperature
T_s	301.15 K	Sea surface temperature
h_a	45%	Relative humidity, ambient region
p_a	500 hPa	Pressure level, ambient region
$h_{ref,b}$	80%	Relative humidity, boundary layer
p_{ref}	1000 hPa	Reference surface pressure
β	0.875	Tangential wind profile parameter

Table 3.1: Default model parameters

3.2.5   Thermodynamic equations

The low-order model is based upon thermodynamic variables. All needed hydrodynamic variables can be deduced diagnostically from Eqs. (3.9), (3.16), (3.18), (3.19), (3.21), (3.23), (3.24) and (3.26). First, a prognostic equation for saturation entropy of the eyewall s_i^* is needed. It is changed by the mass flux from the boundary layer and diabatic processes like radiation or turbulent mixing. The mass flux results from Eq. (3.9) evaluated at $r = r_{b2}$. At the inner edge of the eyewall, we assume vanishing mass exchange with the eye. Furthermore, we presume that the inflow from the boundary layer into the eyewall is exactly compensated by the outflow in the upper troposphere. This implicates that the eyewall mass enclosed by

angular momentum surfaces above the boundary layer is conserved. It is calculated in terms of potential radii:

$$M_i = M - M_e = M - \pi \rho H {R_1}^2 = \pi \rho H \left({R_2}^2 - {R_1}^2\right). \tag{3.27}$$

M_i given by Eq. (3.27) is equivalent to the mass of the resting state with vertically oriented eyewall boundaries, i.e. $r_1 = R_1$ and $r_2 = R_2$. This assumption seems to be the most reasonable one since TCs typically grow in a horizontally uniform tropical atmosphere close to rest. As the model cyclone intensifies, the boundaries slant and the eyewall obtains the shape of a hyperboloid as drafted in Fig. 3.1.

The diabatic processes are parameterised with a linear relaxation to the state of the ambient region. Furthermore, we assume saturation, so that we can equate entropy with saturation entropy. Then, we obtain the following prognostic equation:

$$\frac{ds_i^*}{dt} = \Psi_{b2} \frac{s_{bi} - s_i^*}{M_i} + \frac{s_a^* - s_i^*}{\tau_E}, \tag{3.28}$$

where s_{bi} is the mean specific entropy of the boundary layer beneath the eyewall, s_a^* the saturated moist entropy of the ambient region, and τ_E the time scale for damping by diabatic cooling processes. The first term on the rhs of Eq. (3.28) represents the upward transport of high entropy air into the eyewall from the boundary layer beneath via the secondary circulation in the radial-vertical plane. Hence, it is related to deep convection in the inner region. The second term represents diabatic cooling via radiation.

Further equations for specific entropy of the boundary layer are needed. To calculate their tendencies, the mass of the boundary layer beneath the eyewall must be known. It is given by

$$M_{bi} = \pi \rho_b \left({r_{b2}}^2 - {r_{b1}}^2\right) H_b, \tag{3.29}$$

and may change in the course of the development due to changes in r_{b2} and r_{b1}. The specific entropy is altered by surface heat fluxes and lateral inflow from the ambient region. These are applied by the following equation:

$$\frac{ds_{bi}}{dt} = \Psi_{b2} \frac{s_{ba} - s_{bi}}{M_{bi}} + \frac{C_H}{2H_b} \left(|v_{b2}| + |v_{b1}|\right) \left(s_{oi} - s_{bi}\right), \tag{3.30}$$

where s_{ba} denotes the specific boundary layer entropy of the outer region[20], C_H the surface transfer coefficient for entropy (cf. section 2.5), and s_{oi} the mean specific entropy at the

---

[20]Strictly speaking, it should be the boundary layer entropy at $R = R_2$. However, we do not resolve the radial entropy profile in this low-order model and, therefore, assume a representative value for the whole box.

ocean surface beneath the eyewall. Advective transport within the boundary layer via secondary circulation is represented by the first term on the rhs of Eq. (3.30). The second term represents the surface transfer of latent heat into the boundary layer due to the prescribed thermodynamical disequilibrium between the sea surface and the atmospheric boundary layer. It has been simplified by using an averaged wind speed over the box.

The specific boundary layer entropy s_{ba} outside the eyewall is altered by surface heat fluxes, radial advection, convective cooling and downwelling of low-entropy air from the free atmosphere above the boundary layer related to the mass transfer along the secondary circulation. The following equation for the mean entropy s_{ba} in the outer region's boundary layer is introduced

$$\frac{ds_{ba}}{dt} = \Psi_{b2}\frac{\delta s_a + (1-\delta)s_{ba0} - s_{ba}}{M_{ba}} + \frac{C_H}{2H_b}|v_{b2}|\,(s_{oa} - s_{ba}) + \frac{s_a - s_{ba}}{\tau_C}, \qquad (3.31)$$

where $0 \leq \delta \leq 1$ is an entrainment parameter describing the entrainment of air into the ambient boundary layer. Taking $\delta = 1$ would be equivalent to the assumption that air transported by the secondary circulation came entirely vertically from the free troposphere above the outer boundary layer, whereas taking $\delta = 0$ would correspond to assuming the entire air flew in sidewise from the far-field surroundings. In the following, we arbitrarily presume $\delta = 0.25$, i.e. 25% of the secondary circulation inflow into the outer boundary layer comes from above, and 75% laterally from the far-field beyond r_{ba}. s_{oa} and s_a are the mean specific entropies at the ocean surface and in the free troposphere above the boundary layer, s_{bao} the far-field boundary layer entropy, and τ_C the time scale for exchange processes across the top of the boundary layer due to shallow convection, which is represented by the third term in Eq. (3.31). The boundary layer mass in the ambient region is given by

$$M_{ba} = \pi\rho_b(r_{ba}{}^2 - r_{b2}{}^2)H_b \qquad (3.32)$$

and may change in the course of the development due to changes in r_{b2}. The radius r_{ba} determines the width of the ambient boundary layer and, therefore, its thermal inertia.

Yet, we have to determine the specific entropy s_o at the sea surface and the specific entropy s_a in the ambient region above the boundary layer, which will be done in the following. The sea surface entropy changes with time due to its dependence on surface pressure p_s. We use the approximated expression

$$s_o(T_s, p_s) = c_p ln\left(\frac{T_s}{T_{ref}}\right) - R_d ln\left(\frac{p_s}{p_{ref}}\right) + L_v\left(\frac{q_v^*}{T_s} - \frac{q_{v,ref}}{T_{ref}}\right), \qquad (3.33)$$

where T_s denotes the sea surface temperature and q_v the specific humidity. The index ref symbolises that the quantity is a constant reference quantity and the asterisk denotes that the moisture variable is considered at saturation. The reference entropy s_{ref} is chosen to coincide with the boundary layer entropy of the undisturbed environment, i.e. $s_{ba0} = 0$ Jkg^{-1}K^{-1}. Here, the temperature is identical to the sea surface temperature T_s and the relative humidity takes the value $h_{ref,b}$. Therefore, we obtain

$$s_o = L_v \left(\frac{q_v^* - q_{v,ref}}{T_s} \right) - R_d ln \left(\frac{p_s}{p_{ref}} \right),   \tag{3.34}$$

with the specific reference humidity $q_{v,ref}$.

We assume gradient wind balance to calculate the surface pressure p_s. Hence

$$\frac{R_d T_s}{p_s} \frac{\partial p_s}{\partial r} = \frac{v_b^2}{r} + f v_b,   \tag{3.35}$$

where R_d is the specific gas constant. A radial integration to infinity would lead to a diverging integral when the tangential wind takes a profile of the shape described by Eq. (3.25). Therefore, the integration is only applied to a finite radius r_a where the surface pressure coincides with the reference value. By integration of Eq. (3.35) we obtain

$$R_d T_s ln \left(\frac{p_{s2}}{p_0} \right) = -\frac{v_{b2}^2}{2\beta} \left[1 - \left(\frac{r_{b2}}{r_a} \right)^{2\beta} \right] + \frac{f v_{b2} r_{b2}}{1 - \beta} \left[1 - \left(\frac{r_a}{r_{b2}} \right)^{1-\beta} \right].   \tag{3.36}$$

The surface pressure can be used to evaluate the entropy s_{o2} at the radius r_{b2}. For the surface entropy of the eyewall region we assume $s_{oi} = s_{o2}$ and for the outer region $s_{oa} = (s_{o2} + s_{oa0})/2$, respectively, where s_{oa0} is the entropy at the surface for $R \to \infty$, namely

$$s_{oa0} = L_v \left(\frac{q_v^* - q_{v,ref}}{T_s} \right).   \tag{3.37}$$

The undisturbed environment may be in a state of convective-radiative equilibrium which is neutral to convective instability. It excludes an acquisition of kinetic energy from environmental convective available potential energy. Observations indicate that CAPE does not vanish during the mature state of a TC [e.g. Bogner et al. (2000); Frank (1977); Sheets (1969)] and increases with radial distance from the centre of the storm. Hence, assuming neutrality to convection, or more accurately to slantwise convection in potential radius space, may be appropriate for the eyewall region, but not suitable for the ambient region. Moreover, as discussed in subsection 2.7.3, the analysis on the possible impact of SCAPE on potential intensity by Frisius and Schönemann (2012) yields that PI rises with environmental SCAPE.

Therefore, we have investigated different cases which differ in their far-field equilibrium strat-ification:

- case I, where we assume a constant lapse rate and boundary layer relative humidity ($h_{ref,b}$),

- case N1, where neutrality to convection is maintained by adjusting boundary layer relative humidity,

- case N2, where neutrality to convection is maintained by adjusting the temperature lapse rate,

- hybrid case H, which excludes convective instability, such as in case N2, but allows for stability in the ambient region like in case I.

Convective instability in the far environment can only arise in case I. For case N2 and case H we implement a lower convective damping, i.e. $\tau_C = 8$ h instead of $\tau_C = 4$ h. The reasons will be outlined in section 3.4. The entropy in the ambient region s_a is given by

$$s_a = L_v \left(\frac{q_{v,a}}{T_a} - \frac{q_{v,ref}}{T_{ref}} \right) - R_d ln \left(\frac{p_a}{p_{ref}} \right) + c_p ln \left(\frac{T_a}{T_{ref}} \right), \tag{3.38}$$

where the index a denotes that the quantity is evaluated in the ambient region at a character-istic pressure level above the boundary layer p_a. The temperature T_a is calculated for a given pressure level p_a in analogy to a formula proposed by Reed and Jablonowski (2011) [see their Eq. (5)]. We found that the difference between virtual and absolute temperature is relatively small in the calculation of T_a. It does not affect the outcoming tendencies discussed in this study. In the course frame of the box-model, the difference between absolute and virtual temperature can therefore be neglected and T_a is considered to be determined sufficiently accurate by

$$T_a = T_s \left(\frac{p_a}{p_{ref}} \right)^{\frac{R_d \Gamma}{g}}, \tag{3.39}$$

with the gravitational acceleration $g = 9.806 \ m/s^2$. Due to subsaturation in the ambient region on average, s_a is smaller than the corresponding saturation entropy s_a^*. As stated above, the boundary layer entropy in the far-field environment at the outer boundary of the box-model s_{ba0} is put to zero. Consequently, the saturated entropy of the ambient region s_a^* must be also zero to provide for the case of convective neutrality. In this reference frame, s_a

measured as an anomaly of s_{ba0} becomes negative[21]. In case N1, we consider the moisture conditions of a pseudoadiabatically ascending parcel as reference state and determine the relative humidity in the boundary layer analytically. In this way, it is assured that the value of the reference entropy equals that taken in the calculation of the surface entropy. In the non-neutral case I, s_a^* is calculated in reference to the prescribed conditions within the boundary layer beneath and relative humidity in the boundary layer at r_{ba} is set to a value of 80%. In the other neutral case N2, T_a is not calculated from Eq. (3.39). Instead it is determined numerically to provide for neutrality like in case N1 considered here (see above). In the hybrid case H, this will be done only where convective instability would occur. Elsewhere, the hybrid case H is identical to case I.

3.2.6   The thermodynamical system

The derivations of the previous subsections lead to a closed low-order tropical cyclone model. The low-order model takes the form of a dynamical system with three ordinary differential equations for the three unknowns s_i^*, s_{bi} and s_{ba}. The equations are given by

$$\frac{ds_i^*}{dt} = \Psi_{b2}\frac{s_{bi}-s_i^*}{M_i} + \frac{s_a^*-s_i^*}{\tau_E}, \tag{3.40}$$

$$\frac{ds_{bi}}{dt} = \Psi_{b2}\frac{s_{ba}-s_{bi}}{M_{bi}} + \frac{C_H}{2H_b}\left(|v_{b1}|+|v_{b2}|\right)\left(s_{oi}-s_{bi}\right), \tag{3.41}$$

$$\frac{ds_{ba}}{dt} = \Psi_{b2}\frac{\delta s_a-s_{ba}}{M_{ba}} + \frac{C_H}{2H_b}|v_{b2}|\left(s_{oa}-s_{ba}\right) + \frac{s_a-s_{ba}}{\tau_C}. \tag{3.42}$$

In these equations, the mass stream function Ψ_{b2}, the tangential velocities v_{b1} and v_{b2}, the boundary layer masses M_{bi} and M_{ba}, and the specific entropies at the sea surface, s_{oi} and s_{oa}, can be written as a function of s_i^* by consideration of Eqs. (3.9), (3.16), (3.18), (3.19), (3.21), (3.23), (3.24), (3.26), (3.29) and (3.36). This is advantageous for the calculation of equilibria since we can derive a single equation for the equilibrium values of s_i^*.

The system dynamics depend on a number of model parameters. These are r_a, r_{ba}, τ_E, τ_C, C_H, C_D, H, H_b, f, κ, δ, R_1, R_2, ΔR, ρ, ρ_b, T_t, T_s, h_a, p_a, $h_{ref,b}$, p_{ref} and β (see Tab. 3.1). Fix parameter values for moisture and temperature at the respective pressure levels where chosen in close agreement to observational data (Jordan, 1958). The regions' extent in potential radius space, i.e. R_1 and R_2, were chosen in accordance with those of simulations with a high-resolution axisymmetric model and the radial extent of the model domain according to recent findings by Chavas and Emanuel (2010).

---

[21]To avoid negative values in entropy, one may add a constant value to the reference entropy. However, we note that this would not affect any of the model results, because crucial here are not any absolute entropy values, but only the entropy differences. Therefore, the addition of any constant value would result in an identical behaviour of the model.

3.3   Estimation of the tropical cyclone state

Here, we consider the steady state solution which can be associated to a tropical cyclone at its final intensity. For this purpose, we only consider the effects of transport via secondary circulation and latent heat transfer between ocean and atmosphere, and shallow convection. The obstructive effect of radiative cooling is neglected, i.e. we set $1/\tau_E = 0$ s^{-1}. For a comparison with Emanuel's PI theory [E-PI, Emanuel (1986)] the existence of an eye is neglected by setting $R_1 = 0$ km. The environmental convective available potential energy should vanish as in E-PI, i.e. $s_{ba0} = s_a^*$ ($= 0$ Jkg^{-1}K^{-1}, see subsection 3.2.5). In addition to this, we presume the ambient region to be saturated by setting $s_a = s_a^*$ to have a relaxation towards a neutral state by shallow convection. Furthermore, the entrainment parameter δ is set to zero, i.e. entrainment of air along the secondary circulation does not enter from above the boundary layer but only from the far environment. With these assumptions, we determine steady state solutions of the dynamical system [cf. Eqs. (3.40)-(3.42)] and solve the following equations

$$0 = \Psi_{b2}\frac{s_{bi} - s_i^*}{M_i} \, , \tag{3.43}$$

$$0 = \Psi_{b2}\frac{s_{ba} - s_{bi}}{M_{bi}} + \frac{C_H}{2H_b}|v_{b2}|\,(s_{oi} - s_{bi}) \, , \tag{3.44}$$

$$0 = -\Psi_{b2}\frac{s_{ba}}{M_{ba}} + \frac{C_H}{2H_b}|v_{b2}|\,(s_{oa} - s_{ba}) - \frac{s_{ba}}{\tau_C} \, . \tag{3.45}$$

The Coriolis force at $R = R_2$ is small compared to the centrifugal force for a tropical cyclone vortex. In turn, the higher order term $r_{b2}{}^2$ becomes very small against $R_2{}^2$ and therefore negligible. Eqs. (3.19) and (3.26) can be simplified accordingly:

$$v_{b2} = \frac{f}{2}\frac{R_2{}^2}{r_{b2}}, \quad \zeta_{b2} = (1 - \beta)\frac{v_{b2}}{r_{b2}} \, . \tag{3.46}$$

Since $r_{b2} << r_2|_{z=H_b+H}$ for a fully developed TC, we can simplify the thermal wind balance equation [see Eqs. (3.15) and (3.16)] to

$$\frac{1}{r_{b2}{}^2} = \frac{2\Gamma H}{f^2 R_2{}^3}\frac{s_i^*}{\Delta R} \, . \tag{3.47}$$

Application of these approximations to Eq. (3.9) leads to the following equation for the mass transport:

$$\Psi_{b2} = \frac{\pi\rho_b f R_2{}^2 C_D}{1 - \beta}r_{b2} \, . \tag{3.48}$$

Then, evaluation of Eqs. (3.43) and (3.44) gives

$$s_i^* = s_{bi} = \frac{s_{ba} + \frac{C_H}{4C_D}(1-\beta)s_{oi}}{1 + \frac{C_H}{4C_D}(1-\beta)} \ . \tag{3.49}$$

Evaluation of Eq. (3.45) using the approximation $r_{ba}^2 - r_{b2}^2 \approx r_{ba}^2$ for a fully developed cyclone leads to

$$s_{ba} = \frac{\frac{C_H}{4C_D}(1-\beta)s_{oa}}{\frac{r_{b2}^2}{r_{ba}^2} + \frac{C_H}{4C_D}(1-\beta) + r_{b2}\frac{H_b(1-\beta)}{R_2^2 f C_D}\frac{1}{\tau_C}} \ . \tag{3.50}$$

We see that shallow convection and entrainment are necessary to attain a boundary layer entropy below that of the sea surface in the outer region. Since $r_{b2} << r_{ba}$, the first term in the denominator of Eq. (3.50) can be neglected. Only for very strong damping, i.e. smaller τ_C values, shallow convection provides the dominant contribution and the approximation

$$s_{ba} = \frac{C_H v_{b2} \tau_C}{2H_b} s_{oa} \tag{3.51}$$

holds. The physically valid solution for tangential wind with this approximation, and neglect of the pressure dependence of surface entropy so that $s_{oi} = s_{oa} \equiv s_o$, becomes:

$$v_{b2} = \frac{C_H \Gamma H R_2 \tau_C s_o}{8H_b \Delta R(1 + \frac{C_H}{C_D}\gamma)} + \sqrt{\left[\frac{C_H \Gamma H R_2 \tau_C s_o}{8H_b \Delta R(1 + \frac{C_H}{C_D}\gamma)}\right]^2 + \frac{C_H}{C_D}\frac{\Gamma H R_2}{2\Delta R}\frac{\gamma s_o}{1 + \frac{C_H}{C_D}\gamma}} \ , \tag{3.52}$$

where $\gamma = (1-\beta)/4$. This formula will be compared to that of E-PI theory (Emanuel, 1995a), which predicts for maximum wind speed squared [cf. Eq. (2.6)]

$$v_{max,E}^2 = \frac{C_H}{C_D}(T_s - T_{out})(s_{o2} - s_{b2}), \tag{3.53}$$

where s_{o2} and s_{b2} are the entropies at the sea surface and in the boundary layer at $R = R_2$, respectively. s_{b2} is calculated in such a way that the relative humidity of the boundary layer equals environmental relative humidity and the boundary layer temperature is identical to sea surface temperature. T_{out} denotes the outflow temperature at the top lid of the model. Hence, the factor $T_s - T_{out}$ can be identified with ΓH in Eq. (3.52). The classical E-PI is proportional to $(C_H/C_D)^{1/2}$. A similar formula results for very small τ_C values, because then the second term under the square root in Eq. (3.52) dominates. This is consistent with E-PI since fixation of boundary layer relative humidity outside the eyewall by shallow convection is a crucial assumption in this theory. Fig. 3.2 displays maximum tangential wind as a function of C_H/C_D using standard parameters for different τ_C values. For smaller τ_C values (0.5 h) the increase of tangential wind with C_H/C_D is similar to the approximation (3.52), and it is
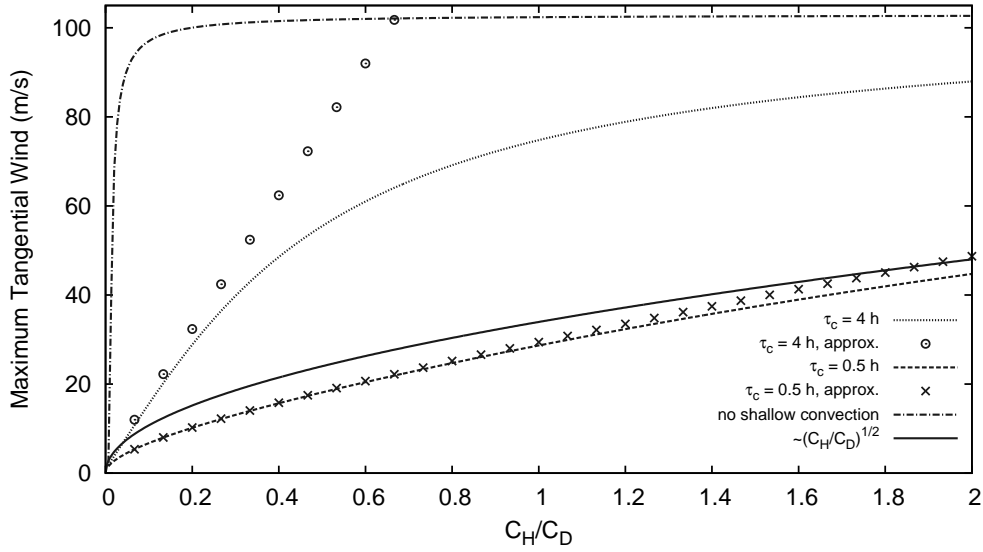
Figure 3.2: Maximum tangential wind (m/s) of the tropical cyclone state as a function of C_H/C_D for various timescales for shallow convective damping τ_C. The solid line displays $v_{b2} \propto \sqrt{C_H/C_D}$. The circles and crosses mark the analytical approximation given by Eq. (3.52) for $\tau_C = 4$ h and $\tau_C = 0.5$ h, respectively.

roughly proportional to $(C_H/C_D)^{1/2}$. For larger convective damping time scales, i.e. higher τ_C values, Eq. (3.52) becomes a poor approximation. When shallow convection is switched off, we obtain a very rapid increase of v_{max} with C_H/C_D and constancy afterwards. This behaviour seems rather unrealistic as it is unlike that of more complex numerical models [e.g. Bryan and Rotunno (2009b)].

3.4 Equilibria, bifurcations and stability

As a standard parameter set of our model experiments we use the values listed in Table 3.1. The simulations are based on this set as has been elaborated in section 3.2, unless stated otherwise.

First, equilibria are determined by an iterative procedure. The output of the standard simulation with gradual change in constant sea surface temperature shows two up to four equilibria apart from the trivial solution, which is associated with an atmosphere at rest. Conducting a stability analysis by which eigenvalues from the respective Jacobian are numerically determined, we detect that the fourth or uppermost and the second equilibrium are stable (everywhere, apart from the A-regime which will be described below), while the first and third intermediate equilibria are unstable. The second equilibrium represents a low pressure system of rather small intensity and the uppermost is associated with a tropical cyclone of hurricane strength on the Saffir-Simpson scale (see section 1.2). A bifurcation diagram
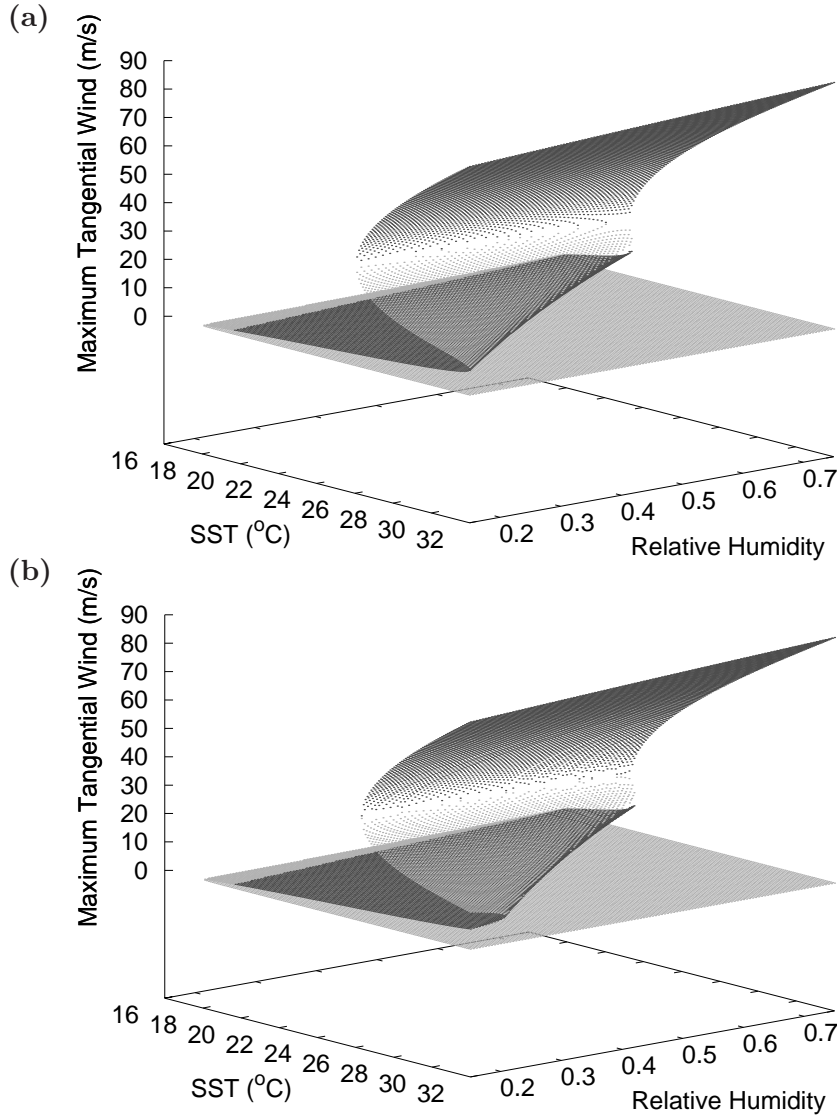
(a)

(b)

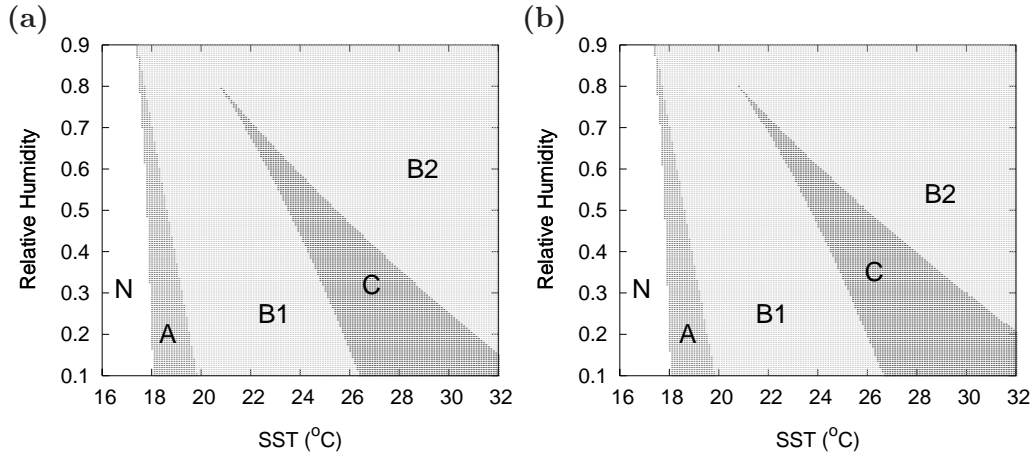Figure 3.3: Equilibrium solutions for maximum tangential wind v_{b2} (m/s) as a function of T_s (°C) and h_a (fraction by one) for (a) the non-neutral case I and (b) case N1 under the assumption of convective neutrality. Stable equilibria are coloured in dark grey and unstable equilibria in a brighter grey.

is shown in figure 3.3, which displays the maximum tangential wind of these equilibria as a function of SST, and relative humidity in the ambient region h_a. It can be seen from the 3-D-plot (Fig. 3.3), and the respective regime diagrams (Fig. 3.4) that the number of equilibria strongly depends on h_a. In all cases, there is a threshold for the formation of cyclones, which is majorly determined by SST. Below a temperature of about 18°C, no stable low pressure system would form in the model. Within a certain regime spanned by h_a and SST, we obtain two unstable equilibria, denoted by an A in the regime diagrams. The lower equilibrium acts as a repellor everywhere it exists. The upper one of these two equilibria exhibits the character

Figure 3.4: Regime diagrams as a function of T_s (°C) and h_a (fraction by one) for (a) the non-neutral case I and (b) case N1 under the assumption of convective neutrality. The different regimes are labelled with different capital letters: The regime, where no stable low pressure systems would form at all, is denoted as N-regime; in the A-regime we obtain two unstable equilibria; in the B-regimes (B1 and B2), the lower equilibrium is unstable and the upper one is stable; in the C-regime, two unstable and two stable equilibria arise.

of an unstable or negative fixed point associated with two complex conjugated Eigenvalues. For slightly higher temperatures and with increasing relative humidity in the ambient region, the fixed point attractor becomes stable where the A-regime turns into the B1-regime. Two additional equilibria arise by a cusp catastrophe in the C-regime (Fig. 3.4) of which the upper one is stable (Fig. 3.3). The additional repellor imposes an amplitude threshold, i.e. it is obstructive to the formation of a storm reaching TC intensity. Only in the B2-regime, where we have two equilibria again, SST and h_a are sufficiently high for the formation of a strong TC from a small initial disturbance in an atmospheric state close to rest.

As can be seen from Fig. 3.5, the principal equilibrium structure as described above, is qualitatively stable to changes in the exponent β, which describes the radial decline of tangential wind velocity. However, there are quantitative changes and tendencies, i.e. the intensity of the TC decreases for lower β-values. This may be due to an enhanced mass transport across r_{b2} into the inner boundary layer with increasing β-values, since Ψ_{b2} is approximately proportional to $(1-\beta)^{-1}$ [cf. Eq. (3.48)]. This result is in qualitative agreement with the behaviour observed in a slab-boundary model (Frisius et al., 2013), which accounts for the effect of gradient wind imbalance (see subsection 2.7.2). Beside an increase in intensity in the upper stable equilibrium, the amplitude threshold is shifted to higher sea surface temperatures for higher β-values. This is true for both cases I and N1 pictured in Figs. 3.3, 3.4 and 3.5. Qualitatively and in terms of maximum wind speed for TCs, there is no visible difference between the non-neutral case I (Figs. 3.3a, 3.4a, 3.5a) and case N1 (Figs. 3.3b, 3.4b, 3.5b),

whereas the amplitude threshold is sensitive to the stability conditions in the ambient region. As can be seen from Fig. 3.4, the C-regime is broadened and the amplitude threshold is shifted towards higher temperatures in case N1. The quantitative differences between case I and case N1 disappear for $\delta = 1$ (not pictured here), presuming that air transported by the secondary circulation into the boundary layer comes entirely vertically from the ambient region above rather than its surroundings (in the figures shown here, δ equals 0.25 as stated in Tab. 3.1). The higher the amount of horizontal air transport into the boundary layer from the surroundings (i.e. the smaller δ), the larger becomes the difference between case I and case N1 with regard to the location and extent of the C-regime in the T_s-h_a-plane.

(a)

(b)
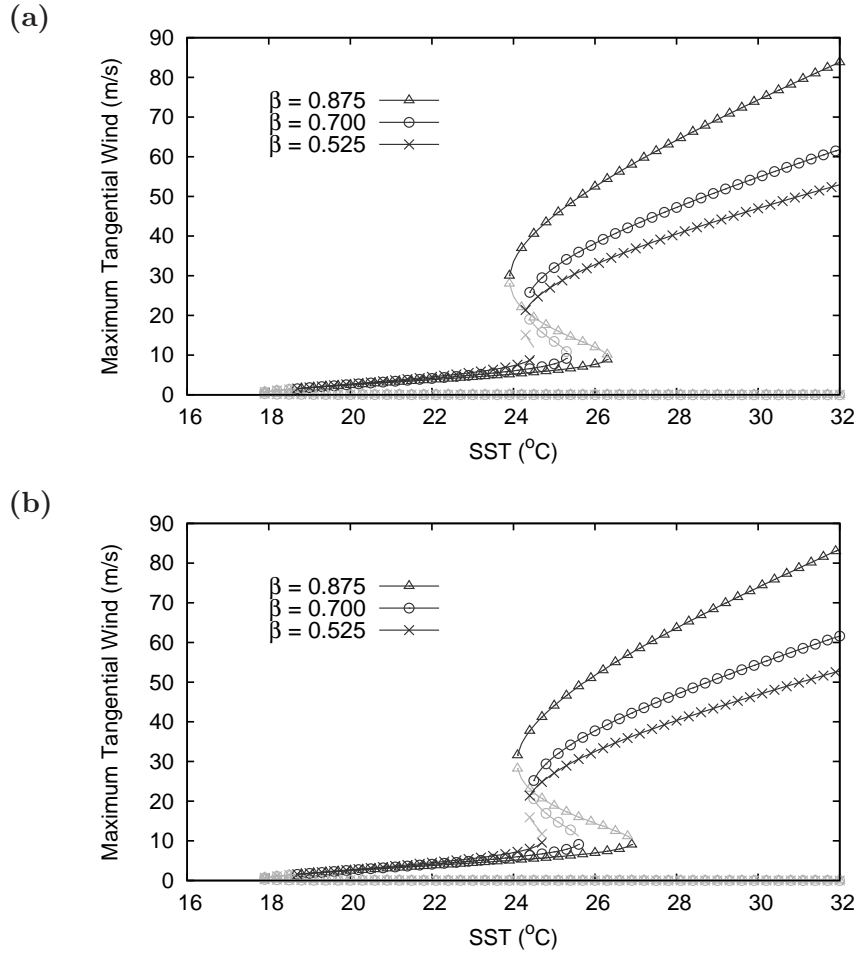
Figure 3.5: Bifurcation diagrams of maximum tangential wind v_{b2} (m/s) as a function of T_s (°C) for different β-values and a relative humidity in the ambient region of $h_a = 45\%$ for (a) the non-neutral case I and (b) case N1 under the assumption of convective neutrality. Stable equilibria are coloured in dark grey and unstable equilibria in a brighter grey.

Model results from case I and case N1 are in qualitative agreement and display relatively small differences with regard to their quantitative behaviour. The decrease in boundary

layer humidity in case N1 at higher SSTs compensates for the decreased dry static stability we obtain when SST increases, while the tropopause temperature is held fix. This way to maintain neutrality to convection, results in unrealistically low values for relative humidity in the outer boundary layer at warm tropical SSTs. At $T_s \approx 25°C$, boundary layer humidity falls below 60% and it decreases even further for higher SSTs in case N1. On the other hand, relative humidity of the boundary layer at r_{ba} does not need to be calculated from other model variables in case I (see section 2.5). Instead a fix value of $h_{ref,b} = 80\%$ is chosen in case I, i.e. changes in dry static stability are not counteracted by changes in boundary layer humidity to keep moist neutrality. For reasons of clarity, we relinquish a further discussion on results of case N1 in the following part of this section and only display results from case I. However, we note that the results obtained from case N1 exhibit the same behaviour as those from case I with regard to changes in the parameters investigated in this study.

Tropical cyclone intensity as well as the number of equilibrium solutions are sensitive to relative humidity in the ambient region above the boundary layer h_a as discussed above. The entropy in the ambient region depends on h_a [see Eq. (3.38)]. Thereby, this model parameter highly influences the entrainment of low-entropy air from the ambient region into the boundary layer beneath via secondary circulation and shallow convection within the ambient region [see Eq. (3.31)]. Another parameter, which determines the entrainment of low-entropy air into the boundary layer, is the time scale for convective damping τ_C [see Eq. (3.31)]. As can be seen from Fig. 3.6, the strength of convective damping has a notable impact on TC intensity as well as the SST-amplitude threshold. For lower values in τ_C, i.e. enhanced shal-
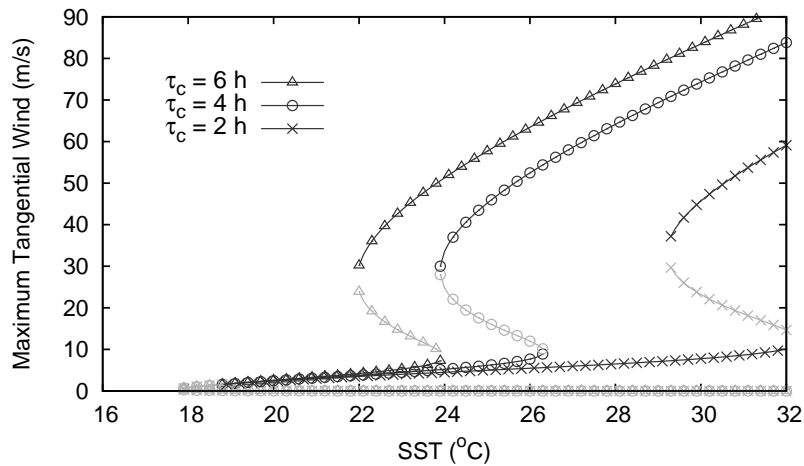

Figure 3.6: Bifurcation diagram of maximum tangential wind v_{b2} (m/s) in case I as a function of T_s (°C) for different τ_C-values and a relative humidity in the ambient region of $h_a = 45\%$. Stable equilibria are coloured in dark grey and unstable equilibria in a brighter grey.
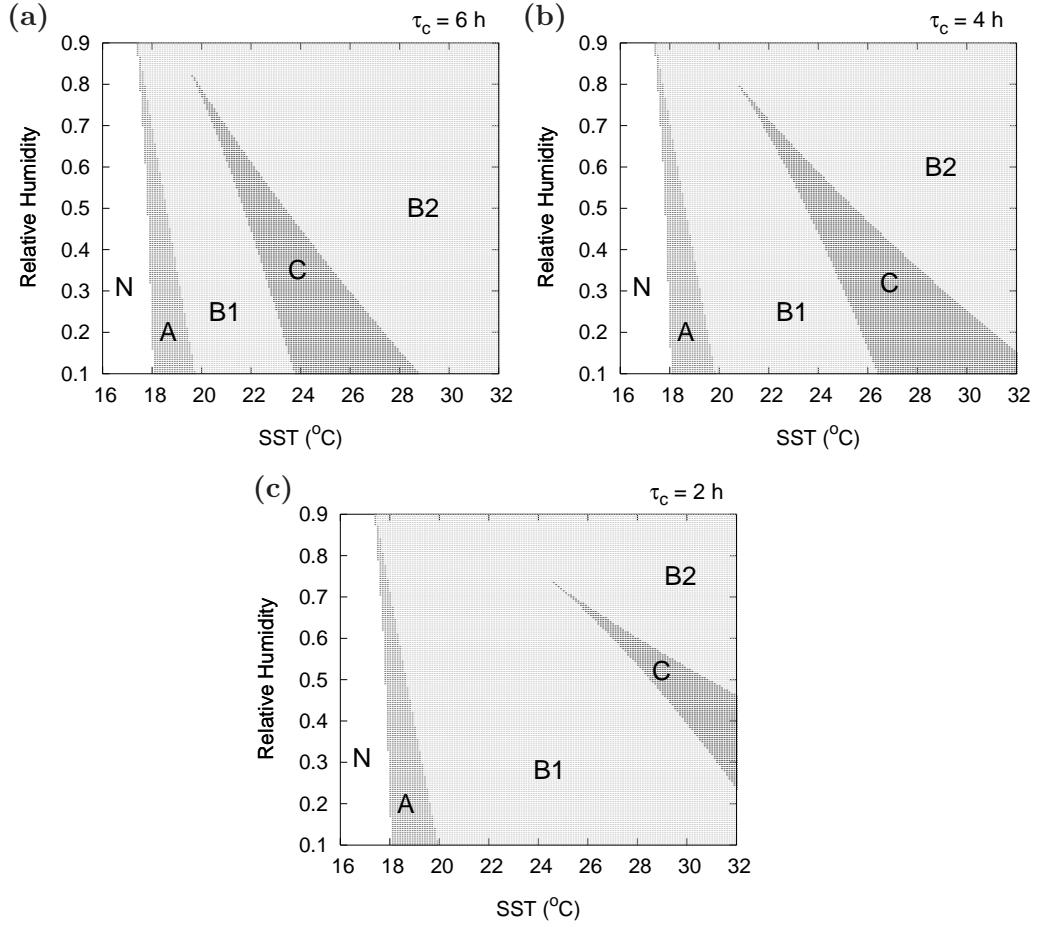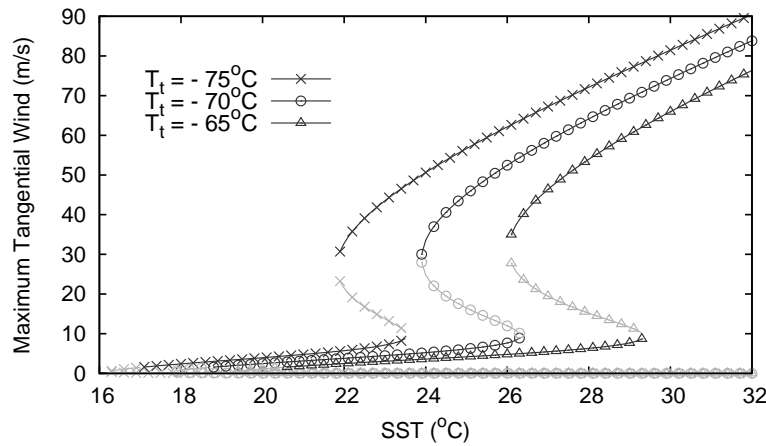
Figure 3.7: Regime diagrams in case I as a function of T_s (°C) and h_a (fraction by one) for different time scales in convective damping: (a) $\tau_C = 6$ h, (b) $\tau_C = 4$ h and (c) $\tau_C = 2$ h. The different regimes are labelled like in Fig. 3.4.

low convective damping, maximum potential intensity decreases and the amplitude threshold is shifted to higher SSTs. The sensitivity of the equilibrium structure to convective damping within the ambient region is further illustrated in regime diagrams in Fig. 3.7. The formation threshold is hardly affected by changes in τ_C, whereas the amplitude threshold is shifted to higher sea surface temperatures and relative humidity in the ambient region.

In Case N2, we make use of another possibility to ensure neutrality with respect to convection. In difference to case N1, the temperature stratification is corrected while the boundary layer relative humidity $h_{ref,b}$ is kept constant. Instead of using Eq. (3.39), the temperature T_a is determined iteratively, so that s_a^* becomes zero. The lapse rate Γ has been corrected accordingly. In Case I, the vertical temperature difference between T_s and T_a increases by definition with increasing SST, while T_t is treated as constant and independent of T_s [see subsection 3.2.3 and Eq. (3.39)]. By contrast in case N2, neutrality to convection is

maintained by adjustment of T_a, which results in a decreased temperature difference between T_s and T_a (not pictured here), acting against instability. Model studies on global climate feedbacks show that the upper tropospheric temperature in the tropics increases in response to global warming and the tropospheric temperature lapse rate decreases (Hansen et al., 1984; Hegerl et al., 2007), which stabilises the vertical stratification. The configuration of case I allows us to investigate the behaviour of the dynamical system for different tropopause temperatures (Figs. 3.8, 3.9). The TC intensity increases with increasing difference between SST and tropopause temperature by lowering T_t (Fig. 3.8), and the amplitude as well as the formation threshold are shifted to lower SSTs (Fig. 3.9).

Figure 3.8: Bifurcation diagram of maximum tangential wind v_{b2} (m/s) in case I as a function of T_s (°C) for different fix tropopause temperatures T_t and $h_a = 45\%$. Stable equilibria are coloured in dark grey and unstable equilibria in a brighter grey.

The equilibrium surfaces of maximum tangential wind and the regime diagram for case N2 are shown in Fig. 3.10a and 3.11a, respectively. We see that non-trivial solutions appear for much lower SSTs, even below the freezing point, than in the other cases. For example, a maximum wind speed of about 33 m/s results at $T_s = 18°C$ and $h_a = 80\%$. Under these conditions, tropical cyclones do not occur in the real atmosphere. Therefore, we think that the assumption of convective neutrality cannot be applied in general. Looking at the regime diagram (Fig. 3.11a), we see that the equilibria exhibit a cusp bifurcation at $T_s \approx 10°C$ and $h_a \approx 50\%$. Beside its different position, the C regime is also oriented in a different way compared to cases I and N1. Furthermore, the lower stable equilibrium becomes unstable at high SSTs and low relative humidity, where the B1 regime again switches to the A regime. A notable qualitative difference in comparison to case I and N1 is that the B2-regime narrows with increasing SST, i.e. the obstruction for tropical cyclogenesis becomes larger with increasing SST in case N2. On the other hand, the steady state tropical cyclone intensifies at
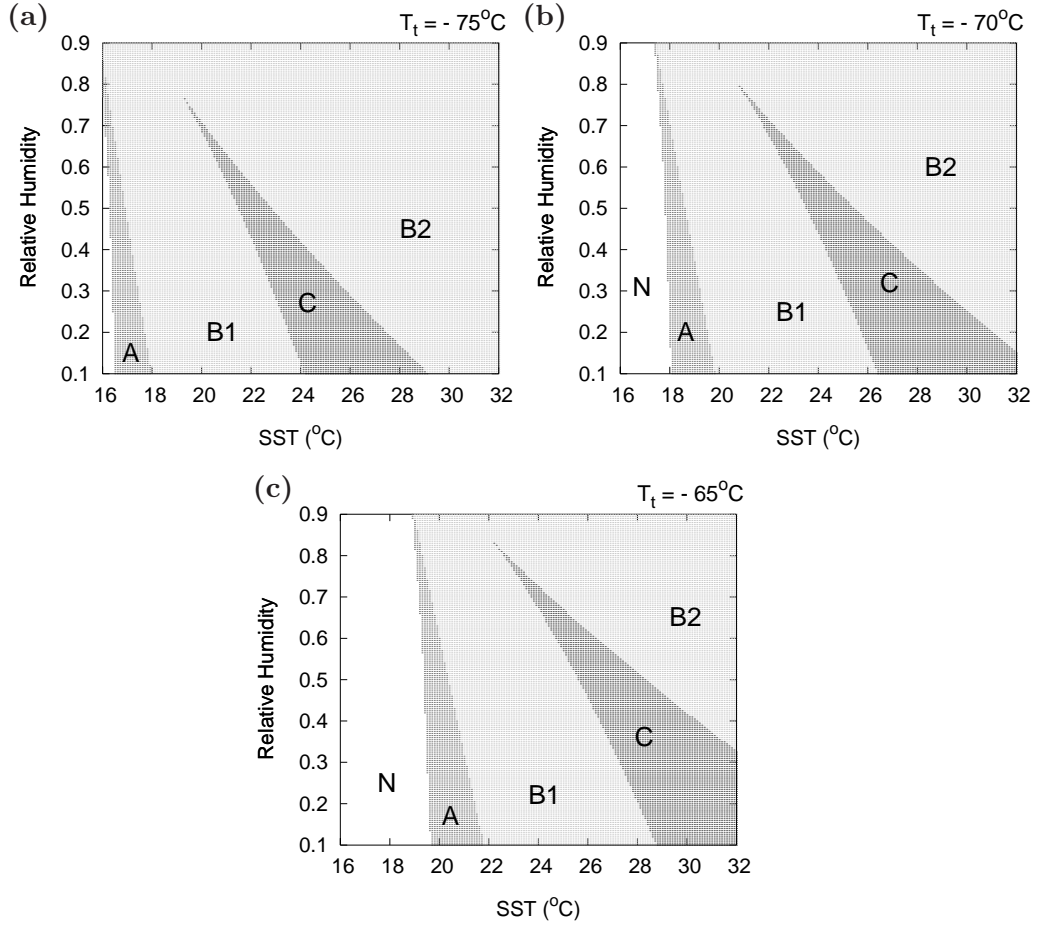
Figure 3.9: Regime diagrams in case I as a function of T_s (°C) and h_a (fraction by one) for different tropopause temperatures: (a) $T_t = -75$°C, (b) $T_t = -70$°C and (c) $T_t = -65$°C. The different regimes are labelled like in Fig. 3.4.

higher SSTs. In Case N2 the N-regime arises only below a sea surface temperature of about -10°C, where the validity of the model is rather questionable.

The results for the hybrid case H are displayed in Fig. 3.10b and 3.11b. In this case, we have a clear SST formation threshold since in the regions with moist static stability it coincides with case I, except for some small differences due to the different value for τ_C. Therefore, the A-regime occurs at both edges in the SST range shown in the regime diagram in case H. For larger SSTs, however, the regimes are (by definition) assembled identically to case N2 and quite differently from case I. So, a comparison to case H indicates that TC intensity in case I is sensitive to environmental CAPE. This is probably a consequence of the fact that the temperature T_a cannot change in time due to convective exchange. Possibly, case I would be more similar to the hybrid case if a dynamical adjustment of T_a were allowed. Such an adjustment might be realisable by implementation of a prognostic entropy equation
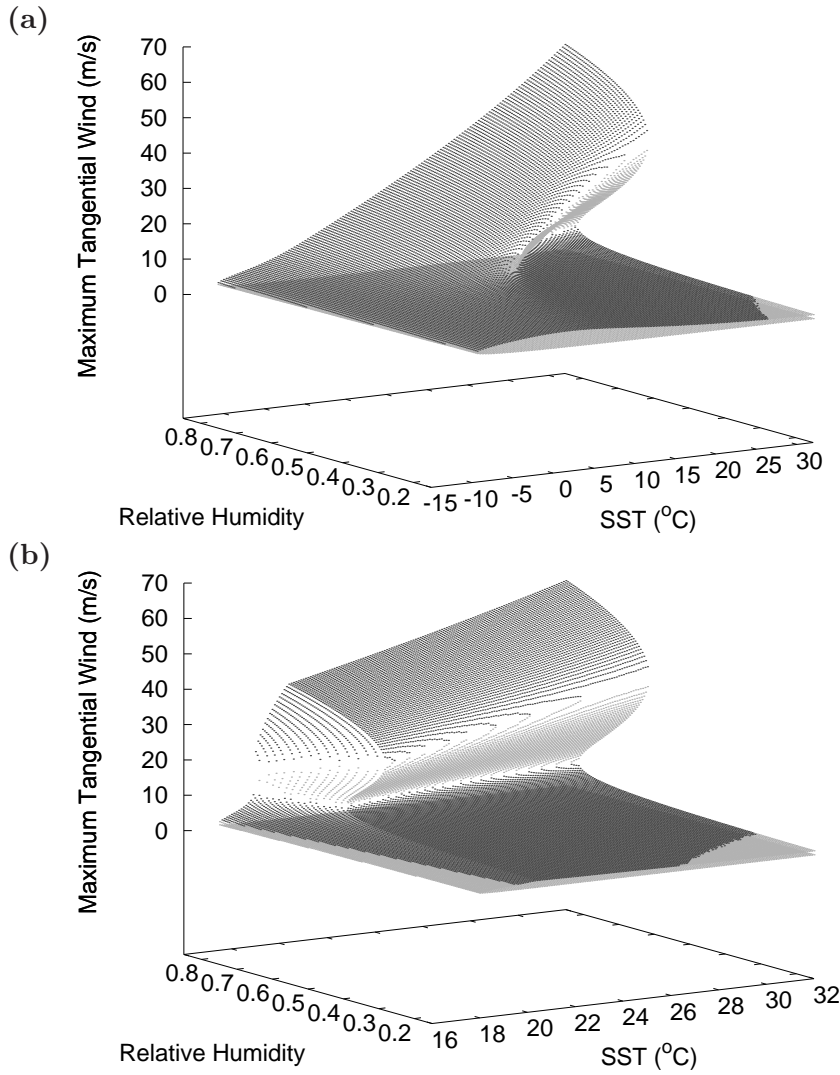
Figure 3.10: Equilibrium solutions for maximum tangential wind v_{b2} (m/s) as a function of T_s (°C) and h_a (fraction by one) with $\tau_C = 8$ h for (a) the neutral case N2 and (b) the hybrid case H. Stable equilibria are coloured in dark grey and unstable equilibria in a brighter grey. Note that the SST-interval chosen in (a) to display case N2 extends into the unphysical range of temperatures below the freezing point.

for the ambient region. However, this is beyond the scope of this study.

The course of the border between the C- and the B2-regime in Fig. 3.11b indicates that tropical cyclogenesis becomes less likely with increasing SSTs (above ∼ 20°C) in the hybrid case H. This may seem to be surprising but is in qualitative agreement with recent climate change simulations which show a tendency towards increasing intensity and a decreasing frequency of occurrence of tropical cyclones in response to global warming [e.g. Bengtsson et al. (2007)]. An explanation for the increasing obstruction seems to be related to the secondary circulation, which intensifies with increasing entropy difference between the atmosphere and
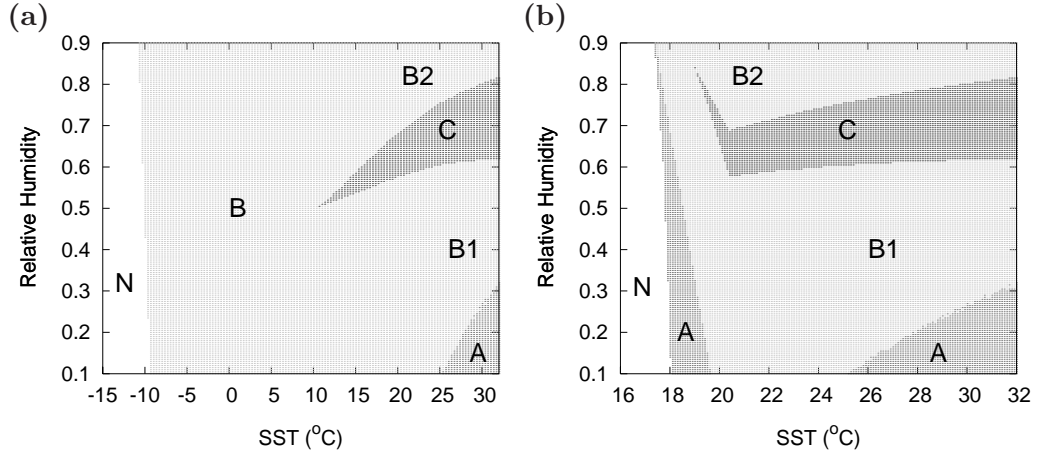
Figure 3.11: Regime diagrams as a function of T_s (°C) and h_a (fraction by one) with $\tau_C = 8$ h for (a) the neutral case N2 and (b) the hybrid case H. The different regimes are labelled like in Fig. 3.4.

the ocean. This enhances the injection of low-entropy air into the eyewall region and inhibits more efficiently the development of a tropical cyclone.

Entrainment of low-entropy air by shallow convection in the ambient region, in addition to that by the secondary circulation, also has a highly impeding impact on TC formation in case H (Fig. 3.12). When we choose the same time scale for convective damping as depicted in Fig. 3.7a for case I (τ_C = six hours), the B2-regime exists only for relative humidity in the ambient region approximately equal to or even higher than that in the boundary layer beneath (Fig. 3.12c). Even if we take less than half the strength in convective damping as in case I, by setting τ_C to ten hours (Fig. 3.12a), a development of a tropical cyclone from a small initial disturbance close to the state at rest, still becomes only possible for relative humidity in the ambient region higher than ca. 63%, which is still about 18% higher, than the standard value we have chosen with regard to observational data at the 500 hPa-level (Jordan, 1958). In order to further abate the amplitude threshold with respect to h_a in case H, the entrainment of low-entropy air by convection within the ambient region must be further reduced by an increase in τ_C. For higher values in τ_C, the tendency of TCs to become less likely with increasing SST is more pronounced (Fig. 3.12). On the other hand, in case I (see above) we found that TCs generally become more likely with both higher values in h_a and increased SSTs (Figs. 4a, 5a), and the influence of h_a on the amplitude threshold gets smaller with decreased convective damping in the ambient region (Figs. 3.6, 3.7).
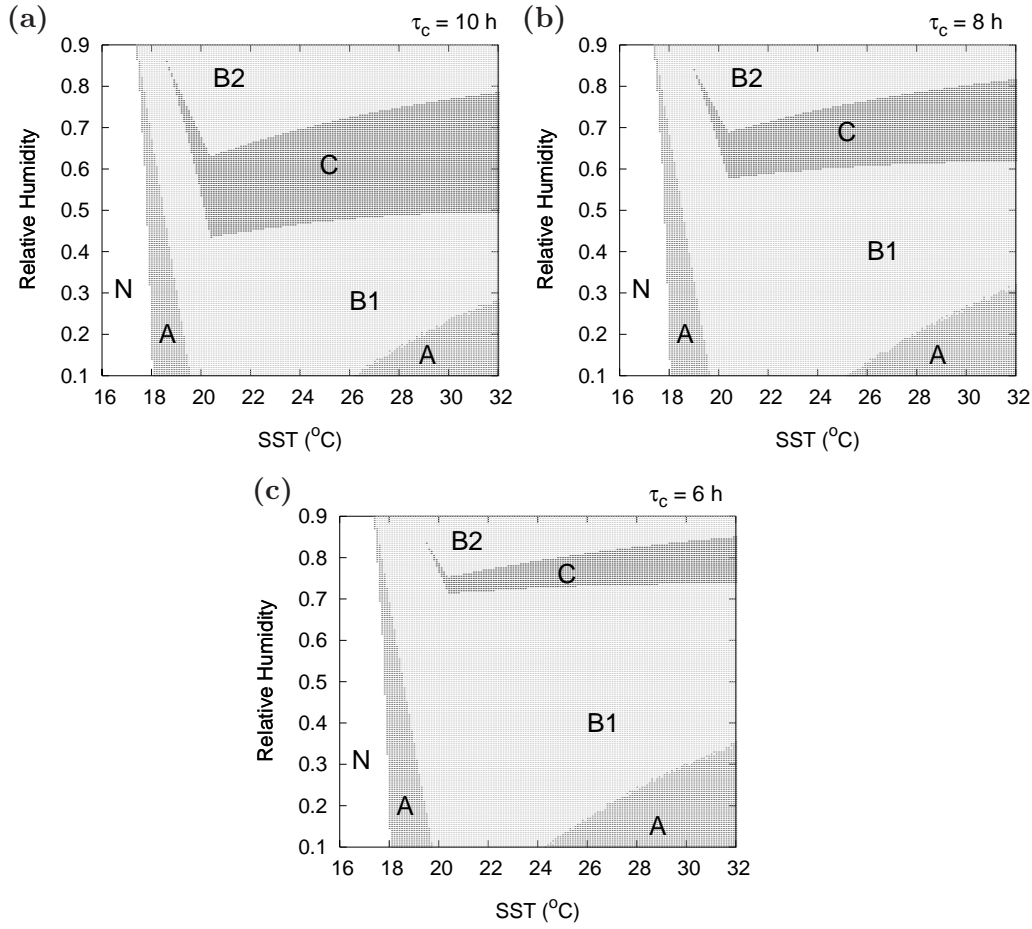
Figure 3.12: Regime diagrams in case H as a function of T_s (°C) and h_a (fraction by one) for different time scales in convective damping: (a) $\tau_C = 10$ h, (b) $\tau_C = 8$ h and (c) $\tau_C = 6$ h. The different regimes are labelled like in Fig. 3.4.

3.5   Cyclogenesis

3.5.1   Initial growth

To analyse the behaviour in the early phase of storm development, cyclogenesis in the box-model is considered in a highly idealised way. In a state near to an atmosphere at rest, the eyewall region plays the role of a convective ring that eventually contracts and forms the eyewall of the fully developed tropical cyclone. Such a cyclogenesis scenario is possible in an axisymmetric tropical cyclone model. Regarding the growth of the TC, CISK [conditional instability of the second kind, (Charney and Eliassen, 1964)] and WISHE [wind induced surface heat exchange, (Emanuel, 1986)] mechanisms may become crucial. The importance of these processes can be analysed in the box-model by consideration of small amplitudes and

neglecting obstructive processes, i.e. $\delta = 1/\tau_E = 1/\tau_C = 0$. Linearisation and combination of Eqs. (3.16), (3.18) and (3.19) with respect to the state at rest gives

$$v_b = \frac{\Gamma H}{2f\Delta R} s_i^* \; .$$
(3.54)

Using this approximation for v_{b2} and $\zeta \approx f$ in Eq. (3.9), we obtain for the mass stream function

$$\Psi_{b2} = C_D \pi \rho_b R_2 \frac{\Gamma^2 H^2}{2f^3 \Delta R^2} s_i^{*2} \; .$$
(3.55)

The entropies at the sea surface and the mass M_{bi} are assumed to be constant. With these relations the dynamical system becomes

$$\frac{ds_i^*}{dt} = \frac{F_C}{M_i} s_i^{*2} (s_{bi} - s_i^*),$$
(3.56)

$$\frac{ds_{bi}}{dt} = \frac{F_C}{M_{bi}} s_i^{*2} (s_{ba} - s_{bi}) + F_{Wi} s_i^* (s_{oi} - s_{bi}),$$
(3.57)

$$\frac{ds_{ba}}{dt} = -\frac{F_C}{M_{ba}} s_i^{*2} s_{ba} + F_{Wa} s_i^* (s_{oa} - s_{ba}).$$
(3.58)

where

$$F_C = C_D \pi \rho_b R_2 \frac{\Gamma^2 H^2}{2f^3 \Delta R^2} \; , \quad F_{Wa} = C_H \frac{\Gamma H}{4f\Delta R H_b} \; ,$$

$$F_{Wi} = C_H \left[1 + \left(\frac{R_1}{R_2} \right)^{\kappa-1} \right] \frac{\Gamma H}{4f\Delta R H_b} \; ,$$

The atmosphere at rest (with $s_i^* = 0 \; \mathrm{Jkg^{-1}K^{-1}}$) forms a steady state solution of the system. For this state, s_{bi} and s_{ba} can take arbitrary values, since exchange with the sea surface vanishes. A stability analysis by linearisation of the system (3.56)-(3.58) reveals that the state at rest is dynamically indifferent. However, small perturbations may grow and eventually form a tropical cyclone. This can be seen by solving Eq. (3.56) for a prescribed boundary layer entropy s_{bi} which is positive and nonzero when the atmosphere is unstable to convection. Then, ignoring the third order term on the right hand side leads to the following solution

$$s_i^* = \frac{s_{i0}^*}{1 - \frac{F_C}{M_i} s_{bi} t s_{i0}^*} \; ,$$
(3.59)

which describes an intensification of the vortex with increasing growth rate from a small initial perturbation s_{i0}^*. This corresponds to cyclogenesis by the CISK mechanism, where the frictionally induced boundary layer inflow is responsible for latent heat release in the eyewall and thereby enhances the tangential wind. This in turn, strengthens the inflow and, thereby, closes the feedback loop. We see that the intensification rate is proportional to the drag
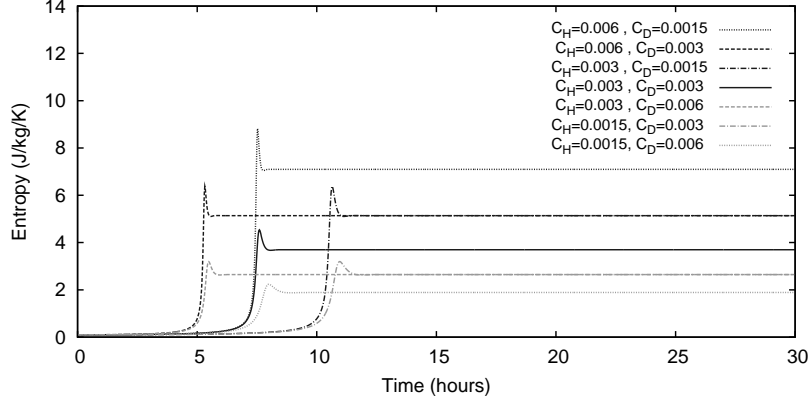
Figure 3.13: Time evolution of eyewall entropy s_i^* ($\mathrm{Jkg^{-1}K^{-1}}$) for various transfer coefficients C_H and C_D. The curves display time integrations of the dynamical system (3.56)-(3.58), which is valid at small amplitudes.

coefficient C_D. The growth stops when the eyewall saturated moist entropy attains the value of the boundary layer.

For excitation of a pure WISHE feedback, the atmosphere must be neutrally stratified, i.e. $s_i^* = s_{bi}$. Convection is implicitly assumed to remove any convective instability immediately. Equating s_i^* with s_{bi} and linearisation of Eq. (3.57) gives:

$$\frac{ds_{bi}}{dt} = F_{Wi} s_{oi} s_{bi}, \tag{3.60}$$

The solution of this equation describes a perturbation intensifying with a growth rate $\sigma = F_{Wi} s_{oi}$ proportional to C_H.

We see that both CISK and WISHE feedbacks may be excited in the box-model. Indeed, in the model these feedbacks act in a combined way. Combining the CISK and WISHE term by substitution of Eq. (3.60) into the time derivative of Eq. (3.56), neglecting third order terms, we obtain the following differential equation

$$\frac{d}{dt}\left(\frac{1}{s_i^{*\,2}}\frac{ds_i^*}{dt}\right) = \frac{F_C F_{Wi}}{M_i} s_{oi} s_i^*, \tag{3.61}$$

This equation shows that the intensification rate is proportional to $\sqrt{C_H C_D}$. The relevance of the combination of CISK and WISHE intensification mechanisms can be tested by variation of C_H and C_D as has been suggested by Craig and Gray (1996). Therefore, we performed various cyclogenesis simulations with the simplified dynamical system (3.56)-(3.58). All necessary model parameters are given in Table 3.1. Fig. 3.13 displays time evolution of entropy s_i^* for various values of C_H and C_D. We clearly see that the overall growth rate is indeed a function of $\sqrt{C_H C_D}$ while the final intensity depends on C_H/C_D.

3.5.2   Transient dynamics of amplification and equilibration

The stability properties of the different equilibria are also reflected in the time development when we consider cyclogenesis including all effects prescribed by the thermodynamic budget equations (3.40)-(3.42) given in subsection 3.2.6. For this purpose, the time integration is started close to or from initial conditions corresponding to the unstable equilibria (Fig. 3.14). Model experiments initialised by negative (positive) s_i^*-perturbations, inducing a negative (positive) deviation in velocity with respect to a system repellor, run into the respective lower (higher) stable equilibrium. As initialised with a negative perturbation with respect to
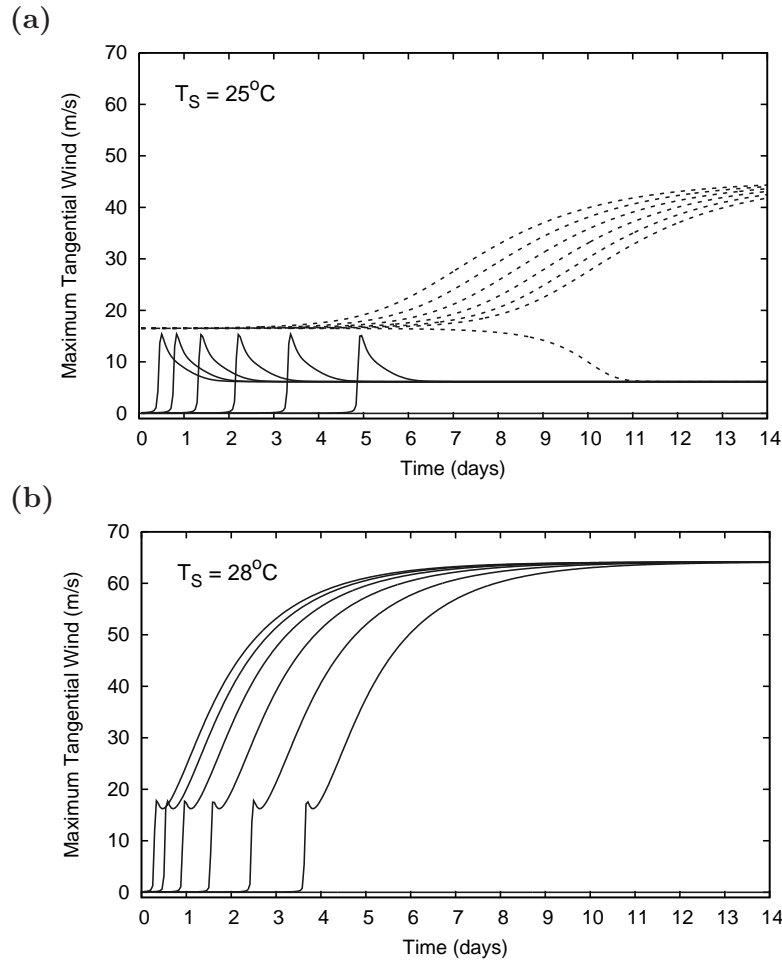
(a)

(b)

Figure 3.14: Time development of maximum tangential wind v_{b2} (m/s) in case I with $h_a = 45\%$ started near an unstable equilibrium for (a) $T_s = 25°C$ and (b) $T_s = 28°C$. Equilibrium solutions in the upper panel (a) are located in the C-regime (see Figs. 3.3b, 3.4b). Model runs initialised by small perturbations with respect to the upper repellor are plotted with dashed lines and those started near the lower equilibrium are plotted with solid lines. In the lower panel (b) equilibrium solutions exist in the B2-regime with only one repellor. For each repellor, model runs were initialised by one negative perturbation and six gradually increased positive perturbations.

the lowest unstable equilibrium, the system simply runs into the state of an atmosphere at rest. The smallest positive eyewall entropy perturbation introduced to the time experiments plotted in Fig. 3.14 is $\Delta s_i^* = 10^{-4}$ Jkg^{-1}K^{-1} and is gradually doubled. The higher the magnitude of the initial perturbation, the faster does the system reach a stable state. At the beginning, the maximum tangential wind speed hardly increases for several days and it takes much longer than for higher perturbations until it intensifies with a relatively high rate. However, the maximum intensification rate is not visibly affected by the magnitude of the initial perturbation.

Concerning TC-genesis from very small initial perturbations (cf. Fig. 3.14b), our result is in qualitative agreement with that found earlier in a three-layer axisymmetric TC model by Anthes [cf. Anthes (1982)]. As can be seen in Fig. 3.14b, the cyclone intensifies rapidly in the initial phase until it reaches a first maximum. Then it slightly decays and further intensifies at a smaller rate than in the beginning. To some extent, this behaviour can be attributed to the action of the lower attractor, which acts into the opposite direction of the upper attractor after the initial growth. The further we move away from the C regime into the B2 regime (in $T_s - h_a$ space), the weaker is the impeding effect of the lower attractor on TC formation and the higher is the intensification rate as the system develops from a weak storm into a tropical cyclone.

3.6   Discussion

The dynamical system analysis of tropical cyclones in a conceptual box-model reveals the existence of a SST threshold for the formation of cyclones under different conditions. We find that no cyclone would form below a certain SST. If neutrality to convection is maintained by moisture adjustment in the boundary layer (case N1), the SST formation threshold does not differ from that found in the case in which moist static instability was not excluded (case I).

The results of the neutral case N1 and the case, which allows for both moist-neutral stability, and CAPE outside the eyewall (case I), are in good qualitative and quantitative agreement with regard to PI, TC intensification, and their sensitivity to the other model parameters investigated in this study. The type of neutralisation we obtain in case N1 corresponds to the neutralisation mechanism found from a correlation analysis of tropical soundings in regions with trends to enhanced moist-neutral stability (DeMott and Randall, 2004). But in the box-model, moisture adjustment (case N1) to maintain neutrality under decreased dry static stability results in unrealistically low values for boundary layer relative humidity over a warm tropical ocean. Quantitatively, this may possibly be due to the fact

that we cannot look at the dynamically combined effect in the box-model (i.e. we consider either a moisture or a lapse rate adjustment).

On the other hand, when neutrality is kept by temperature adjustment in the ambient region as in case N2, the formation threshold would be shifted to SSTs below the freezing point and storms of TC intensity, already form over greatly colder water than in reality. This is also a result of E-PI theory excluding moist static stability of the atmosphere and premising a neutral ambient atmosphere instead. Observational studies give evidence for the existence of non-zero CAPE in the catchment area of a TC. Hurricane soundings computed from radiosonde measurements (Sheets, 1969) and measurements from dropwindsondes (Bogner et al., 2000) point to the existence of considerable amounts of CAPE with increased radial distance from the centre of a mature tropical cyclone. Analyses of satellite and radiosonde observations over areas with deep convection in the tropical Pacific exhibit the existence of CAPE for SSTs higher than 28°C and moist-neutral stability for SSTs below 27°C (Fu et al., 1994). Therefore, we also considered a hybrid case which allows for stability but prohibits instability by temperature adjustment (case H). Neutrality is probably a suitable assumption for regions characterised by strong convection, because it contributes to the adjustment of the atmosphere towards a neutral state and in reverse, a reduced static stability facilitates convection.

The stability of the troposphere is to some extent determined by the temperature lapse rate. DeMott and Randall (2004) found that the correlation between temperature lapse rate, moisture content and CAPE depends on the sign of the trend in CAPE. Their results indicate that a decrease in CAPE is primarily driven by changes in the lapse rate, whereas increases in CAPE are chiefly driven by increasing moisture contents. Results from global climate models show, that the lapse rate feedback in global warming scenarios, with enhanced mean SST, has a stabilising effect in the tropics by heating the upper troposphere at the expense of the surface [e.g. Hansen et al. (1984); Hegerl et al. (2007)]. This view is in accordance with the observed nonlocality of tropical cyclones (Swanson, 2008). In this context, nonlocality means that tropical cyclone activity depends on the relation between local SST anomalies and tropical mean SST rather than only on local SST anomalies. With regard to the box-model, this suggests that the tropopause temperature is mainly a function of tropical mean SST and that SST anomalies cause variations in static stability also crucial for tropical cyclone activity. In the box-model, this effect can be seen in both case N1, where decreased dry static stability is accompanied by a decrease in relative boundary layer humidity to maintain moist neutrality, and in the non-neutral case I, where boundary layer humidity is held fix. Presuming that changes in tropopause temperature are mainly controlled by changes in mean SST rather than local SST anomalies infers that the amplitude threshold of ~ 26°C for TC

development observed under present climate conditions is shifted under climate change, as indicated by Holland (1997) and Henderson-Sellers et al. (1998).

Both the hybrid case H and case I with no adjustment, display five different regimes with respect to the number of equilibrium states and their stability properties for different values in SST and relative humidity in the ambient region. By definition, case H and I are identical with regard to the formation threshold. Within a certain range in SST and h_a, we detect an additional repellor forming an amplitude threshold for the development of a TC. The amplitude threshold is sensitive to sea surface temperature and entrainment of low-entropy air into the boundary layer. In case we allow for CAPE in the ambient region, the SST plays a more dominant role in setting the amplitude threshold than entrainment along the secondary circulation. Here, our model results imply that the frequency of occurrence of TCs rises with decreased entrainment of low-entropy air and locally increased SST.

In the hybrid case, the entrainment effect has a high impact on the amplitude threshold. TCs can only develop from small initial disturbances, when relative humidity in the ambient region is sufficiently high and convective damping within the ambient air is sufficiently low. In case H, TCs also become more intense but occur less frequently with increased SSTs when CAPE is zero. Here, neutrality is maintained by temperature adjustment resulting in a decreased vertical temperature gradient from the surface to mid-tropospheric levels at higher SSTs. Otherwise, instability to convection would rise over a warmer ocean as it does in case I. Because of this temperature adjustment, it was not possible here, to probe the effect of a reduced or increased tropical tropopause temperature in response to global warming or cooling, combined with that of a regionally enhanced temperature gradient in the low to mid-tropospheric levels in response to a local increase in SST. Hence, in contrast to case I, we cannot discern the impact of local SST anomalies and nonlocal changes in SST in case H. Presumably, this is the major reason for the different results, we obtain in case I and H. This could be further investigated by testing the system behaviour for a dynamical temperature adjustment in case I. In the frame of the conceptual model, this may be feasible by implementation of an additional thermodynamic budget equation for the entropy in the ambient region, and may provide some material for future investigations.

4   Dynamical system properties and parameter sensitivity of the axisymmetric cloud model HURMOD

4.1   Introduction

In this chapter, the sensitivity of the potential intensity of tropical cyclones towards several thermodynamic control parameters is studied within the axisymmetric convection-resolving model HURMOD (Frisius and Wacker, 2007; Frisius and Hasselbeck, 2009). The environmental sensitivity parameters investigated herein comprise the sea surface temperature, which forms a lower boundary condition in the atmospheric model; the tropospheric temperature stratification; and the environmental moisture content in terms of the initial relative humidity value. Moreover, the dynamical system properties of HURMOD with regard to the respective parameters are investigated empirically on the grounds of numerical long-term simulations, in which a steady state is approached. The results indicate the existence of a Hopf bifurcation, when sea surface temperature is used as the bifurcation parameter.

As has been demonstrated in the previous chapter, the idealised treatment of a tropical cyclone as an autonomous dynamical system, provides a useful ansatz for the description of this phenomenon by a conceptual model. Its results show a strong quantitative and qualitative sensitivity of equilibrium intensity to thermodynamic environmental control parameters, including the sea surface temperature, the vertical temperature stratification, and the relative humidity of the ambient troposphere. On one hand, the simplicity of the conceptual model allows for an exact determination of its equilibrium structure, which is clearly advantageous. On the other hand, the conceptual model relies on a number of relatively rough assumptions and simplifications, while several processes that may be also relevant to the dynamics of TCs cannot be captured within a rather simplistic model of that kind. In order to be able to further specify and incorporate physical processes on smaller scales, a rather complex convection-resolving model is required. For this reason, investigation of the sensitivity of potential intensity of TCs and the bifurcation structure will be also performed with the high-resolution axisymmetric convective model HURMOD, and the results will be compared to those gained from the conceptual box-model. For this purpose, the sensitivity parameters are chosen in analogy to those investigated in the low-order model.

In spite of the fact that real tropical cyclones exhibit several asymmetric features, which cannot be resolved within an axisymmetric framework, we share the view that axisymmetric models provide the basis for theoretical and numerical studies on a theoretical upper limit to TC intensity (Rotunno and Bryan, 2012). It has been shown that the enforcement of an asymmetric structure, due to vertical shear of the large-scale environmental flow, as well as a high translational speed of the storm, acts to lower TC intensity (Zeng et al., 2007, 2008).

This supports the view that axisymmetric models are suitable for the study on a theoretical upper limit to TC intensity. Moreover, axisymmetric models are considerably lower in their computational costs than 3-D models.

This chapter is organised as follows: A brief introduction to the cloud model HURMOD and the parameterisation of sub-scale processes applied in this study is provided in section 4.2. Section 4.3 gives an overview over the model experiments, and modelling assumptions and approximations that are made in the framework of the long-term simulations with HURMOD. In section 4.4, the parameter sensitivity and the dynamical system behaviour of the convective model HURMOD are investigated and discussed. A discussion on the results from HURMOD in comparison to the results from the low-order model is provided in section 4.5.

4.2   Model description

For our numerical experiments, we use the cloud-resolving atmospheric model HURMOD, which is designed to capture convective motion in detail. HURMOD is formulated in cylindrical coordinates (r, φ, z) on the basis of the approximation of an axisymmetric vortex flow, which is suitable to simulate the inner dynamics of TCs. The spatial dependence of the Coriolis acceleration is neglected, and a constant value corresponding to that at a latitude of 20° is taken for the whole model domain. Similar models have been developed and introduced in several previous studies [e.g. Willoughby et al. (1984), Rotunno and Emanuel (1987), Bryan and Fritsch (2002), Tang and Emanuel (2012b)]. All quantities are computed on a staggered Arakawa-C-type grid as in Rotunno and Emanuel (1987). The cylindrical model domain has a vertical extent of 20 km and a radius of 2000 km. The vertical grid spacing is $\Delta z = 250$ m, and the radial grid spacing in the centre within a radius of 120 km is $\Delta r = 500$ m, rising non-linearly with radial distance to the centre to $\Delta r \simeq 10$ km in the outermost ring of the model domain. For time integration, we employ a leap-frog scheme. An extensive description of the model is given in Frisius and Wacker (2007). A brief description of the model and the parameterisation used in this study, will be given in the following subsections. Further approximations and the initial conditions are outlined in section 4.3.

4.2.1   Prognostic equations

The governing equations are phrased in flux form. In comparison to the advective form, the flux form is more suitable to avoid non-physical sources and sinks, and therefore improves the computation of conserved properties. The prognostic variables in the equations of motion are radial, tangential, and vertical momentum density (ρu, ρv and ρw). The momentum equations are given by:

$$\frac{\partial(\rho u)}{\partial t} = -\frac{1}{r}\frac{\partial(r\rho u^2)}{\partial r} - \frac{\partial(\rho u w)}{\partial z} + \rho\left(\frac{v^2}{r} + fv\right) - \rho c_{pd}\theta_v\frac{\partial\Pi^*}{\partial r} + D_{\rho u} \tag{4.1}$$

$$\frac{\partial(\rho v)}{\partial t} = -\frac{1}{r}\frac{\partial(r\rho v u)}{\partial r} - \frac{\partial(\rho v w)}{\partial z} - \rho\left(\frac{vu}{r} + fu\right) + D_{\rho v} \tag{4.2}$$

$$\frac{\partial(\rho w)}{\partial t} = -\frac{1}{r}\frac{\partial(r\rho w u)}{\partial r} - \frac{\partial(\rho w^2)}{\partial z} - \rho c_{pd}\theta_v\frac{\partial\Pi^*}{\partial z} \tag{4.3}$$
$$+ \rho g\left(\frac{\theta^*}{\theta_0} + \frac{\theta}{\theta_{v0}}\left[\left(\frac{R_v}{R_d} - 1\right)q_v{}^* - q_c - q_r\right]\right) + D_{\rho w},$$

where the potential temperature θ, the mass fraction of water vapour q_v, and the non-dimensional pressure Π (also referred to as the Exner function) can be split into their horizontally independent reference value, denoted by the index 0, and the deviation from the respective reference state, denoted by an asterisk. The continuity equation is given by:

$$\frac{\partial\rho}{\partial t} = -\frac{1}{r}\frac{\partial(r\rho u)}{\partial r} - \frac{\partial(\rho w)}{\partial z}, \tag{4.4}$$

the temperature equation is formulated in terms of the potential temperature flux:

$$\frac{\partial(\rho\theta)}{\partial t} = -\frac{1}{r}\frac{\partial(r\rho\theta u)}{\partial r} - \frac{\partial(\rho\theta w)}{\partial z} + \rho\frac{Q_R + \phi}{c_p\Pi} \tag{4.5}$$
$$-\frac{1}{c_p\Pi}\left(l_v Q_v + [c_{pd}J_d + c_{pv}J_v + c_{pl}(J_c + J_r)]\frac{\partial T}{\partial z}\right) + D_{\rho\theta},$$

and the budget equations for water vapour (index v), cloud water (index c) and rain water (index r) are given by:

$$\frac{\partial(\rho q_v)}{\partial t} = -\frac{1}{r}\frac{\partial(r\rho q_v u)}{\partial r} - \frac{\partial(\rho q_v w)}{\partial z} + Q_v - \frac{\partial J_v}{\partial z} + D_{\rho q_v} \tag{4.6}$$

$$\frac{\partial(\rho q_c)}{\partial t} = -\frac{1}{r}\frac{\partial(r\rho q_c u)}{\partial r} - \frac{\partial(\rho q_c w)}{\partial z} + Q_c - \frac{\partial J_c}{\partial z} + D_{\rho q_c} \tag{4.7}$$

$$\frac{\partial(\rho q_r)}{\partial t} = -\frac{1}{r}\frac{\partial(r\rho q_r u)}{\partial r} - \frac{\partial(\rho q_r w)}{\partial z} + Q_r - \frac{\partial J_r}{\partial z} + D_{\rho q_r}. \tag{4.8}$$

The first and second terms on the rhs of the prognostic equations (4.1)-(4.8) represent the advection of the respective variable. In the computation of the horizontal momentum fluxes

(4.1)-(4.2), Coriolis and centrifugal forces are accounted for by the third term on the rhs. The effect of the radial and vertical pressure gradient is represented by the fourth term on the rhs of Eq. (4.1), and the third term on the rhs of Eq. (4.3), respectively. The effect of buoyancy is given by the fourth term in the vertical momentum equation (4.3). In all the equations above, the exchange through micro-turbulent mixing of the respective variable G is denoted by $D_{\rho G}$. In the temperature equation (4.5), heat fluxes via radiative cooling and dissipative heating via turbulent eddies are described by the third term, and latent heat as well as vertical diffusive mass fluxes (J_G) are represented by the fourth term on the rhs. In Eqs. (4.6)-(4.8), Q_v, Q_c, and Q_r denote sources and sinks for the respective substance related to transition processes (i.e. condensation, evaporation, autoconversion, coalescence), and vertical diffusive fluxes are represented by the fourth term on the rhs.[22] An overview over the model variables and constants in the governing equations is provided in Table 4.1.

4.2.2 Parameterisation of sub-scale processes

The parameterisation of turbulent mixing by small-scale eddies follows the commonly used simple K-ansatz, where turbulent fluxes are described in analogy to molecular diffusion, and are assumed to be proportional to a parameterised eddy-diffusivity K. The eddy-coefficient K is assumed to be equal for turbulent exchange of momentum and entropy (i.e. eddy-viscosity is considered to equal eddy-diffusivity), but we distinguish between vertical and horizontal eddy-diffusivity, K_v and K_h respectively. The diagnostic calculation of K_v and K_h follows that by Bryan and Rotunno (2009c) [cf. their Eq. (16) and (17)]. As HURMOD is formulated in flux form in this study, we use dynamic instead of kinematic diffusivity:

$$K_h = l_h^2 \rho \sigma_h, \qquad K_v = l_v^2 \rho (\sigma_v^2 - N^2)^{\frac{1}{2}}, \tag{4.9}$$

where σ_v denotes vertical and σ_h horizontal strain deformation, N is the Brunt-Väisälä or stability frequency, and l_h and l_v represent the horizontal and vertical mixing length scale, respectively. The eddy-diffusivity formulated in Eq. (4.9) is proportional to the squared mixing length scale, which has to be parameterised. In a modelling study, Bryan and Rotunno (2009c) find that TC intensity exhibits a considerable sensitivity to l_h. They suggest a value of $l_h = 1500$ m to be reasonable. Here, we take a lower value of $l_h = 750$ m, which was derived by Zhang and Montgomery (2012) based on in situ aircraft measurements taken in the boundary layer of three major hurricanes.

---

[22]For reasons of simplicity, we only work with "warm-rain" simulations in the present work, i.e. the ice phase is not considered in the calculation of the water budget, and the cloud-microphysical parameterisation follows a Kessler type scheme. For possible effects of the inclusion of an ice phase in axisymmetric models, we may refer the reader to previous studies by Willoughby et al. (1984) as well as Frisius and Hasselbeck (2009).

Table 4.1: Notation for variables and constants in prognostic equations (4.1)-(4.8)

Not.	Value	Meaning
t		Time
r		Radius
z		Height
u		Radial velocity
v		Tangential velocity
w		Vertical velocity
V		Horizontal wind speed
Π		Non-dimensional pressure (Exner-function)
ρ		Air density
T		Absolute temperature
θ		Potential temperature
q_v		Mass fraction of water vapour
q_c		Mass fraction of cloud water
q_r		Mass fraction of rain water
J_G		Vertical diffusive mass flux of substance G
		(G = dry air, water vapour, cloud water, rain water)
Φ		Dissipation rate
Q_R		Radiative heating rate
$D_{\rho G}$		Micro-turbulent flux of quantity G
		($G = u, v, w, \theta, q_v, q_c, q_r$)
c_p		Spec. heat capacity of air at constant pressure
c_{pd}	1005 Jkg^{-1}K^{-1}	Spec. heat capacity of dry air
c_{pv}	1848 Jkg^{-1}K^{-1}	Spec. heat capacity of water vapour
c_{pl}	4185 Jkg^{-1}K^{-1}	Spec. heat capacity of liquid water
R_d	287.0 Jkg^{-1}K^{-1}	Spec. gas constant of dry air
R_v	461.5 Jkg^{-1}K^{-1}	Spec. gas constant of water vapour
l_v	$2.5 \cdot 10^{-6}$ Jkg^{-1}	Latent heat of vapourisation
f	$5 \cdot 10^{-5}$ s^{-1}	Coriolis-parameter
g	9.81 ms^{-2}	Gravitational acceleration

It is also shown by Bryan and Rotunno (2009c) that the shape of the horizontal flow field in and near the eyewall region is strongly influenced by the choice of l_v [cf. their Fig. 5]. In a test study on boundary layer schemes and their turbulence parameterisation Kepert (2012) argues that biases in the lowest model level flow, thermodynamic fields, and consequently in the surface fluxes occur due to an overestimation of eddy-diffusivity at the lowest model level in many Bulk schemes, when the mixing length is treated as a spatially independent constant. As recommended by Kepert (2012), we implement a height-dependent formula to calculate the vertical mixing length l_v, developed fifty years earlier by Blackadar (1962) [cf. his Eq. (24)]:

$$l_v = \frac{kz}{1 + kz/l_{v_\infty}}, \tag{4.10}$$

where k is the von Kármán-constant, and l_{v_∞} is the value of l_v at infinite height. For $l_{v_\infty} = 200$ m and with $k = 0.4$, we obtain $l_v = 100$ m at $z = 500$ m. This agrees with the value derived by Zhang et al. (2011) from aircraft data collected in the eyewall region of one category 4, and one category 5 hurricane on the SSHS.

The computation of micro-turbulent atmosphere-ocean exchange is based on a commonly used bulk algorithm [cf. Eq. (20) in Frisius and Hasselbeck (2009)]. In the study at hand, vertical turbulent surface fluxes are calculated as a function of the horizontal wind speed V_{10m} at $z = 10$ m instead of that at the lowest model level

$$F_{G_0} = C_G V_{10m} \left(G_0 - G \right), \tag{4.11}$$

where G_0 represents the value of water vapour, heat or momentum at $z = 0$ m, and C_G is the surface transfer coefficient of the respective quantity G. Both the radial and tangential component of V_{10m} are approximated by assuming a logarithmic wind profile beneath the lowest model level

$$\mathrm{v}_{10m} = \mathrm{v}_1 \frac{ln\left(z_{10m}/r_L\right)}{ln\left(z_1/r_L\right)}, \tag{4.12}$$

where v_{10m} represents either the radial (u_{10m}) or the tangential wind velocity (v_{10m}) at $z = 10$ m, v_1 the corresponding component of the horizontal wind velocity at the lowest model level above the sea surface, z_1, and r_L the sea surface roughness length. The roughness length r_L is a function of the surface exchange coefficient for momentum C_D and is calculated at $z = 10$ m:

$$r_L = \frac{z_{10m}}{exp\left(\frac{k}{\sqrt{C_D}}\right)}. \tag{4.13}$$

In several previous hurricane modelling studies, both the drag coefficient C_D and the surface exchange coefficient for heat and moisture C_H are chosen to be equal, and are prescribed as a linear function of horizontal wind speed V at a near-surface level according to Deacon's formula [e.g. Rotunno and Emanuel (1987), Frisius and Hasselbeck (2009)]. Instead of using Deacon's formula, the surface exchange coefficients will be determined in close agreement with the results from observation-based studies by Black et al. (2007) and Fairall et al. (2003). For C_H we take a constant value of $1.2 \cdot 10^{-3}$, which is very close to the value found by Black et al. (2007) (cf. their Fig. 6). The drag coefficient is assumed to vary linearly with wind speed within a certain range of V_{10m} [cf. Fig. 5 in Black et al. (2007) and Fig. 10 in Fairall

et al. (2003)]:

$$
C_D = \begin{cases} 1.0 \cdot 10^{-3} \ , & V_{10m} < 5 \ ms^{-1} \\ 1.0 \cdot 10^{-3} + 7 \cdot 10^{-5}(V_{10m} - 5 \ ms^{-1}) \ , & 5 \ ms^{-1} \leq V_{10m} \leq 25 \ ms^{-1} \\ 2.4 \cdot 10^{-3} \ , & V_{10m} > 25 \ ms^{-1} \end{cases} \ , \quad (4.14)
$$

As the drag coefficient C_D by itself is a function of the wind speed V_{10m}, we only iteratively compute proximate solutions to Eqs. (4.12)-(4.14). Notwithstanding, it is probably much more realistic to calculate the turbulent surface exchange [Eq. (4.11)] on the basis of 10 m-wind speeds rather than that at the much higher first model level, which would possibly result in an excessive inflow and, consequently, a stronger eyewall updraught (Kepert, 2010a).

The effect of radiation is parameterised in a most simplistic manner by application of a so-called "Newtonian cooling" (Rotunno and Emanuel, 1987), given by

$$
\frac{Q_R}{c_{pd}\Pi} = -\frac{\theta - \theta_E}{\tau_R}, \quad (4.15)
$$

where τ_R is a time scale for radiative cooling, and θ_E denotes the radiative equilibrium potential temperature (for further notations, see Tab. 4.1). In HURMOD, τ_R is set to 12 h, and θ_E is assumed to be equal to the potential temperature of the reference state θ_0. Therefore, the Newtonian cooling can be viewed as a radiative damping or relaxation of the potential temperature field. Where other processes that affect the temperature, such as advection or turbulent mixing, become negligible, Newtonian cooling is dominant and acts to relax the temperature to its initial vertical profile. Note, in difference to Eq. (4.15) the relaxation is applied to the absolute instead of the potential temperature profile here, which results in a slightly weaker relaxation in the inner low-pressure region.

4.3 Experimental setup

The sensitivity experiments are grouped into two sets: One, which allows for both moist stability and instability, and another one, where the tropospheric stratification is relaxed to moist-neutral conditions. The first setup corresponds to the non-neutral case I considered in the low-order model introduced in chapter 3, and the second set to the moist-neutral case N [23]. To realise case N in HURMOD, the tropospheric equivalent potential reference temperature above the surface layer is kept vertically constant by an iterative adjustment of

---

[23]Note, in the low-order model, moist neutrality is either maintained by an adjustment of the boundary layer relative humidity or by a lapse rate adjustment, whereas a physically more consistent combination of both a moisture- and a temperature profile adjustment, cannot be realised in the low-order model. Therefore, case N is subdivided into case N1 and N2 in the low-order model.

temperature and specific humidity. The tropospheric relative humidity, and specific humidity as well as temperature at the lowest model level are not altered by this procedure.

In case I, the tropopause temperature is taken as a reference parameter, and the lapse rate is adjusted according to the prescribed SST-value, and the respective reference tropopause temperature value. In addition to this, some simulations are carried out in which the temperature lapse rate serves as a reference parameter, and the tropopause temperature is adjusted accordingly. The latter set of model experiments will be referred to as case J. In both case I and J, the vertical reference temperature profile is presumed to be simply linear throughout the troposphere, and hence the initial (or reference) tropospheric lapse rate is equal to the difference between the SST and the reference tropopause temperature, divided by the tropopause height. As long as the far-field is calm so that dynamical processes do not play a role, the temperature profile is fixed in accordance with the initial boundary conditions via radiative forcing. For all three cases, the reference value of the tropopause height, z_t, is set to 15 km. Regarding the initial relative humidity, RH_{ref}, we choose a highly idealised setup, where RH_{ref} is presumed to be distributed homogeneously throughout the troposphere, and to decrease linearly from above the tropopause to zero at the upper vertical boundary of the model domain. The main distinguishing features between these three sets, are listed in Table 4.2.

Table 4.2: Characteristics of different experimental setups in HURMOD

Designation	moist stability	reference stratification
Case I	Non-neutral	Time-invariant tropopause temperature T_t
Case J	Non-neutral	Time-invariant tropospheric lapse rate Γ
Case N	Moist-neutral	

In the standard configuration, the model cyclones are initialised with a sea surface temperature of $T_s = 30°C$; a tropospheric relative humidity of $RH_{ref} = 70\%$; a tropopause temperature of $T_t = -70°C$ in case I, which corresponds to a temperature lapse rate of $\Gamma = 0.00\bar{6}$ K/m, which is also taken as the reference Γ-value in case J; a minimum surface pressure of 1005 hPa in the centre of the model domain; and an environmental reference surface pressure of $p_{00} = 1015$ hPa. Within a radius of twice the initial RMW, the initial disturbance has the shape of a modified Rankine vortex (Holland, 1980). Further outward, the tangential wind at the lowest model level is assumed to decay continuously faster with increasing radius as proposed by George Bryan (personal communication):

$$v(r) = \begin{cases} v_{max}\left(\frac{r}{RMW}\right), & r < RMW \\ v_{max}\left(\frac{r}{RMW}\right)^{-0.3}, & RMW \leq r < 2RMW \\ a_2 v_2 + a_3 v_3, & 2RMW \leq r < r_0 \end{cases} \quad (4.16)$$

with

$$a_2 \equiv 1 - a_3 \; , \qquad\qquad a_3 \equiv \left(\tfrac{r-2RMW}{r_0-2RMW} \right) ,$$
$$v_2 \equiv v_{max} \left(\tfrac{r}{RMW} \right)^{-0.3} , \qquad v_3 \equiv \tfrac{v_{max}}{2} \left(1 - \tfrac{r-2RMW}{r_0-2RMW} \right) , \qquad\qquad (4.16a)$$

where r_0 is the radius of vanishing wind, and the index *init* has been omitted. If not stated otherwise, the initial radius of maximum winds (RMW_{init}) is situated at a distance of 100 km from the centre and the initial radius of vanishing lowest-level winds ($r_{0,init}$) at a radius of 500 km. The vertical distribution of the initial wind field is calculated as follows:

$$v(z) = v(r) \cdot \sqrt{cos(\frac{\pi}{2} \frac{z}{z_t})} \; , \qquad\qquad (4.17)$$

where z_t denotes the tropopause height ($z_t = 15$ km). We presume the initial state to be in gradient wind and hydrostatic balance to relate the initial pressure anomaly to the tangential velocity field as given by Eqs. (4.16)-(4.17). With this and the respective moisture and temperature reference profiles, the initial Π- and θ-anomalies can be determined numerically.

First, the steady state sensitivity to the initial vortex size in the standard configuration is investigated for case I. Then, in both configurations the non-neutral case I and the moist-neutral case N, we run long-term model experiments over a modelling period of 4000 h (i.e. almost seven weeks). The choice of the integration time for the long-term simulations is entirely based on practical considerations. It has been found in numerous model experiments that the system reveals its character after a shorter period of time than 4000 h; i.e. the system either approaches a steady state, which resembles the behaviour of a fixed point attractor corresponding to a stable equilibrium for rather intense model storms, or a lower steady state with small but visible intensity oscillations, or a state of rest. This behaviour will be illustrated and discussed in the subsequent sections of this chapter.

The simulations are carried out with different values for SST and initial tropospheric relative humidity to test the sensitivity of TC intensity and size to SST and atmospheric moisture content. Note, the SST represents a lower boundary condition in HURMOD. Hence the ocean is considered as an unlimited energy reservoir, whereas the air-sea interaction associated with real TCs results in a cooling of surface waters beneath the TC due to enhanced vertical turbulent entropy fluxes into the atmosphere and upwelling (Knaff et al., 2013; Mei and Pasquero, 2013). In case I, we also run simulations with different values for the tropopause temperature to test the sensitivity to vertical temperature stratification and outflow temperature. In a second step, we investigate the cyclone behaviour in response to slow changes in SST for all three cases listed in Table 4.2, and for three differing configurations in case I. These simulations are started from a stable state and are run with a linearly decreasing SST at a rate of

0.001°C/h.[24] The dynamical system behaviour in the standard configuration of case I will
be outlined in further detail in subsection 4.4.3.

For the purpose of long-term model experiments, i.e. to achieve a steady state, the
simulations are run in the hydrostatic mode. This allows us to apply a considerably larger
time-step ($\Delta t = 1$ s - 2 s) compared to that required in the non-hydrostatic configuration
($\Delta t = 0.16$ s - 0.32 s), and thus to reduce computational costs by a factor higher than
six. In order to roughly mimic the effect of moisture exchange through the lateral boundary
without introducing artificial lateral gradients in the moisture field, a global relaxation of the
moisture field is applied in an analog way to the Newtonian cooling. We assume that the
relaxation rate for moisture ($\tau_Q = 120$ h) is by one order of magnitude slower than that for
radiative cooling ($\tau_R = 12$ h). Furthermore, the virtual temperature correction is neglected,
and consequently, the buoyancy term in Eq. (4.3) simplifies to:

$$\rho B = \rho g \frac{\theta^* - \theta\,(q_c + q_r)}{\theta_0}. \tag{4.18}$$

By application of the global moisture relaxation and neglecting the virtual temperature cor-
rection, the long-term development of artificial disturbances at the closed lateral boundary
can be avoided.

To test the possible impact on modelled PI of these two idealisations, three further sim-
ulations are carried out, whose configuration only differs to that of the standard experiment
by either the non-neglect of the virtual temperature correction, or in that no moisture re-
laxation is applied, or both. The evolution of maximum wind speed in comparison to that
of the idealised standard configuration is depicted in Fig. 4.1. As can be seen, all model
experiments reach approximately the same peak intensity after about four days. The onset
of rapid intensification occurs at the earliest in the simulation without any of the two ideal-
isations, and at the latest in the standard simulation with both idealisations. Hence, both
idealisations act to slow down the initial spin-up: Neglecting the virtual temperature correc-
tion directly lowers the buoyancy effect related to saturation in ascending air, and the global
moisture damping introduces a very weak relaxation towards the reference relative humidity,
which is below 100%. After the peak in maximum wind speed is reached, the TC exhibits
the highest weakening rate in the simulation without any of the two idealisations, and the
lowest weakening rate, followed by an approach towards a stable equilibrium in case both
idealisations are applied. The described tendencies are intermediate in the simulations, where
only one of the idealisation is applied. It is further notable that the maximum wind speed
delivered by the model experiment, which incorporates the virtual temperature correction, is

---

[24]The cooling rate is chosen to be very small in order to stay close to the respective equilibrium, which eases
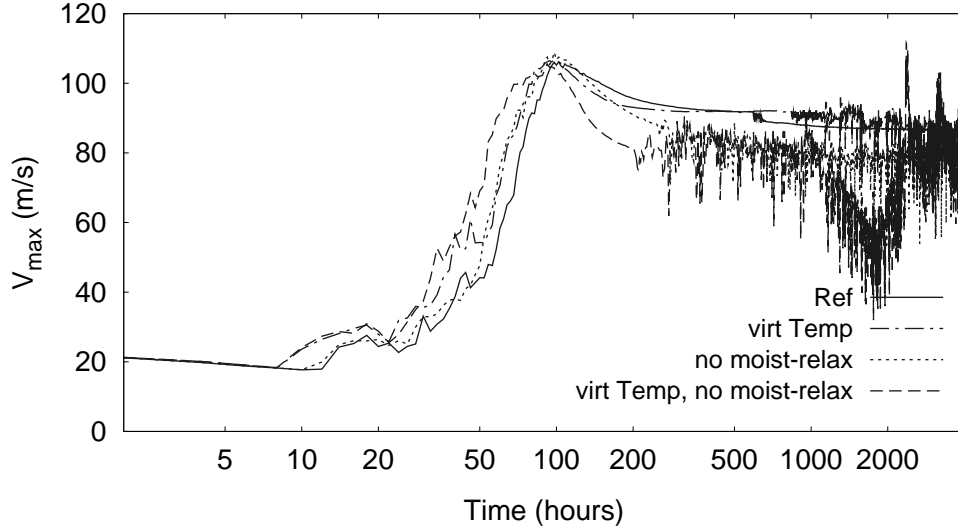the detection of bifurcations.

Figure 4.1: Time development of maximum horizontal wind speed in simulations with the standard case I configuration, which differ with regard to two further idealisations: 1) neglect of virtual temperature correction and assumption of a global moisture relaxation (solid line), 2) assumption of a global moisture relaxation (dashed-dotted line), 3) neglect of virtual temperature correction (dotted line), no further idealisation (dashed line). See text for detailed information. Note, the time scale is logarithmic.

almost equal to that in the idealised standard experiment over a few hundred hours, before the onset of high-amplitude oscillations. These oscillations, which occur in all simulations, except in the standard simulation, are associated with an artificial lateral gradient in relative humidity imposed by the closed domain boundary, which in itself constitutes an idealisation. With regard to these results, the suggested idealisations, i.e. the global moisture damping, and the neglect of the virtual temperature correction, would be certainly inappropriate for a detailed investigation of cyclogenesis and rapid intensification, but are fairly reasonable to study the steady state behaviour of TCs. For this purpose, they provide a useful instrument to suppress the growth of spurious effects associated with the lateral model boundary.

4.4   Results

4.4.1   Initial vortex size

In order to test the sensitivity to a given initial size of the disturbance, we performed long-term simulations with four different initial values of the RMW, and correspondingly four different values in the initial radius of vanishing surface wind speed, $r_{0,init}$ ($RMW_{init} = 50$ km & $r_{0,init} = 250$ km; $RMW_{init} = 100$ km & $r_{0,init} = 500$ km; $RMW_{init} = 150$ km & $r_{0,init} = 750$ km; $RMW_{init} = 200$ km & $r_{0,init} = 1000$ km). The maximum wind speed of the initial vortex, $v_{max,init}$, is chosen to be $\simeq 22$ m/s in this set of experiments. The initial

tangential wind profiles at the lowest model level according to Eq. (4.16) are displayed in Fig. 4.2. Whether cyclogenesis occurs or not, may also depend on the initial vortex strength as will be depicted later on in subsection 4.4.2.
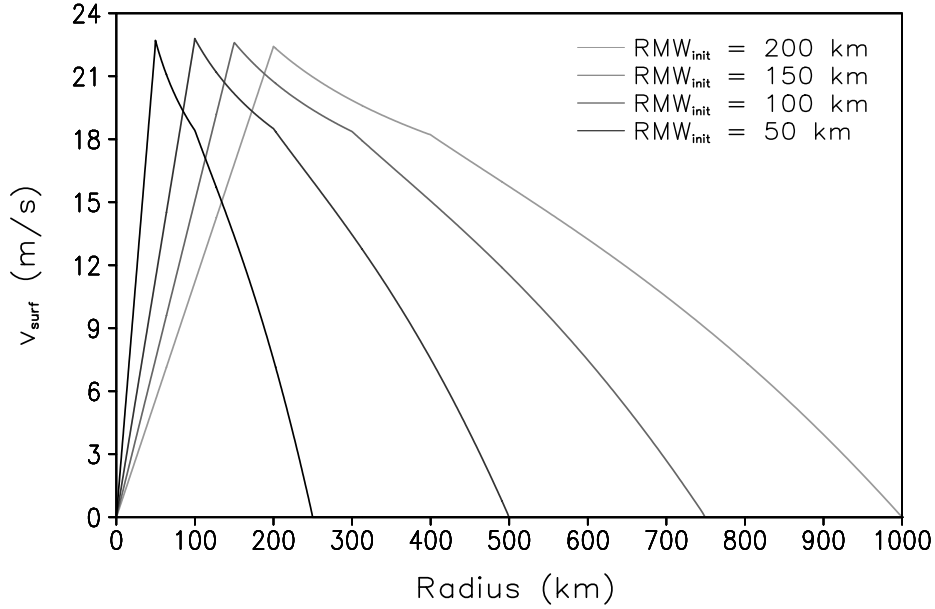

Figure 4.2: Initial tangential surface velocity as a function of radial distance to the centre for four different values in the initial RMW (50 km, 100 km, 150 km, 200 km).

The trajectories in the phase diagram spanned by the RMW and the maximum wind speed (Fig. 4.3) reveal that a tropical cyclone attractor exists in HURMOD. The TC reaches an equilibrium, where both the RMW and maximum horizontal wind speed are independent of the initial perturbation radius as can be seen in Fig. 4.3. For the standard configuration in case I, we obtain an equilibrium at a maximum horizontal wind speed of ~ 87 m/s at a radius of ~ 21 km. At first glance, this result appears to disagree with what was indicated by Rotunno and Emanuel (1987) and confirmed by Xu and Wang (2010). The output from the numerical study by Rotunno and Emanuel (1987) gave evidence suggesting that there is a slight dependence of TC intensity in the mature stage with regard to the initial vortex size, and that the initial size of a TC largely determines its final size. Further evidence for this behaviour is given by Xu and Wang (2010), whose 3-D model simulations also show that cyclones, which stem from an initially larger disturbance, remain larger than those originating from a spatially rather small initial disturbance. However, we note, the larger the initial extent and the further away from its equilibrium position the initial radius of maximum winds is, the longer it takes until the stable equilibrium state is reached. Over a shorter time period of the first ten days, we also observe that storms with an initially larger RMW keep a larger extent than those started from a smaller RMW. In this respect, the results from
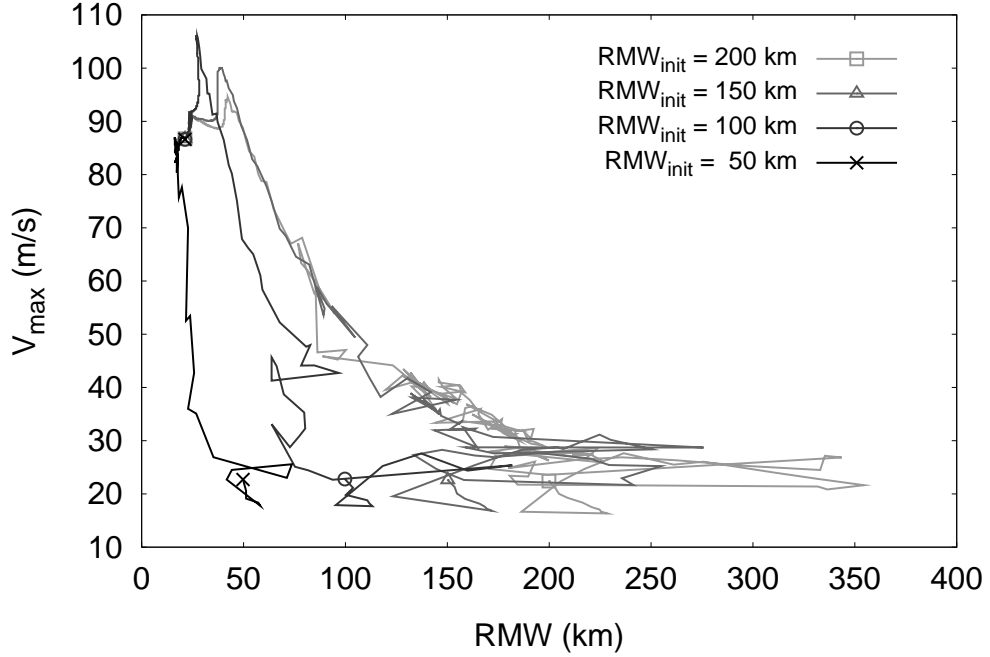
Figure 4.3: Trajectories in a phase diagram spanned by maximum horizontal wind speed and RMW for different initial RMW values (50 km, 100 km, 150 km, 200 km). A marker is plotted at the starting point ($t = 0$ h) and the final point ($t = 4000$ h) on each trajectory.

HURMOD are in qualitative agreement with the findings by Rotunno and Emanuel (1987) and Xu and Wang (2010). Presumably, there also exists a lower and an upper threshold for the size of the initial disturbance to form a tropical cyclone in HURMOD. However, within the range of the spatial extent for the initial vortex investigated here, all disturbances develop sooner or later into a TC.

4.4.2   Parameter sensitivity

To investigate the sensitivity of TCs to environmental moisture content, we have run simulations for case I and the moist-neutral case N with an initial tropospheric relative humidity of $RH_{ref} = 50\%$, 60%, 70%, and 80%, respectively. In the final stage, the TCs have a similar structure, but differ in their spatial extent and vortex strength. Radial-vertical profiles of relative humidity and radial velocity for two different values in RH_{ref} for case N and case I are displayed in Fig. 4.4. Outside the storm core, a relatively dry region forms above the boundary layer at mid-tropospheric levels. Further outward in the far-field environment, relative humidity becomes approximately uniform in the horizontal plane and increases with height to form a stratus cloud at upper tropospheric levels.

As can be seen in Figs. 4.4 and 4.5, case N and case I show a contrasting behaviour in response to different values in RH_{ref}. In case N, the TC becomes stronger (i.e. more intense)
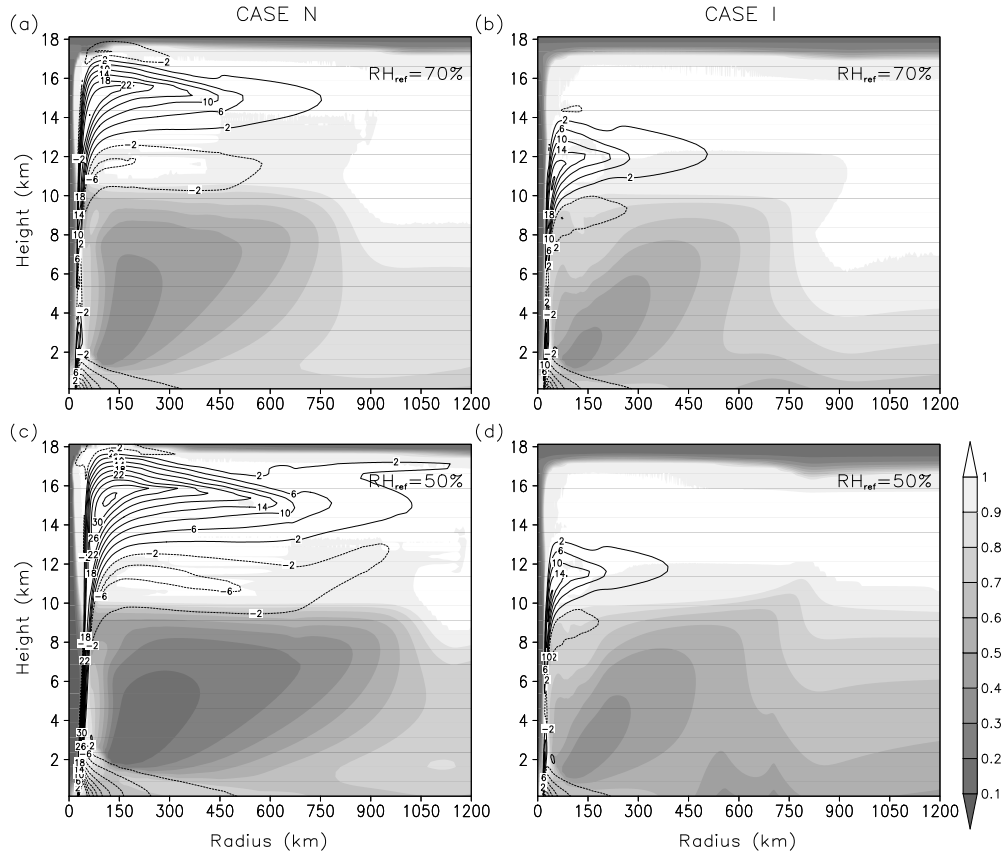
Figure 4.4: Radial velocity (contour lines) and relative humidity (shadings) fields for two different values in initial tropospheric relative humidity: $RH_{ref} = 70\%$ in the upper panels (a) and (b), and $RH_{ref} = 50\%$ in the lower panels (c) and (d). Stable state results averaged over the last 120 h of the 4000 h simulations for case N are displayed on the left, and those for case I on the right.

and more spacious with decreasing RH_{ref}, whereas in case I the trend is vice versa. It can also be seen that the sensitivity of the intensity to RH_{ref} is stronger in case N than in case I. The latter result is closer to findings by Wang (2009) and Hill and Lackmann (2009). Both studies detected a rather weak dependence of storm intensity with regard to environmental relative humidity in 3-D model simulations. Moreover, the sensitivity of TC size to RH_{ref} in case I corresponds with results from the modelling study by Hill and Lackmann (2009), who found that the lateral extent of TCs increases with increasing environmental moisture content. As pointed out by Gray (1979), an enhanced relative humidity at mid-tropospheric levels is favourable to the formation of TCs, and hence expected to be a determining factor with regard to their frequency of occurrence. This is partially confirmed by a more recent modelling study of Zhao and Held (2012). According to their results, mid-tropospheric relative humidity and TC frequency are strongly correlated in all ocean basins, expect the South Pacific. This
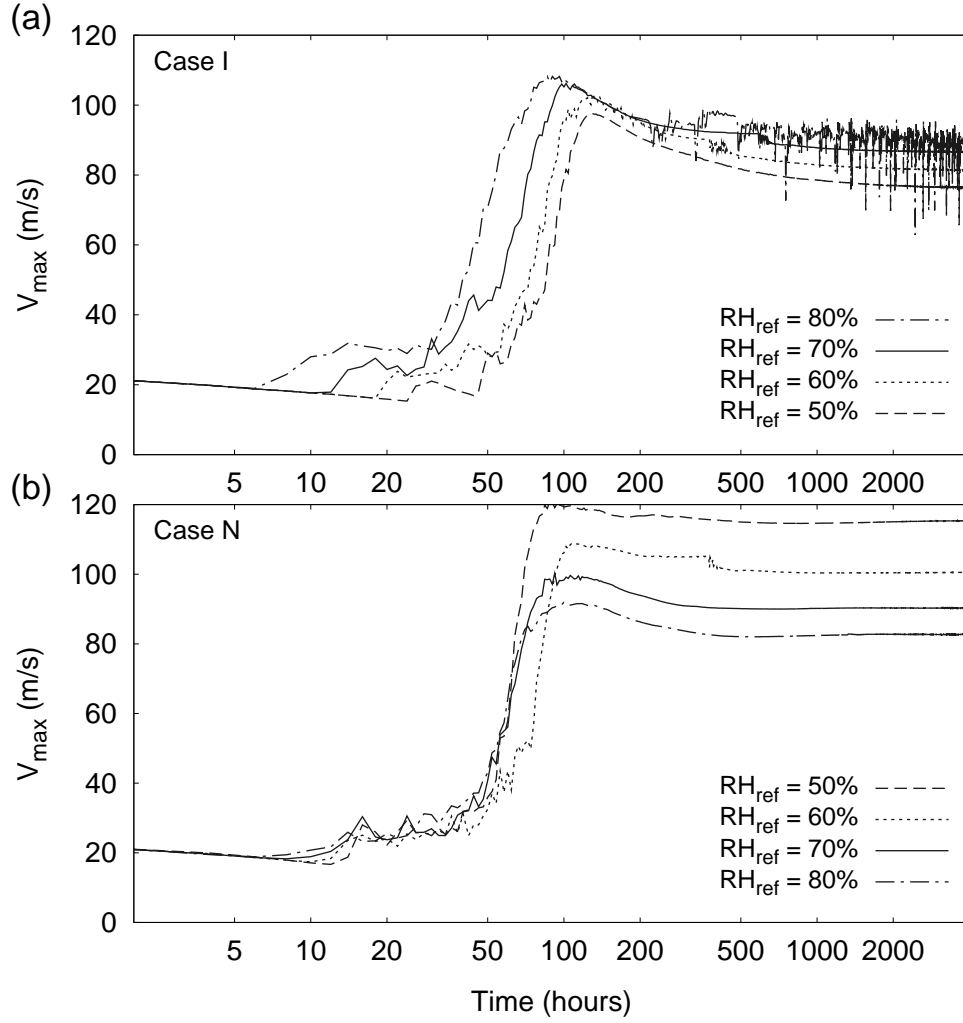
Figure 4.5: Time development of maximum horizontal wind speed for (a) case I with a constant equilibrium tropopause temperature of $T_t = -70°$C, and (b) the moist-neutral case N, in simulations with differing parameter values for the reference relative humidity, RH_{ref}. Note, the time scale is logarithmic.

suggests that the case I scenario is more realistic than the case N scenario. For $RH_{ref} = 80\%$ in case I, no equilibrium is reached. Instead, high-frequency fluctuations occur, which are related to convection in the ambient region. For this scenario, the reference troposphere becomes unstable giving rise to convective bursts in the ambient region, which act to disturb the flow within the TC thereby diminishing its intensity. In both cases I and N, the relative humidity under the eyewall in the final stage appears to be correlated to RH_{ref}, i.e. the higher RH_{ref}, the higher RH under the eyewall. For a 10%-change in RH_{ref}, we obtain a difference of $\sim 1\%$ at the lowest model level beneath the eyewall (not shown). Camp and Montgomery (2001) found a similar sensitivity of the Emanuel-model with regard to RH beneath the eyewall to that we see in case N, whereas case I displays a RH-sensitivity rather

similar to that found by Holland [cf. Fig. 1 in Camp and Montgomery (2001)].

In the case I scenario in HURMOD, the sensitivity of TC intensity to RH_{ref} is rather low compared to that in case N (Fig. 4.5). On the other hand, the sensitivity of the amplitude threshold, which appears in the non-neutral case I (and J), is quite high. This becomes evident from simulations with different initial vortex strength given by the initial central surface pressure difference, Δp_{init}, between the core and the environment (Fig. 4.6). For $RH_{ref} = 70\%$ (Fig. 4.6a), even very weak cyclonic disturbances with a central surface pressure reduction of only 2 hPa develop into a TC, whereas for $RH_{ref} = 50\%$ (Fig. 4.6b), an initial pressure reduction of ~ 10 hPa is required to finally reach the TC state. From this we would expect that environmental relative humidity has a considerable impact on the frequency of occurrence of TCs. This also agrees with findings from recent observational data over the Bay of Bengal (Yanase et al., 2012).

The results from HURMOD simulations also show that tropospheric dry static stability plays a certain role with regard to the frequency of occurrence of TCs, but primarily it appears to have a strong impact on TC intensity. This can be seen by comparison of Fig. 4.6a and Fig. 4.6c, and in Fig. 4.7. The latter shows the evolution of TCs for four different values in the reference tropopause temperature in the case I scenario. As mentioned in section 4.3, in all case I and J simulations, the reference temperature profile is assumed to be linear, i.e. altering the environmental T_t value at a constant SST implies a change in dry static stability. If we lower the dry static stability by increasing the tropopause temperature by 5°C within the range of $-70°C \leq T_t \leq -60°C$, and $T_s = 30°C$, the maximum wind speed decreases by $14-15$ m/s (Fig. 4.7). For an even lower tropopause temperature of $T_t = -75°C$, the reference troposphere becomes unstable and fluctuations in the flow field occur, which are similar to those, we obtain for $RH_{ref} = 80\%$ (see above). However, as long as the troposphere in the ambient region does not become moist-statically unstable, our results show that the lower the dry-static stability, the higher is the intensity of the storm and the lower is the amplitude threshold. This is in agreement with results from previous studies based on observations over different ocean basins (Zeng et al., 2008; Wada et al., 2012). Wada et al. (2012) pointed out that the relatively low static stability over the western Pacific compared to that over the eastern Pacific is a relevant factor to explain why TCs are stronger over the western than over the eastern Pacific.

Moreover, both observation and modelling-based studies (Zeng et al., 2008; Yu et al., 2010) confirm that the outflow temperature at upper tropospheric levels is an important factor with regard to maximum potential intensity, as anticipated in the earlier theoretical studies, based on the description of the energy cycle of a TC in analogy to that of a Carnot heat engine (Kleinschmidt, 1951; Emanuel, 1986, 1995a; Bister and Emanuel, 1998). In this
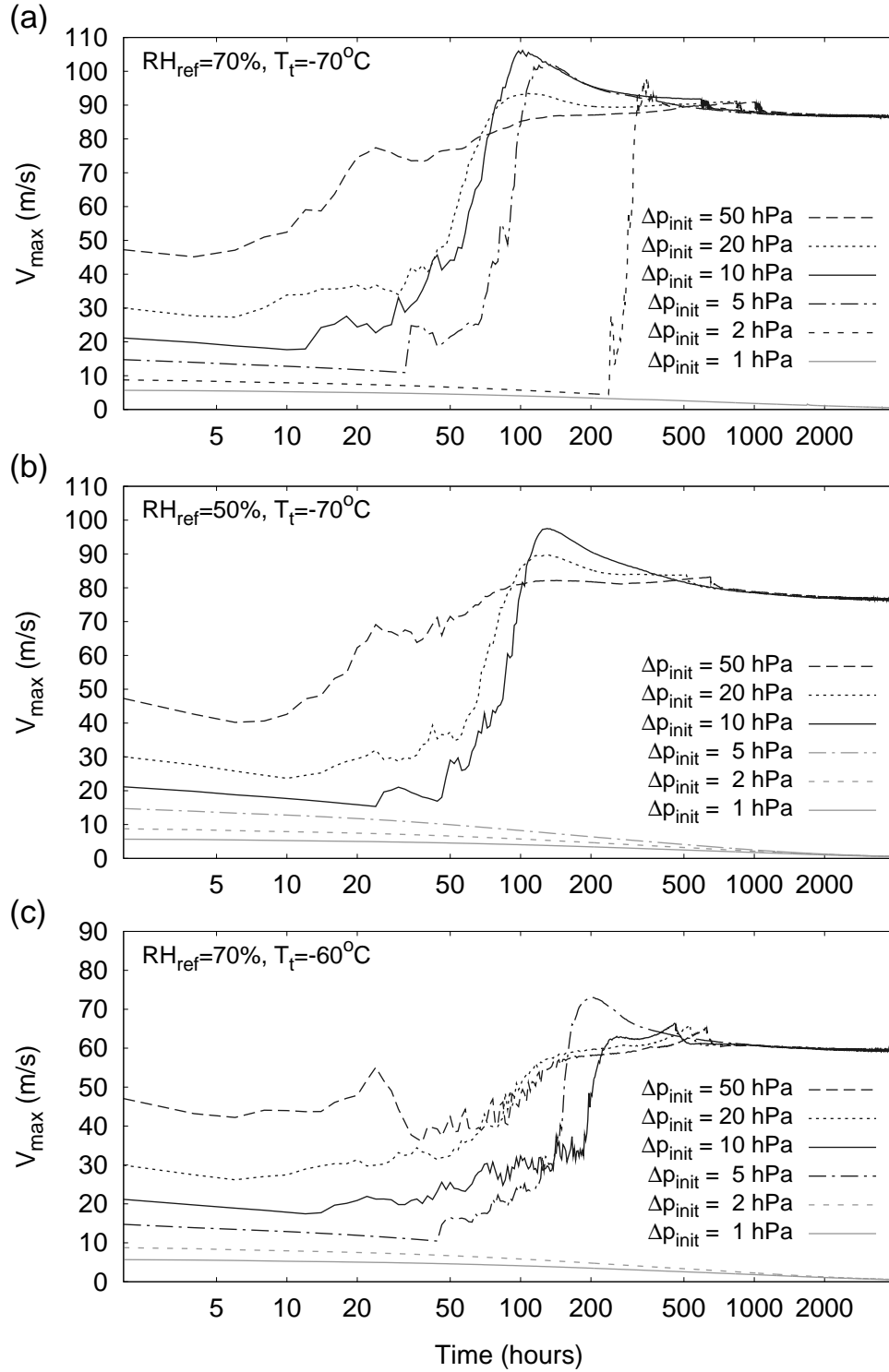
Figure 4.6: Time development of maximum horizontal wind speed in case I, for varying initial vortex strength given by the initial central surface pressure difference, Δp_{init} (hPa), between the core and the environment in simulations with differing parameter values for the reference relative humidity, RH_{ref}, and the tropopause temperature, T_t, from top to bottom: (a) $RH_{ref} = 70\%$ and $T_t = -70^oC$, (b) $RH_{ref} = 50\%$ and $T_t = -70^oC$, and (c) $RH_{ref} = 70\%$ and $T_t = -60^oC$. Initial disturbances that reach TC strength are displayed by black lines, non-developing systems by grey lines. Note, the time scale is logarithmic.
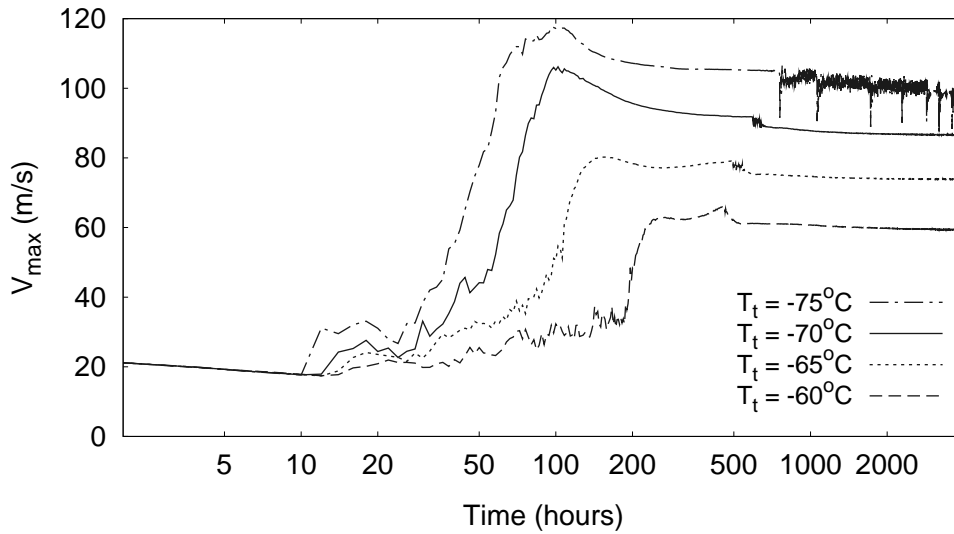
Figure 4.7: Time development of maximum horizontal wind speed for case I in simulations with differing parameter values for the tropopause temperature, T_t. Note, the time scale is logarithmic.

view, the thermodynamic efficiency of the system is a function of the difference between the inflow temperature near the surface, and the outflow temperature in the upper troposphere [cf. Eq. (2.5)]. Changes in the tropopause temperature are also reflected in the outflow temperature of the storm at upper tropospheric levels. As the vertical extent varies with intensity in HURMOD, we estimate the outflow temperature T_{out} by assuming that it corresponds approximately to the temperature at the point, where the radial velocity reaches 2 m/s at the outermost location in the outflow layer. By comparison of the simulations shown in Fig. 4.7 with T_t equal to $-60°$C, $-65°$C, and $-70°$C, respectively, we find that a drop of $5°$C in T_t in the ambient region corresponds to a drop of about $7°$C in T_{out} (not shown). Hence, the colder T_t, the colder T_{out}, so that the thermodynamic efficiency rises, and, as expected, the TC becomes more intense.

This may also provide an explanation for the behaviour, we obtain in case N with regard to the reference value of relative humidity. As discussed above, the sensitivity to RH_{ref} in the non-neutral case N is opposite to that found in case I. This is due to the moist-neutral adjustment, which results in colder temperatures in the outflow region at upper tropospheric levels for a drier reference troposphere. Thus, the lower RH_{ref}, the higher becomes the thermodynamic efficiency (and vice versa) in case N. Furthermore, the moist-neutral adjustment leads to a slightly higher efficiency at lower SSTs, i.e. the weakening effect of SST cooling may be partially offset by an enhanced thermodynamic efficiency, providing a possible explanation for the relatively low sensitivity of the intensity to the SST in case N, which will be displayed in the following subsection (cf. Fig. 4.8).

4.4.3   Dynamical system properties

The dynamical behaviour of the vortex in response to changes in the SST, depends on whether the tropospheric reference-state is chosen to be moist-neutral (case N) or not (case I and J). This becomes evident from simulations, which are started from a stable state with $T_s = 30°$C, and are exposed to a very slow surface temperature cooling at a rate of 10^{-3} °C/h, until either a SST of 20°C is reached, or a SST, where the storm dies off (Fig. 4.8). Additionally, we have run long-term simulations at different constant SSTs in order to assure that the results from the cooling experiments are not chiefly due to transient dynamics related to the continuous changes in SST. As can be seen in Fig. 4.8, we obtain only little sensitivity to the SST in case N, where the maximum wind speed in the eyewall decreases only slightly with decreasing sea surface temperature. In contrast, the non-neutral cases I and J deliver a generally higher sensitivity to SST as well as rather sudden changes in V_{max}, which hints to the existence of bifurcation points.
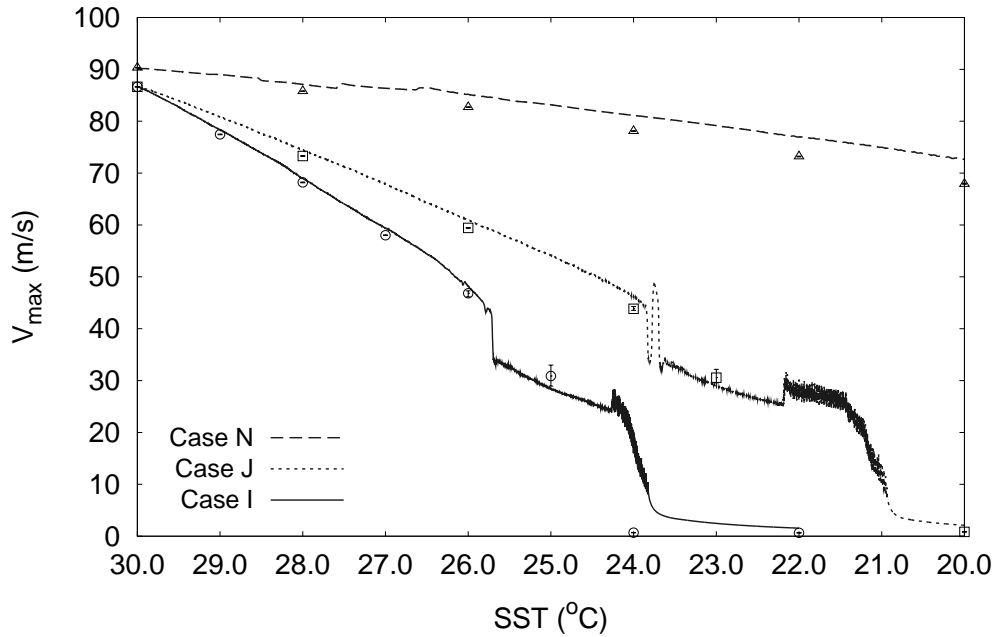

Figure 4.8: Development of maximum horizontal wind speed with decreasing SST with time at a cooling rate of 10^{-3} °C/h for the moist neutral case N (dashed line), case J with $\Gamma = const.$ (dotted line), and case I with $T_t = const.$ (solid line). Average values over the last 120 h of the 4000 h-runs at fixed SSTs are plotted with different markers for case N (triangles), case J (squares), and case I (circles). Error bars display the full range of maximum wind speed during the last 120 h of the long-term runs.

Case I and case J behave qualitatively very similar, but differ quantitatively in their dependence on the SST. For our standard configuration with $T_t = -70°$C and $RH_{ref} = 70\%$, case I weakens faster with decreasing SST than case J, where the far-field temperature lapse rate is held constant at $\Gamma = 0.00\bar{6}$ K/km. The first jump in vortex intensity occurs at $T_s \simeq 25.8°$C in case I, and at $T_s \simeq 23.8°$C in case J. One can also see that the storm entirely decays at SSTs close to 24°C in case I, whereas in case J we still obtain quasi-steady state vortices of tropical storm intensity at SSTs near 22°C. We note, unlike in the other long-term experiments displayed in Fig. 4.8, a steady state associated with a tropical storm is not reached after 4000 h in the case J run with a constant SST of 22°C (not shown here). In this experiment, a maximum horizontal wind speed of ~ 28 m/s is reached after two days, which then slightly decreases, re-intensifies, and then fluctuates between ~ 27 m/s and ~ 34 m/s for several days, after which fluctuations become small and the storm continuously weakens to $V_{max} \sim 25$ m/s, before it starts to oscillate again (after about 50 days of running time), with a very slow decreasing trend, and increasing amplitudes in the fluctuations. If we ran this simulation for even longer, we would expect the storm to slowly weaken further, until it finally decomposes and the atmosphere approaches a state of rest. A similar behaviour is reflected in the cooling experiment.

Recalling the results shown in subsection 4.4.2, the quantitative differences in case I and case J can be simply attributed to the difference in their static stability, and outflow temperatures, which arises between these two cases when the SST is changed. In the cooling experiments shown here, the reference temperature lapse rate is continuously decreased in case I and kept constant in case J, which affects the potential intensity via a higher or lower dry static stability, and thermodynamic efficiency as discussed in the previous subsection (cf. Fig. 4.7). A comparison of different cooling experiments in case I further evinces the relevance of the tropospheric temperature stratification. The maximum horizontal wind speed in response to surface cooling for three different settings regarding tropopause temperature and reference relative humidity are shown in Fig. 4.9. The weakening rate of the vortex in the strong TC state appears to be similar and independent of the tropospheric reference state. On the other hand, the SST at which a rapid weakening takes place as well as that below which the storm decays completely, are strongly sensitive to the thermodynamic reference conditions, especially to the tropopause temperature.

The jump in maximum wind speed appears to be most pronounced or abrupt in the reference run, displayed by a solid line in Fig. 4.9. For a drier reference atmosphere ($RH_{ref} = 50\%$), displayed by a dotted line, the cyclone displays vacillations between the high-intensity and the low-intensity state within a small SST-range, before it settles into the lower tropical storm state. In a run with a higher cooling rate, similar vacillations (not shown) appear, and
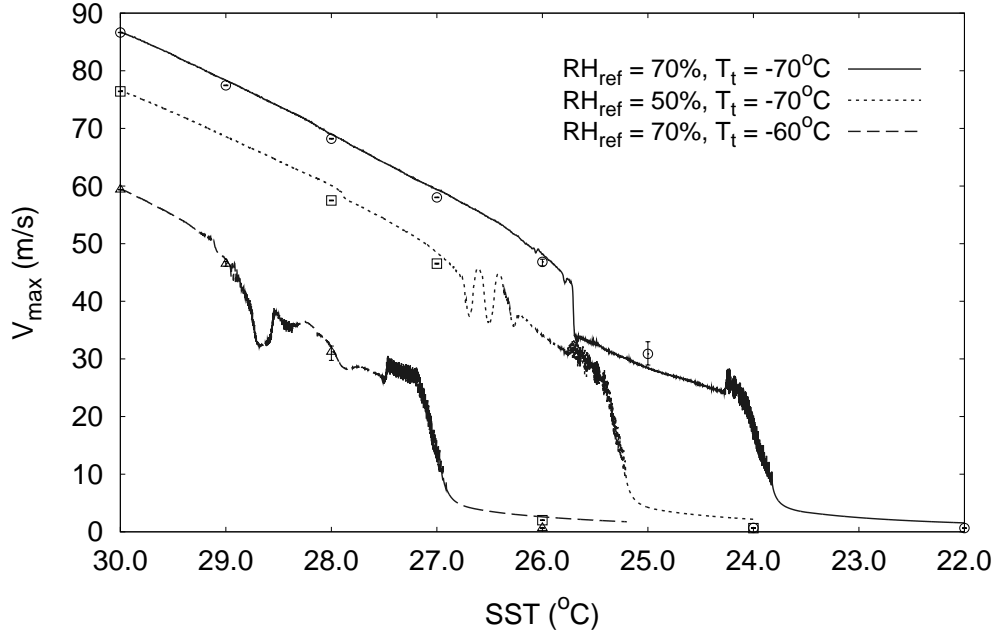
Figure 4.9: Development of maximum horizontal wind speed with decreasing SST with time at a cooling rate of 10^{-3} °C/h in case I for three simulations with differing parameter values for the reference relative humidity, RH_{ref}, and the tropopause temperature, T_t. Average values over the last 120 h of the 4000 h-runs at fixed SSTs are plotted with different markers for $RH_{ref} = 70\%$ and $T_t = -70$°C (circles), $RH_{ref} = 50\%$ and $T_t = -70$°C (squares), and $RH_{ref} = 70\%$ and $T_t = -60$°C (triangles). Error bars display the full range of maximum wind speed during the last 120 h of the long-term runs.

one vacillation also occurs in the cooling experiment for case J (see Fig. 4.8, dotted line). In the SST-range between the first drop in maximum wind speed and before the decay of the cyclone, the surface cooling experiment with a warmer tropopause ($T_t = -60$°C), displayed by a dashed line in Fig 4.9, does not exhibit such a monotonous, relatively smooth decrease in V_{max} as the standard run ($T_t = -70$°C), nor do we see rather rapid fluctuations between a strong TC state with $V_{max} \geq 44$ m/s and, following the classification according to the SSHS, a tropical storm or relatively weak TC state with $V_{max} \leq 35$ m/s as in case J. However, if we compare the quasi-steady state obtained from long-term runs at a fix SST with $T_s = 26$°C for the standard experiment, and $T_s = 28$°C for the experiment with $T_t = -60$°C in case I, and with $T_s = 23$°C in case J, we find that they are almost identical, in terms of their final intensity (see Figs. 4.8, 4.9) and spatial extent (not shown). The mean value of V_{max} is close to 31 m/s and slightly fluctuates by an amount of $\sim 1 - 1.5$ m/s around its mean value in these three experiments.

Overall, this gives rise to the assumption that the principal equilibrium structure in case I and J is, at least within a certain parameter range, fairly robust to changes in the reference

lapse rate. For drier initial conditions, the SST range within which a lower equilibrium corresponding to a weak TC or a tropical storm exists, appears to narrow. In the simulation with $RH_{ref} = 50\%$, the equilibrium solution representing the TC state may either vanish or the attractor may possibly turn directly into a repellor at a certain SST between 27°C and 26.0°C, so that the TC quenches off instead of first experiencing a transition to some lower or second stable state before the cyclone decomposes.

To investigate the behaviour and the character of the bifurcation in the range, where the transition from a strong TC state to a tropical storm takes place in more detail, we carried out another sea surface cooling and a warming experiment with the standard configuration in case I ($RH_{ref} = 70\%$, $T_t = -70$°C). The result for SSTs between 26.6°C and 25°C is shown in Fig. 4.10. Here, we applied a very low cooling (warming) rate of $2 \cdot 10^{-4}$ °C/h to further reduce effects related to transient rather than to steady state behaviour. The warming experiment (brighter grey line) was started from a 4000 h-run with $T_s = 25$°C, and the cooling experiment (dark grey line) from the stable state of the 4000 h-run at $T_s = 27$°C. In the cooling experiment, the decrease in V_{max} with declining SST is smooth for $T_s \geq 26.2$°C. At slightly colder SSTs, the decreasing trend persists, but V_{max} starts to fluctuate irregularly. The amplitude of these chaotic fluctuations rises with decreasing SST until an abrupt decrease in V_{max} between 25.9°C and 25.8°C occurs, where V_{max} drops from ~ 45 m/s to ~ 32 m/s. As the SST is further cooled down, V_{max} fluctuates again, but stays below 38 m/s with a slight decreasing trend. The warming experiment displays irregular fluctuations with a maximum amplitude of ~ 3 m/s near $T_s = 25$°C, and an increasing trend in V_{max} as the sea surface gets warmer. The fluctuations decline and almost vanish at $T_s = 25.3$°C. At higher SSTs, V_{max} increases almost monotonously, until the SST reaches a value of about 25.5°C, where V_{max} starts to oscillate regularly. These oscillations appear to be almost sinusoidal with a low frequency. Close to a SST of ~ 26°C, the oscillations disappear, and V_{max} rises almost monotonously with increasing SST.

The abrupt jump, we find in the surface cooling experiment, points to the existence of a bistability, whereas the oscillations in the surface warming experiment rather infer that there is a transition from a fixed point attractor to a limit cycle indicating a Hopf bifurcation. To further elucidate the actual behaviour of the dynamical system, we compared experiments started from the cooling and the warming simulations displayed in Fig. 4.10 at three distinct SSTs in vicinity of the bifurcation point (Fig. 4.11). For $T_s = 26.2$°C and $T_s = 25.4$°C, the two curves converge, giving further evidence for the existence of a fixed point attractor (Fig. 4.11a,c). As can be seen in Fig. 4.11b, the simulation started from the warming experiment (brighter grey line) reveals the existence of a limit cycle attractor at $T_s = 25.8$°C, with V_{max} oscillating sinusoidal between ~ 34 m/s and ~ 44 m/s. The shape of the V_{max}-curve
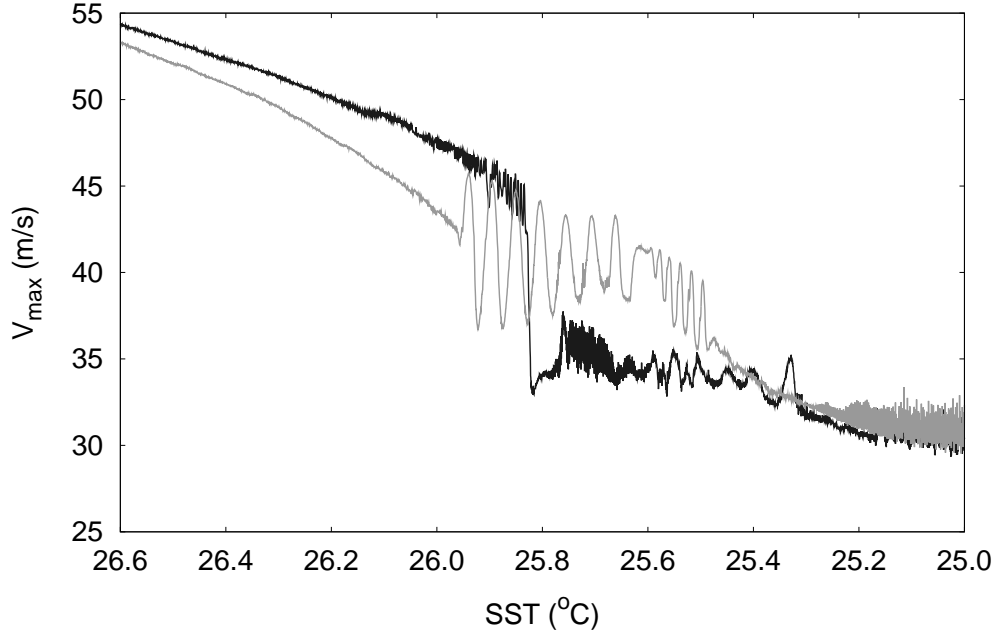
Figure 4.10: Development of maximum horizontal wind speed with decreasing SST (dark grey line), and increasing SST (brighter grey line) in time at a rate of $2 \cdot 10^{-4}$ °C/h.

obtained in the simulation that was started from the cooling experiment (dark grey line) is more ambivalent. Over the first 25 days at a constant sea surface temperature, it displays the behaviour of a limit cycle, too. After this time, the oscillation appears to decline, approaching a value of about 37 m/s, before it starts to oscillate again after 80 days of running time. Finally, the oscillation seems to approach the same period and amplitude that we find in the experiment started from the warming simulation[25]. This strongly suggests that there are two Hopf bifurcations within a relatively narrow sea surface temperature range ($25.4°C < T_s < 26.2°C$ in the standard case I experiment): the first one, at which the fixed point attractor turns into a limit cycle and the second one, where it is vice-versa. Coming up from higher (lower) SST values, the steady state solution seems to approach the maximum (minimum) value of the limit cycle in vicinity of the respective bifurcation. However, this behaviour seems to be rather sensitive to the environmental moisture content. In a drier environment, below a certain value for RH_{ref}, the Hopf bifurcations probably disappear (see above).

---

[25]To test the robustness of the limit cycle behaviour, the simulations at 25.8°C were continued and run 2000 hours longer (not shown). The oscillation with a period of about 225 hours is sustained in both experiments.
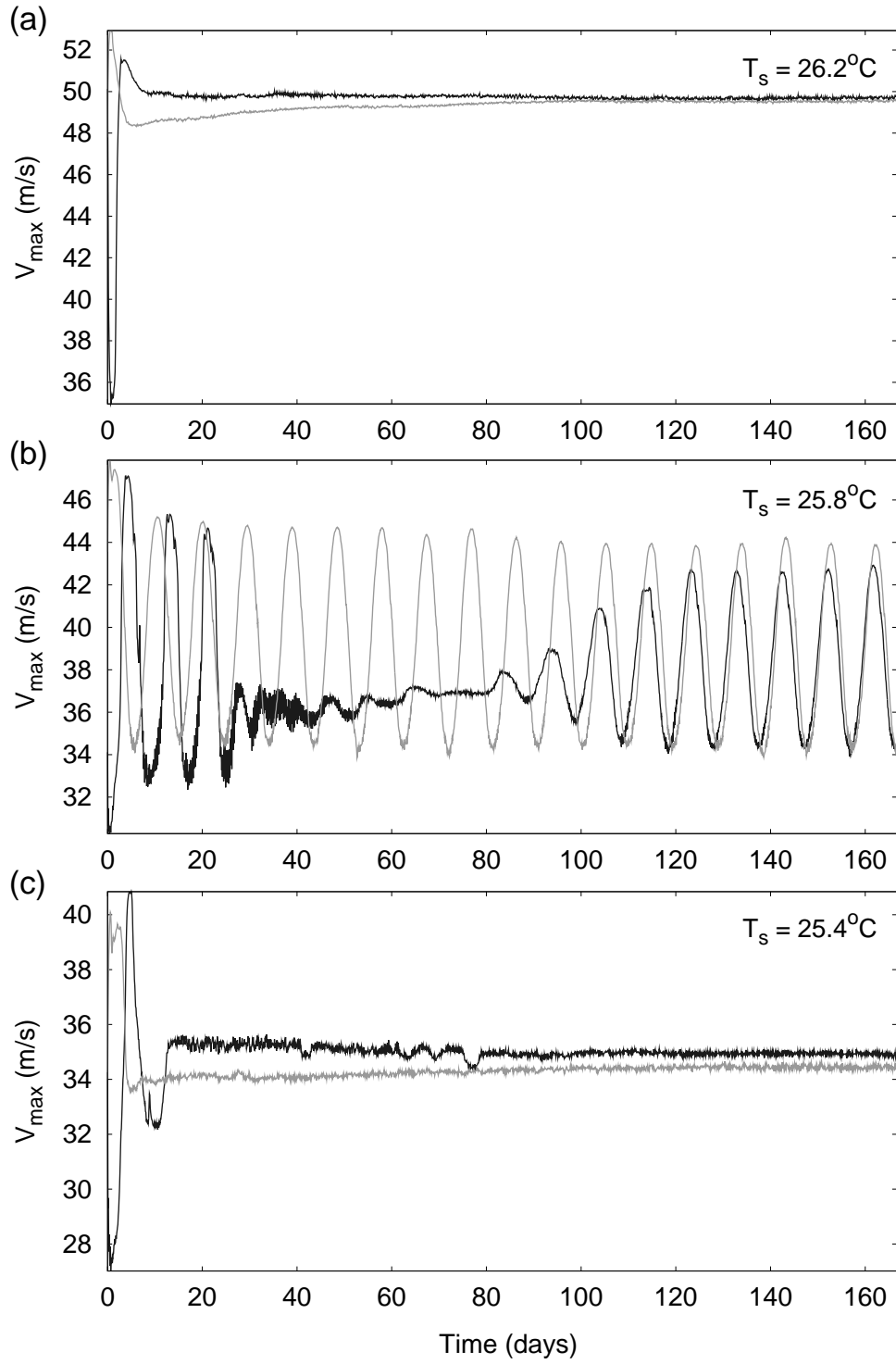
Figure 4.11: Time development of maximum horizontal wind speed in case I for different fix SST values in vicinity of the bifurcation from top to bottom: (a) $T_s = 26.2^oC$, (b) $T_s = 25.8^oC$, and (c) $T_s = 25.4^oC$. Each simulation was started at the respective SST from the simulation with decreasing SST (dark grey lines), and increasing SST (brighter grey line) in time (cf. Fig. 4.10).

4.5   Discussion

In several aspects, the results from the convection-resolving model HURMOD, shown in the previous section, do agree with those gained from a conceptual TC model, which was introduced in the previous chapter and published by Schönemann and Frisius (2012). On the other hand, there are also qualitative differences in the behaviour of these two models. In the following, we will discuss the principal results from HURMOD with respect to those of the low-order model, and address possible reasons for their disagreement in some points.

Above a certain SST threshold, we obtain an equilibrium solution, which is associated with a stable TC state in both models. In the moist-neutral case N2 in the conceptual model, where neutrality in the environment is achieved via a temperature adjustment, this SST threshold is unrealistically low, i.e. far below tropical SSTs (cf. Fig. 3.10a). The moist-neutral Case N in HURMOD does not exhibit any bifurcations within the range of tropical SSTs either. Moreover, in both models, the intensity of the TC displays a rather weak dependence on SST in the respective moist-neutral cases. In this respect, the models behave very similar, but their response to changes in the initial environmental humidity in the moist-neutral configuration appears to be remarkably different from each other. In the conceptual model, TC intensity decreases with decreasing relative humidity in the ambient region. This appears to be directly opposite to what we observe in the moist-neutral case N configuration in HURMOD, where TC intensity rises with decreasing reference relative humidity. In this context, it is important to point out that there are two relevant exogenous relative humidity parameters in the low-order model: RH in the free troposphere of the ambient region, and RH in the boundary layer below. The effect of the latter has not been discussed in chapter 3, but a subsequent analysis exhibits that the response to these two parameters is in opposite direction in the conceptual model (not pictured). Hence, there is a qualitative agreement among the two models in the moist-neutral configuration with regard to their sensitivity to relative humidity in the boundary layer of the inflow region. The discrepancy regarding the sensitivity to environmental RH at mid-tropospheric levels is chiefly attributable to the different way in which the neutrality adjustment of both models works and resulting differences in the impact on tropospheric RH distribution, temperature stratification, and outflow temperature. The neutrality adjustment in HURMOD results in a steeper vertical temperature gradient and a lower outflow temperature at a lower environmental relative humidity. This is similar in the low-order model when environmental boundary layer RH is varied and free-tropospheric RH is fixed, and vice versa when free-tropospheric RH is varied and boundary layer RH is fixed.

For the remaining part of this section, we focus on the discussion of the non-neutral cases I and J. In both models, HURMOD and the conceptual model, the equilibrium solution is

independent of the initial vortex strength, as long as it does not fall below a certain limit, and the strong TC state is represented by a fixed point attractor. The finite amplitude nature of TCs, referring to the existence of an amplitude threshold with respect to the strength of the initial disturbance, has been discovered in model experiments by Rotunno and Emanuel (1987) and becomes also evident from HURMOD simulations. In HURMOD, the vortex strength limit or amplitude threshold is sensitive to the tropopause temperature and atmospheric moisture content (cf. Fig. 4.6), and obviously exists over the whole SST range, we investigated in HURMOD. On the other hand, in the low-order model, the amplitude threshold vanishes beyond a certain SST, so that even smallest initial disturbances would sooner or later grow into strong TCs (cf. Fig. 3.14b). This may be possibly due to the comparatively rudimentary representation of turbulence in the conceptual model, which does not incorporate the effect of horizontal eddy-diffusion. However, for now, this issue remains highly speculative.

As has been depicted in the previous section, there is a second amplitude threshold associated with a critical SST in HURMOD, below which, according to the SSHS classification, TCs only reach tropical storm or minor TC strength. Looking at the case I and J configuration, we see that the critical SST of that amplitude threshold is sensitive to the environmental (reference) lapse rate and tropopause temperature in a qualitatively similar manner as the amplitude threshold defined by a subcritical saddle node bifurcation in the low-order model (cf. Figs. 3.8, 4.8, and 4.9). However, in view of the fact that major TCs can form from initial wind speeds close to zero beyond a certain SST in the conceptual model, the amplitude threshold there can probably not be identified with the SST-dependent amplitude threshold in HURMOD.[26] Notwithstanding, the sensitivity to the reference lapse rate and the related outflow temperature of both TC intensity and the SST above which strong TCs may arise, is rather similar among the two models.

The influence of the environmental moisture content is investigated by application of different time-invariant values for relative humidity in the ambient region in the low-order model, and different initial values for the tropospheric relative humidity in HURMOD (see subsection 4.4.2). Although, as noted above, these two quantities cannot be considered as perfect analogons, they serve as a measure for the environmental moisture content in the respective model, and in the following, we will refer to both as RH_{ref}. In the conceptual model, the equilibrium intensity is only slightly sensitive to RH_{ref}, i.e. for the standard case I configuration, the maximum wind speed only rises by about 0.5 m/s per 10% rise in RH_{ref}

---

[26]We note that this question cannot be answered with certainty here, since we have not tested, whether spontaneous cyclogenesis occurs at SSTs much higher than 30°C in HURMOD or not.

(not shown). The intensity in the corresponding HURMOD simulations exhibits a higher sensitivity to RH_{ref} (see Fig.4.5a).

With regard to the amplitude threshold, both models are visibly sensitive to the environmental moisture content (cf. Fig. 3.4a). In HURMOD this becomes evident by comparison of Fig. 4.6a and 4.6b. This gives a further indication that the subcritical saddle node bifurcation, marking the SST threshold above which TCs can grow from disturbances close to zero in the low-order model actually corresponds to the lower amplitude threshold in HURMOD rather than to the upper strong TC threshold. The second, or upper amplitude threshold is apparently not captured by the conceptual model. In the following, we aim to elucidate some of the causes of the differences in the equilibrium structure of the two models in the parameter range, where the cyclonic system reaches at least tropical storm or category I TC strength on the SSHS. For this purpose, we will further look at the behaviour of the TC in vicinity of the Hopf bifurcations and in the limit cycle stage, we observe in HURMOD.

Several assumptions and approximations conducted in the conceptual model were adopted from Emanuel's theory on potential intensity of tropical cyclones. One such assumption is that the eye only plays a passive role, and hence entropy exchange between the eye and eyewall can be disregarded. The appropriateness of this simplification is challenged by Persing and Montgomery (2003), who claim that low-level fluxes of high-entropy air from the eye into the eyewall are highly relevant to the maximum intensity TCs can reach. They conclude that the neglect of these fluxes is the major reason for the underestimation of TCs' potential intensity by Emanuel's PI theory. In opposition to this, Bryan and Rotunno (2009b) argue that eye-eyewall entropy fluxes at low levels provide at most a small contribution to an enhanced maximum intensity (cf. section 2.7). In the light of these two opposing hypotheses, we want to figure out, whether eye-eyewall entropy fluxes are relevant for TC intensity in HURMOD, and whether they are essential to the existence of the limit cycle in the model.

Equivalent potential temperature, stream lines and radial velocity at lower tropospheric levels in the inner part of the storm are plotted for different stages of the limit cycle in Fig. 4.12, and for the weaker and stronger steady state in vicinity of the Hopf bifurcations in Fig. 4.13, respectively. At first glance, it seems that high-entropy air, coming from the eye and entering the eyewall, may indeed play a decisive role in stronger TCs. To test this, we carried out two sensitivity experiments in analogy to those performed by Bryan and Rotunno (2009b). For this purpose, the limit cycle simulation shown in Figs. 4.11b and 4.12 has been continued for 2000 h with 150% of the value of the surface exchange coefficient for heat and moisture, i.e. $C_H = 1.8 \cdot 10^{-3}$, within 1) a radius of 10 km, and 2) a radius of 12 km. The first sensitivity experiment, where the increase in C_H is confined to the eye, does not exhibit considerable changes in the course of the oscillation regarding the storm structure and its
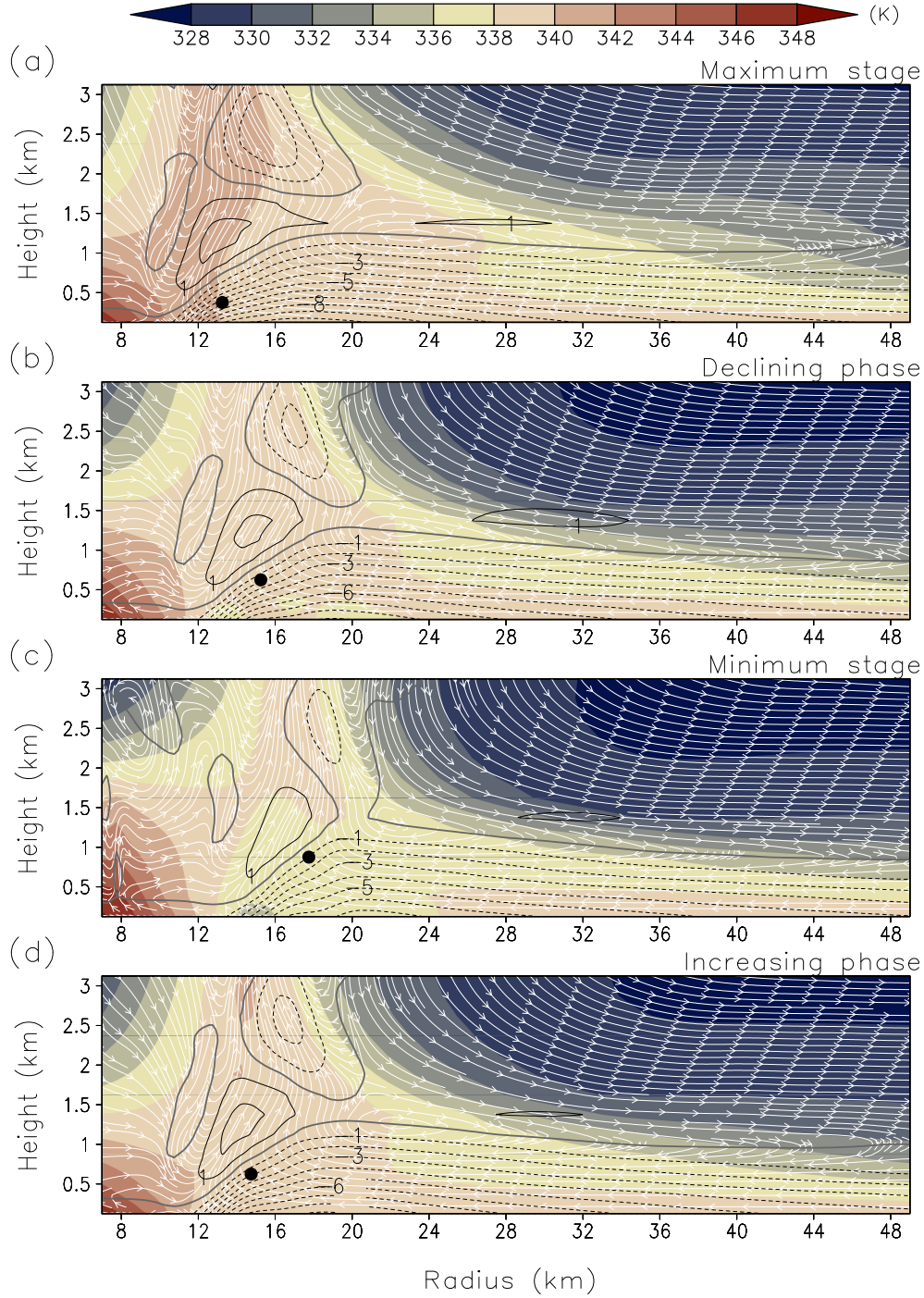
Figure 4.12: Equivalent potential temperature θ_e (colour shadings), stream lines (white) and radial velocity (contour lines) at lower tropospheric levels for the inner part of the TC in the case I standard configuration at different phases of the limit cycle from top to bottom: (a) maximal intensity, (b) declining intensity, (c) minimal intensity, and (d) increasing intensity. Higher θ_e-values are displayed in reddish shades, lower θ_e-values in bluish shades. Inward flow is indicated by dashed black lines, zero-radial velocity by thick grey lines and outward flow by solid black lines. The contour interval is 1 m/s. The location of V_{max} is marked by a black circle.
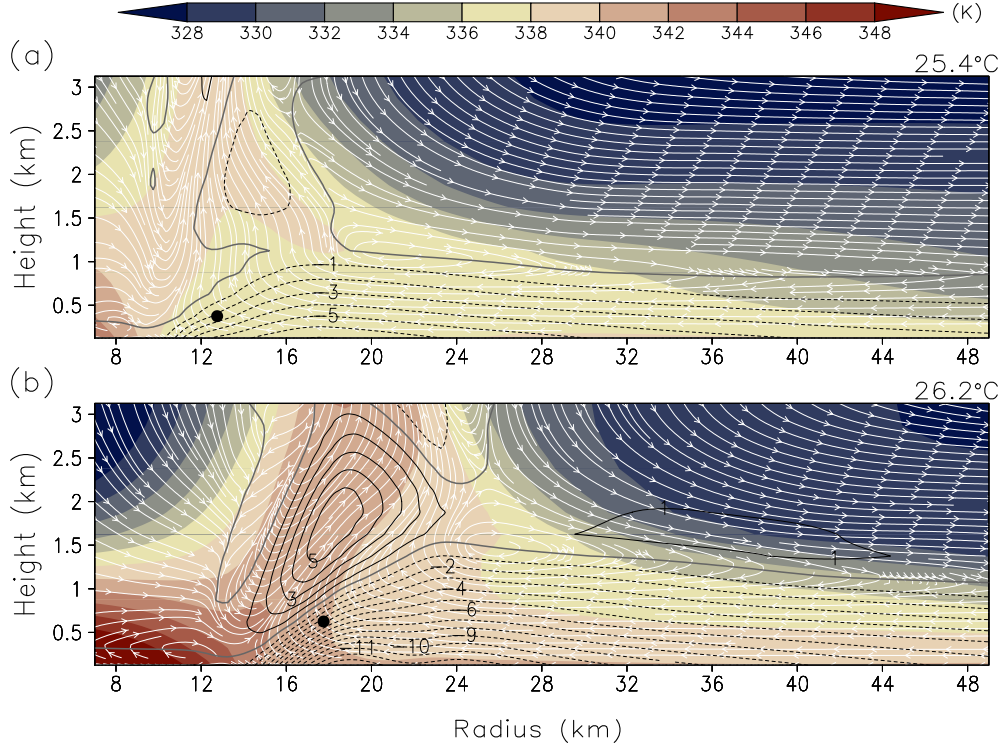
Figure 4.13: As in Fig. 4.12, but for the respective stable states surrounding the limit cycle: (a) at $T_s = 25.4^oC$, and (b) $T_s = 26.2^oC$.

maximum intensity outside the eye. On the other hand, in the second sensitivity experiment, where the region of increased surface enthalpy fluxes is slightly extended reaching into the inner eyewall, the amplitude of the oscillation rises and a maximum wind speed of up to ~ 46 m/s instead of 44 m/s is reached at the maximum stage of the limit cycle (not shown). So, while enhanced entropy fluxes beneath the innermost part of the eyewall do result in a distinctly increased intensity, we find that low-level entropy fluxes from the eye into the eyewall do not seem to be relevant to the maximum potential intensity of TCs, which agrees with results of Bryan and Rotunno (2009b). In this regard, the assumption that the eye itself responds to its surroundings rather than it actively acts on it, seems to be fairly reasonable.

In a follow-up study, Bryan and Rotunno (2009a) argue that gradient wind imbalance, and associated supergradient winds, is the determining factor to explain the exceedance of the maximum TC intensity predicted by Emanuel's PI theory (also referred to as "superintensity", see section 2.7). Concerns about the applicability of the so-called balanced-vortex assumption in the context of hurricanes have been raised already many decades ago [e.g. Gray (1962), Ooyama (1969) and citations herein]. The difference between tangential wind and gradient wind, $v - v_{gr}$, as well as vertical wind velocity in the eyewall region are plotted
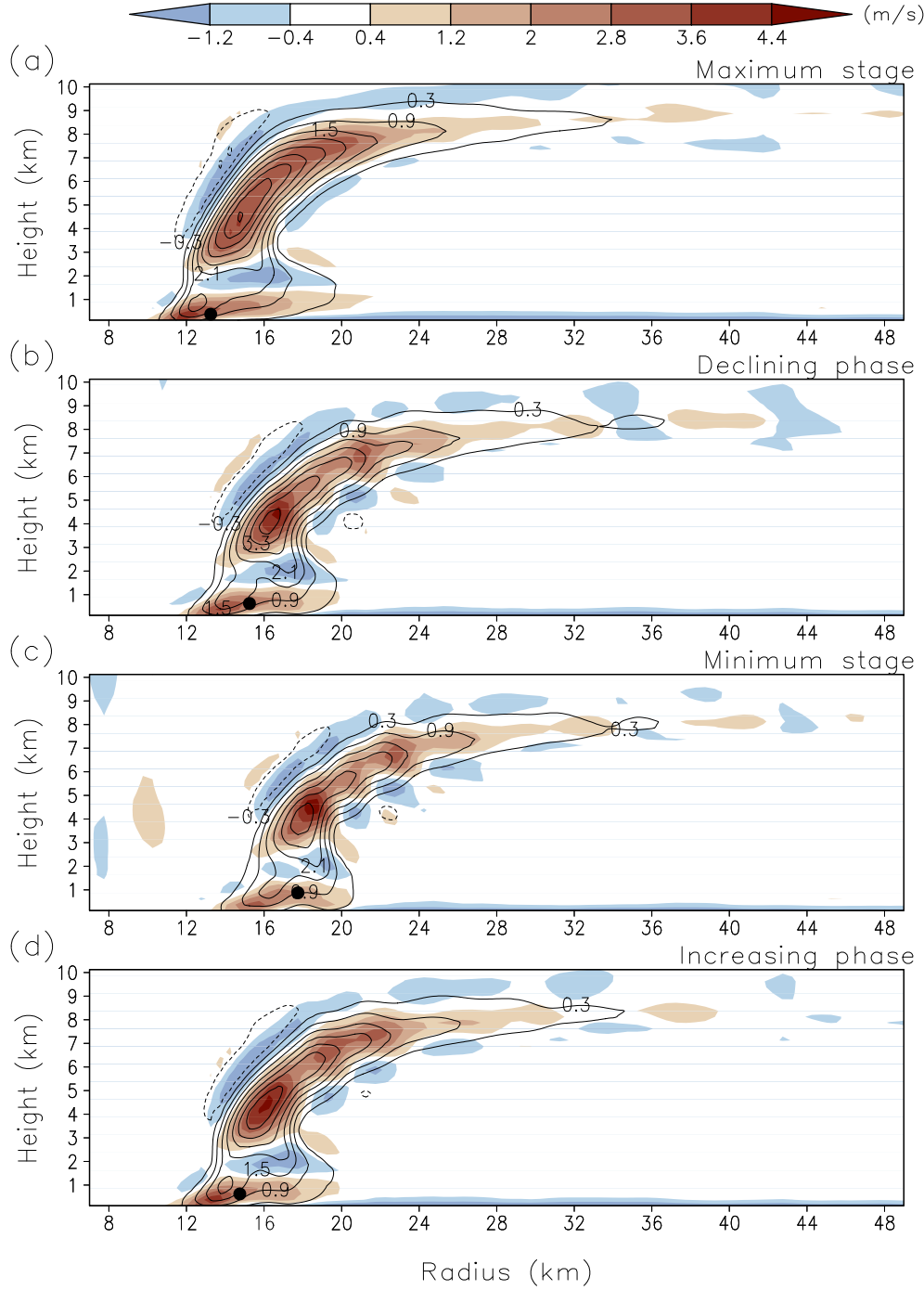
Figure 4.14: Difference between tangential wind and gradient wind (colour shadings), and vertical velocity (contour lines) for the inner part of the TC in the case I standard configuration at different phases of the limit cycle from top to bottom: (a) maximal vortex strength, (b) declining strength, (c) minimal strength, and (d) increasing strength. Red shades indicate supergradient winds, blue shades indicate subgradient winds, and white areas are in or close to gradient wind balance. Downward flow is indicated by dashed lines and upward flow by solid lines. The contour interval is 0.6 m/s. The location of V_{max} is marked by a black circle.
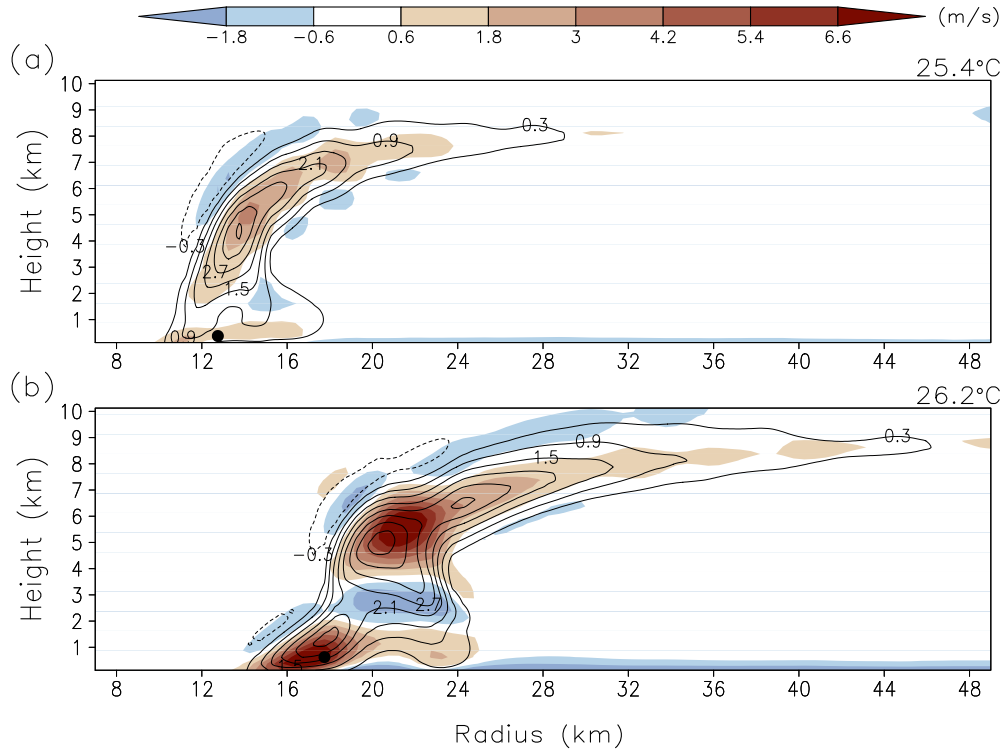
Figure 4.15: As in Fig. 4.14, but for the respective stable states surrounding the limit cycle: (a) at $T_s = 25.4°C$, and (b) $T_s = 26.2°C$. Note, the colour scale interval is larger than in Fig. 4.14.

for different stages of the limit cycle in Fig. 4.14, and for the weaker and stronger steady state in vicinity of the Hopf bifurcations in Fig. 4.15, respectively. Here, it can be seen that strong upward motion in the boundary layer coincides with enhanced supergradient winds. Moreover, the stronger is the TC, the higher are supergradient winds, and the more dominant is the primary maximum in upward motion from lower tropospheric levels. At the lower stable state (Fig. 4.15a), the intensity of the secondary (outer) vertical wind maximum relative to that of the primary (inner) maximum is considerably higher than at the upper stable state (Fig. 4.15b). This behaviour is also reflected in a certain back-and-forth shift of the upward motion between the inner- and outer eyewall that feeds the deep convection, as can be seen by comparison of the different stages of the limit cycle (Figs. 4.12 and 4.14). Considering the evolution of the maximum supergradient wind under uniform surface cooling (Fig. 4.16) in comparison to that of maximum tangential wind (Figs. 4.8 and 4.9) provides further evidence on a link between intensity and superintensity. Beside that maximum supergradient winds decrease with v_{max} in stronger TCs, the onset of considerably enhanced fluctuations as well as a stronger trend in the decline of $(v - v_{gr})_{max}$ coincide with the bifurcation that forms the
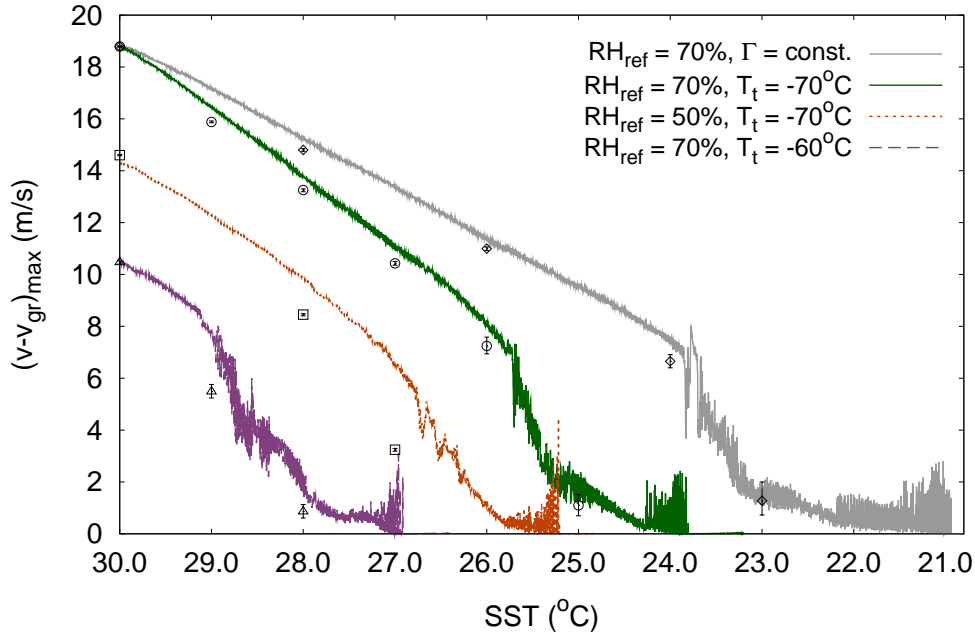
Figure 4.16: Development of maximum supergradient wind, $(v - v_{gr})_{max}$, with decreasing SST with time at a cooling rate of 10^{-3} °C/h in the standard configuration of case J (grey solid line), and case I with differing parameter values: $RH_{ref} = 70\%$ and $T_t = -70$°C (green solid line), $RH_{ref} = 50\%$ and $T_t = -70$°C (orange dotted line), and $RH_{ref} = 70\%$ and $T_t = -60$°C (purple dashed line). Average values over the last 120 h of the 4000 h-runs at fixed SSTs are plotted with different markers for case J (diamonds), case I with $RH_{ref} = 70\%$ and $T_t = -70$°C (circles), $RH_{ref} = 50\%$ and $T_t = -70$°C (squares), and $RH_{ref} = 70\%$ and $T_t = -60$°C (triangles). Error bars display the full range of maximum supergradient wind during the last 120 h of the long-term runs.

upper strong TC threshold. Hence, the assumption of gradient wind balance applied in the low-order model may be a possible reason why Hopf bifurcations as observed in HURMOD are not captured by the conceptual model.

Another possible cause for the differences in the bifurcation structure of the two models, may lie in the low-order model assumption that the potential radius of maximum winds (PRMW), given by $R = \sqrt{r^2 + 2vr/f}$ [cf. Eq. (3.1)] with $v = V_{max}$ and $r =$RMW, is an exogenous parameter, which is constant and independent of environmental conditions. As a consequence, the stronger the mature TC in the conceptual model, the smaller is its final RMW. In contrast, in the convection-resolving model HURMOD, the RMW appears to depend on the intensity of the storm in the opposite way: the higher the maximum wind speed in the mature TC stage, the larger the vertical and radial extent (referring to both the RMW and the radius of the inflow layer) of the TC. The decreasing trend of the RMW with decreasing V_{max} is clearly visible in Fig. 4.17, where the steady state RMW is plotted against V_{max} for case J at different SSTs, and several different configurations with respect to
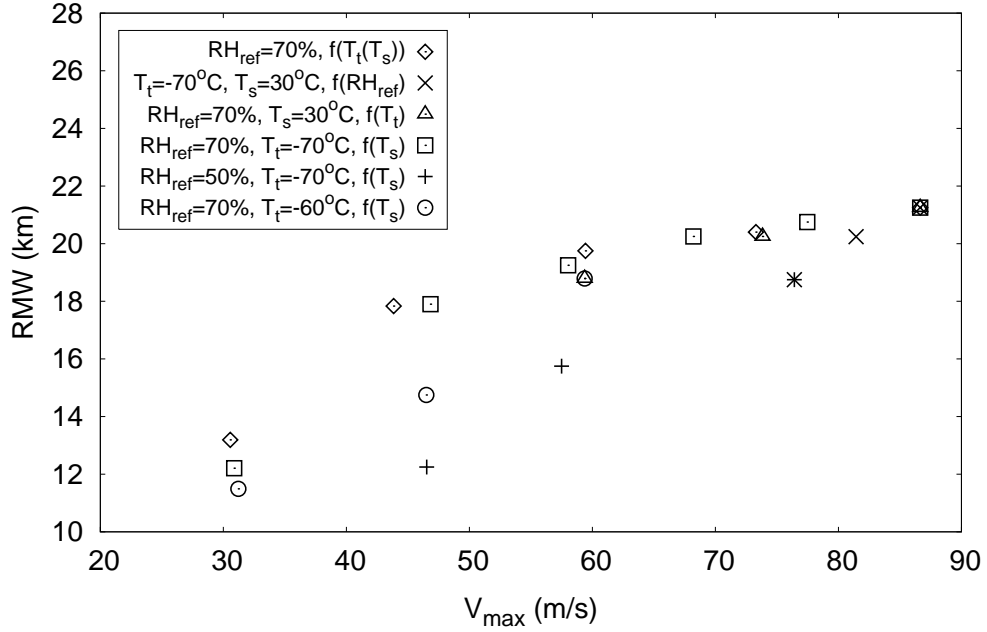
Figure 4.17: Radius of maximum wind speed (km) versus maximum horizontal wind speed (m/s) from average values over the last 120 h of the 4000 h-runs at different values for T_s and $T_t = f(T_s)$ in case J (diamonds), and case I with $T_t = -70°$C and $T_s = 30°$C for different values in RH_{ref} (crosses), $RH_{ref} = 70\%$ and $T_s = 30°$C for different values in T_t (triangles), $RH_{ref} = 70\%$ and $T_t = -70°$C for different values in T_s (squares), $RH_{ref} = 50\%$ and $T_t = -70°$C for different values in T_s (plus signs), and $RH_{ref} = 70\%$ and $T_t = -60°$C for different values in T_s (circles). Note, identical results in this plot stem from the same model experiment.

the choice of RH_{ref}, T_s and T_t for case I. Different symbols are used to depict the relation between V_{max} and the RMW under variation of each one of these three parameters with the two remaining parameters having a fix value. Thereby, it becomes apparent that the relation between the RMW and V_{max} in HURMOD depends on the environmental moisture content, surface temperature and stratification. For example, it can be seen that the RMW is more sensitive to changes in intensity induced by variation of T_s in a drier environment than in a rather moist environment.

The sensitivity of the relation between V_{max} and the RMW to the choice of environmental parameters implies that the PRMW also depends on this choice. Indeed, the sensitivity behaviour of the PRMW is qualitatively very similar to that of the RMW as becomes evident by comparison of Figs. 4.17 and 4.18. In the latter, the steady state PRMW is plotted against V_{max}, and it can be seen that for 30 m/s $\leq V_{max} <$ 90 m/s the PRMW value ranges from $\sim$ 115 km to $\sim$ 275 km. These results show that assuming the PRMW to be an independent constant parameter is very rough and infer that a prescription of the PRMW as a function
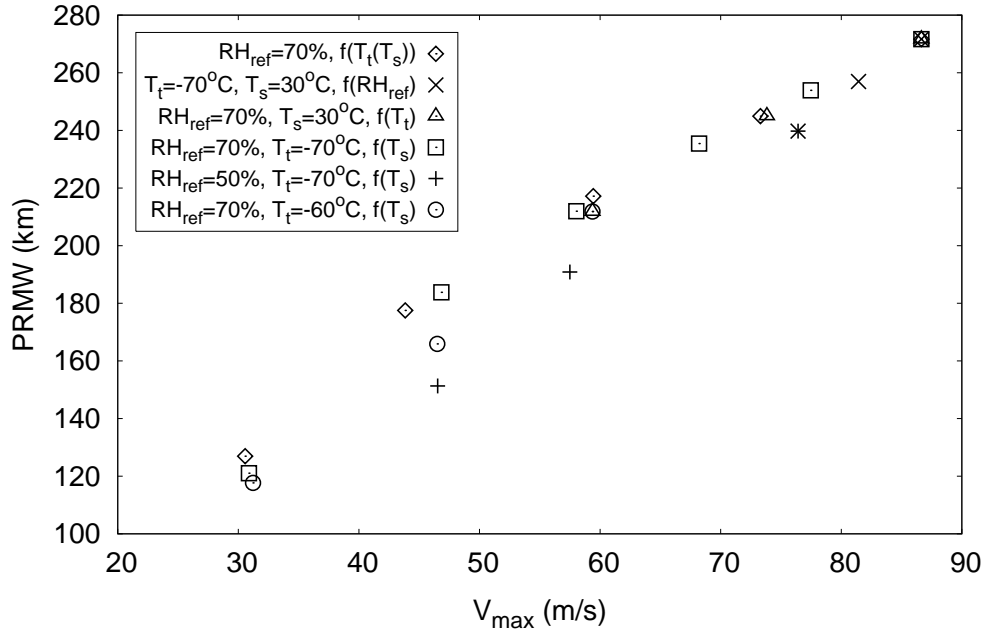
Figure 4.18: As in Fig. 4.17, but with the potential radius of maximum wind speed on the ordinate.

of the initial environmental conditions would be more appropriate. To develop a refined parameterisation of the PRMW within the low-order model, the nature of such a relation clearly needs further investigation and may be subject to a future study.

5   Conclusions and Outlook

In this study, we explored the sensitivity of potential intensity of tropical cyclones towards certain climatological parameters comprising sea surface temperature; tropospheric temperature stratification; and environmental moisture content in terms of relative humidity. These parameters, with a focus on SST, were considered as bifurcation parameters in a dynamical system approach to tropical cyclone PI. The dynamical system properties of mature tropical cyclones were investigated within two axisymmetric models of different complexity: A conceptual box-model, and the convection-resolving model HURMOD. The simplicity of the box-model allows one to compute exact diagnostic solutions by means of an eigenvalue analysis. At the same time it is inherent to the character of conceptual models that they are based on an highly idealised view. The dynamical system properties of the high-resolution model can hardly be analysed exactly, but have to be investigated experimentally. On the other hand it provides a more realistic framework in the sense that it represents a closer, less idealised approximation to the natural phenomenon.

5.1   Conclusions

Results of both models exhibit that the mature stage of a strong tropical cyclone has the character of a fixed point attractor, where the final state is independent of the size and strength of the initial disturbance above a certain threshold. Moreover, TC intensity as well as the critical initial vortex strength necessary for TC formation, are sensitive to tropospheric humidity and temperature lapse rate. The steeper the lapse rate and the more humid the air, the lower is the amplitude threshold to cyclogenesis and the higher is the maximum intensity of the modelled TCs. A larger difference between the SST and the outflow temperature of TCs at upper tropospheric levels, implies both a higher thermodynamic efficiency resulting in an enhanced intensity and a reduced static stability facilitating convection (Wada et al., 2012). Further hints to the possibility that among the thermodynamic control factors not merely SST is relevant to TC activity is given in a recent study by Emanuel et al. (2013). Their analysis of observational and reanalysis data shows that changes in TC activity over the North Atlantic are highly correlated to temperature changes in the upper troposphere. The sensitivity to temperature stratification found in both models is also in accordance with the observed nonlocal response of TC intensity over the North Atlantic found by Swanson (2008). Regarding intensity, results from HURMOD simulations suggest that the temperature stratification plays a more important role than environmental relative humidity. In the box-model this tendency is even more pronounced. On the other hand, environmental relative humidity appears to be highly relevant to the frequency of occurrence of TCs, which agrees

with results from previous modelling and observational studies (Gray, 1979; Zhao and Held, 2012). Furthermore, the results from both models show that the value of the critical sea surface temperature, above which tropical cyclones of hurricane strength may occur, is shifted towards higher values with increasing tropopause temperature; decreasing tropospheric temperature lapse rate; and decreasing environmental moisture content. A similar behaviour of the sea surface temperature threshold in response to upper tropospheric level warming has also been noted by Holland (1997) and Henderson-Sellers et al. (1998). Overall, these results hint to a dependence of the SST threshold for cyclogenesis on the global and regional climate state.

Though the two models are in good qualitative agreement with regard to the parameter sensitivity trends investigated herein, there are notable differences in their bifurcation structures. Within a tropical ocean range of sea surface temperatures, the dynamical system constituting the conceptual model exhibits at least two non-trivial equilibria, an attractor and a repellor. A cusp catastrophe arises at a certain SST and relative humidity, where the stable equilibrium splits into two stable, and one unstable equilibrium giving rise to a bistability. The additional repellor poses a strong obstruction to cyclogenesis, providing a possible explanation, why not all initial disturbances can transform into strong TCs. For relatively high SSTs, however, there remains only one stable and one unstable equilibrium, which is very close to the state of rest. Hence, in this regime the amplitude threshold quasi disappears in the box-model. On the other hand, in HURMOD a considerable amplitude threshold seems to exist throughout the investigated parameter range. Moreover, the investigation of the dynamical system properties of HURMOD in response to changes in the sea surface temperature point to the existence of a Hopf bifurcation instead of a bistability. Below a certain SST, the fixed point attractor associated with a strong TC turns to a limit cycle attractor; then a second Hopf bifurcation arises at a slightly lower SST, where the limit cycle attractor gives way to a fixed point attractor; before the system becomes chaotic and finally unstable at lower SSTs. As noted above, the SST range within which the bifurcations are observed, is strongly sensitive to the tropospheric temperature lapse rate. Furthermore, the existence of the Hopf bifurcations is found to depend on the environmental moisture content in HURMOD. In a drier environment they seem to disappear. Presuming a moist-neutral environment (case N), HURMOD does not exhibit any bifurcations within the range of tropical SSTs. Furthermore, in case N the intensity is found to be enhanced in a drier environment, rather than the other way round, which would be more realistic. Therefore, we conclude that the moist-neutral assumption in case N results in a rather unrealistic behaviour of the modelled TC, compared to that in the non-neutral cases I and J.

Apart from the generally higher susceptibility to the occurrence of small-scale fluctuations in HURMOD, Hopf bifurcations do not occur in the low-order model, and in contrast to HURMOD, strong TCs can develop from very small disturbances close to the state of rest in the conceptual model, given that the environmental moisture and temperature conditions are sufficiently favourable. At this point, we can indicate two principal differences in the conception of the low-order model and HURMOD, which may possibly be responsible for these structural differences among the two models: In the conceptual model, 1) the PRMW is considered as constant and independent of initial conditions, and 2) the assumption that the vortex is in gradient wind balance is made. In contrast, in HURMOD, considerable supergradient winds arise in strong TCs, which agrees with findings by Bryan and Rotunno (2009b). Furthermore, the comparison of steady state results from different model configurations reveals that the PRMW displays a decreasing tendency with decreasing maximum intensity in HURMOD. The tendency itself appears to be sensitive to the initial tropospheric temperature and moisture conditions in HURMOD. Consequently, we expect that the consideration of a parameterisation for the PRMW as a function of the thermodynamic reference state in the low-order model would result in a better agreement among the two models of different complexity.

5.2   Outlook

One of the unresolved issues of this study is concerning the question, whether either the radius of maximum winds or the potential radius of maximum winds can be determined as a function of environmental parameters. If such a relation exists, it will probably provide an important key to a more realistic closure of the conceptual model presented herein as well as of other theoretical models formulated within an axisymmetric framework, in which the interdependency of maximum tangential wind and RMW via angular momentum plays a crucial role. Another interesting question addresses the possible advancement of conceptual TC models, when one includes the effect of supergradient winds. With regard to both of these issues, the scale dependence of tropical cyclones detected by Frisius et al. (2013) by application of a slab-boundary layer model within the theoretical PI model by Emanuel, and some hints to the existence of a link between the RMGW and superintensity, combined with the findings of Bryan and Rotunno (2009a) and of this study, which show that maximum supergradient winds rise with maximum gradient winds, appear to be interesting. A possible way to incorporate superintensity due to the deviation from gradient wind balance may consist in that the surface pressure occurring in the expression for surface saturation entropy is formulated on the basis of an unbalanced boundary layer flow, instead of gradient wind balance as pointed out by Frisius and Schönemann (2012).

With regard to the possible climate state dependence of the SST threshold, it would be certainly interesting to test the validity of the respective tendencies found in the study at hand in a more sophisticated 3-D model, or in global circulation models. Apart from this, the research opportunities related to the phenomenon of TCs generally appear to be most manifold, as the description of this phenomenon covers nearly all subjects in meteorology (Ooyama, 1982).

Appendix: Software tools

This document was written and prepared in the typesetting system LaTeX, and edited with Kile 2.0.85.

The conceptual model introduced in chapter 3, is written in FORTRAN and can be compiled with gcc version 4.4.5, among other gcc versions. The subroutine DGEEV of the LAPACK (Linear Algebra PACKage) library is used for the computation of the Eigenvalues in the stability analysis of the conceptual model.

The convection-resolving model HURMOD is written in FORTRAN. The code is parallel, and has been compiled with different f90-compilers, using different versions of OpenMPI (Open Message Passing Interface) libraries, because the HURMOD simulations had to be carried out on different computer clusters. Among the different OpenMPI libraries, used herein, are openmpi 1.6.4 for gcc and openmpi/1.6.2-gccsys. Note, the format of output data varied. For restarts on a different cluster, some of the output had to be converted from big endian to little endian.

The graphical Open Source scripting programme gnuplot 4.4.0 has been used to visualise the output of the conceptual model (see chapter 3), and part of the output from HURMOD (see chapter 4). To visualise HURMOD data in the two-dimensional plots shown in chapter 4, the Open Source scripting language GrADS (Grid Analysis and Display System) was used (versions 2.x). Figure 1.1, 2.1, and 3.1 were drawn "manually" in different versions of LibreOffice and OpenOffice Impress, and converted to eps-Format in the Open Source graphic programme Gimp (Gnu Image Manipulation Programme).

Bibliography

Anthes, R. A., 1982: *Tropical Cyclones. Their Evolution, Structure and Effects.* Am. Meteorol. Soc., Boston, 208 pp.

Bengtsson, L., K. I. Hodges, M. Esch, N. Keenlyside, L. Kornblueh, J.-J. Luo, and T. Yamagata, 2007: How may tropical cyclones change in a warmer climate? *Tellus*, **59A**, 539–561.

Bister, M. and K. A. Emanuel, 1998: Dissipative Heating and Hurricane Intensity. *Meteorol. Atmos. Phys.*, **65**, 233–240.

Bister, M. and K. A. Emanuel, 2002: Low frequency variability of tropical cyclone potential intensity. 1. Interannual to interdecadal variability. *J. Geophys. Res.*, **107(D24)**, 4801, doi:10.1029/2001JD000776.

Black, A. K., et al., 2007: Air-Sea Exchange in Hurricanes. Synthesis of Observations from the Coupled Boundary Layer Air-Sea Transfer Experiment. *Bull. Amer. Meteor. Soc.*, **88**, 357–374.

Blackadar, A. K., 1962: The Vertical Distribution of Wind and Turbulent Exchange in a Neutral Atmospher. *J. Geophys. Res.*, **67**, 3095–3102.

Bogner, P. B., G. M. Barnes, and J. L. Franklin, 2000: Conditional Instability and Shear for Six Hurricanes over the Atlantic Ocean. *Weather and Forcasting*, **15**, 192–207.

Bryan, G. H., 2008: On the Computation of Pseudoadiabatic Entropy and Equivalent Potential Temperature. *Monthly Weather Review*, **136**, 5239–5245.

Bryan, G. H. and J. M. Fritsch, 2002: A Benchmark Simulation for Moist Nonhydrostatic Numerical Models. *Monthly Weather Review*, **130**, 2917–2928.

Bryan, G. H. and R. Rotunno, 2009a: Evaluation of an Analytical Model for the Maximum Intensity of Tropical Cyclones. *J. Atmos. Sci.*, **66**, 3042–3060.

Bryan, G. H. and R. Rotunno, 2009b: The Influence of Near-Surface, High-Entropy Air in Hurricane Eyes on Maximum Hurricane Intensity. *J. Atmos. Sci.*, **66**, 148–158.

Bryan, G. H. and R. Rotunno, 2009c: The Maximum Intensity of Tropical Cyclones in Axisymmetric Numerical Model Simulations. *Monthly Weather Review*, **137**, 1770–1789.

Camargo, S. J., M. Ting, and Y. Kushnir, 2013: Influence of local and remote SST on North Atlantic tropical cyclone potential intensity. *Climate Dynamics*, **40**, 1515–1529, doi: 10.1007/s00382-012-1536-4.

Camp, J. P. and M. T. Montgomery, 2001: Hurricane Maximum Intensity: Past and Present. *J. Atmos. Sci.*, **129**, 1704–1717.

Carrier, G. F., A. L. Hammond, and O. D. George, 1971: A model of the mature hurricane. *J. Fluid Mech.*, **47**, 145–170.

Charney, J. G. and A. Eliassen, 1964: On the Growth of the Hurricane Depression. *J. Atmos. Sci.*, **21**, 68–74.

Chavas, D. R. and K. A. Emanuel, 2010: A QuikSCAT climatology of tropical cyclone size. *Geophys. Res. Lett.*, **37**, L18 816, doi:10.1029/2010GL044558.

Craig, G. C. and S. L. Gray, 1996: CISK or WISHE as the Mechanism for Tropical Cyclone Intensification. *J. Atmos. Sci.*, **53**, 3528–3540.

DeMott, C. A. and D. A. Randall, 2004: Observed variations of tropical convective available potential energy. *J. Geophys. Res.*, **109**, D02 102, doi:10.1029/2003JD003784.

Emanuel, K. A., 1986: An Air-Sea Interaction Theory for Tropical Cyclones. Part I: Steady-State Maintenance. *J. Atmos. Sci.*, **43**, 585–604.

Emanuel, K. A., 1988: The Maximum Intensity of Hurricanes. *J. Atmos. Sci.*, **45**, 1143–1155.

Emanuel, K. A., 1989: The Finite-Amplitude Nature of Tropical Cyclogenesis. *J. Atmos. Sci.*, **46**, 3431–3456.

Emanuel, K. A., 1994: *Atmospheric Convection*. Oxford University Press, Inc., 592 pp.

Emanuel, K. A., 1995a: Sensitivity of tropical cyclones to surface exchange coefficients and a revised steady-state model incorporating eye dynamics. *J. Atmos. Sci.*, **52**, 3969–3976.

Emanuel, K. A., 1995b: The Behaviour of a Simple Hurricane Model Using a Convective Scheme Based on Subcloud-Layer Entropy Equilibrium. *J. Atmos. Sci.*, **52**, 3960–3968.

Emanuel, K. A., 1997: Some Aspects of Hurricane Inner-core Dynamics and Energetics. *J. Atmos. Sci.*, **54**, 1014–1026.

Emanuel, K. A., 2003: Tropical Cyclones. *Annu. Rev. Earth Planet. Sci.*, **31**, 75–104.

Emanuel, K. A. and D. S. Nolan, 2004: Tropical Cyclone Activity and the Global Climate System. *The 26th Conference on Hurricanes and Tropical Meteorology.*

Emanuel, K. A. and R. Rotunno, 2011: Self-Stratification of Tropical Cyclone Outflow. Part I: Implications for Storm Structure. *J. Atmos. Sci.*, **68**, 2236–2249.

Emanuel, K. A., S. Solomon, D. Folini, S. Davies, and C. Cagnazzo, 2013: Influence of Tropical Tropopause Layer Cooling on Atlantic Hurricane Activity. *J. Climate*, **26**, 2288–2301.

Etling, D., 2008: *Theoretische Meteorologie: eine Einführung*. Springer-Verlag, 388 pp.

Fairall, C. W., E. F. Bradley, J. E. Hare, A. A. Grachev, and J. B. Edson, 2003: Bulk Parameterization of Air-Sea Fluxes: Updates and Verification for the COARE Algorithm. *J. Climate*, **16**, 571–591.

Frank, W. M., 1977: The Structure and Energetics of the Tropical Cyclone. I. Storm Structure. *Monthly Weather Review*, **105**, 1119–1135.

Frisius, T., 2005: An atmospheric balanced model of an axisymmetric vortex with zero potential vorticity. *Tellus*, **57A**, 55–64.

Frisius, T. and T. Hasselbeck, 2009: The effect of latent cooling processes in tropical cyclone simulations. *Q. J. R. Meteorol. Soc.*, **135**, 1732–1749.

Frisius, T. and D. Schönemann, 2012: An Extended Model for the Potential Intensity of Tropical Cyclones. *J. Atmos. Sci.*, **69**, 641–661.

Frisius, T., D. Schönemann, and J. Vigh, 2013: The Impact of Gradient Wind Imbalance on Potential Intensity of Tropical Cyclones in an Unbalanced Slab Boundary Layer Model. *J. Atmos. Sci.*, **70**, 1874–1890.

Frisius, T. and U. Wacker, 2007: Das massenkonsistente axialsymmetrische Wolkenmodell HURMOD. *Deutscher Wetterdienst, Arbeitsergebnisse*, **85**, 42pp.

Fu, R., A. D. D. Genio, and W. B. Rossow, 1994: Influence of Ocean Surface Conditions on Atmospheric Vertical Thermodynamic Structure and Deep Convection. *J. Climate*, **7**, 1092–1108.

Gray, W. M., 1962: On the balance of forces and radial accelerations in hurricanes. *Q. J. R. Meteorol. Soc.*, **88**, 430–458.

Gray, W. M., 1968: Global View of the Origin of Tropical Disturbances and Storms. *Monthly Weather Review*, **96**, 669–700.

Gray, W. M., 1979: Hurricanes: their formation, structure and likely role in the tropical circulation. *Meteorology over the Tropical Oceans*, D. B. Shaw, Ed., Royal Meteorological Society, James Glaisher House, Grenville Place, Bracknell, Berkshire, 155–218.

Hansen, J., A. Lacis, D. Rind, G. Russell, and P. Stone, 1984: Climate sensitivity: Analysis of feedback mechanisms. *Climate Processes and Climate Sensitivity, AGU Geophysical Monograph 29, Maurice Ewing Vol. 5*, J. E. Hansen and T. Takahashi, Eds., American Geophysical Union, 130–163.

Hegerl, G. C., F. W. Zwiers, P. Braconnot, N. P. Gillett, Y. Luo, and co authors, 2007: Understanding and attributing climate change. *Climate Change 2007: The Physical Science Basis. Contribution of Working Group I to the Fourth Assessment Report of the Intergovernmental Panel on Climate Change*, S. Solomon, D. Qin, M. Manning, Z. Chen, M. Marquis, K. B. Averyt, M. Tignor, and H. L. Miller, Eds., Cambridge University Press, Cambridge, United Kingdom and New York, NY, USA.

Henderson-Sellers, A., et al., 1998: Tropical Cyclones and Global Climate Change: A Post-IPCC Assessment. *Bull. Amer. Meteor. Soc.*, **79**, 19–38.

Hill, K. A. and G. M. Lackmann, 2009: Influence of Environmental Humidity on Tropical Cyclone Size. *Monthly Weather Review*, **137**, 3294–3315.

Holland, G. J., 1980: An Analytic Model of the Wind and Pressure Profiles in Hurricanes. *Monthly Weather Review*, **108**, 1212–1218.

Holland, G. J., 1997: The Maximum Potential Intensity of Tropical Cyclones. *J. Atmos. Sci.*, **54**, 2519–2541.

Holton, J. R., 2004: *An Introduction to Dynamic Meteorology*. Academic Press, Inc., 535 pp.

Hughes, L. A., 1952: On the Low-Level Wind Structure of Tropical Storms. *J. Meteor.*, **9**, 422–428.

Jordan, C. L., 1958: Mean soundings for the West Inidies area. *J. Meteor.*, **15**, 91–97.

Kepert, J. D., 2010a: Slab- and height-resolving models of the tropical cyclone boundary layer. Part I: Comparing the simulations. *Q. J. R. Meteorol. Soc.*, **136**, 1686–1699.

Kepert, J. D., 2010b: Slab- and height-resolving models of the tropical cyclone boundary layer. Part II: Why the simulations differ. *Q. J. R. Meteorol. Soc.*, **136**, 1700–1711.

Kepert, J. D., 2012: Choosing a Boundary Layer Parameterization for Tropical Cyclone Modeling. *Monthly Weather Review*, **140**, 1427–1445.

Kleinschmidt, E., 1951: Grundlagen einer Theorie der tropischen Zyklonen. *Meteorol. Atmos. Phys.*, **4**, 53–72.

Knaff, J. A., M. DeMaria, C. R. Sampson, J. E. Peak, J. Cummings, and W. H. Schubert, 2013: Upper Oceanic Energy Response to Tropical Cyclone Passage. *J. Climate*, **26**, 2631–2650.

Kraus, H., 2004: *Die Atmosphähre der Erde. Eine Einführung in die Meteorologie*. Springer-Verlag, Berlin Heidelberg, 422 pp.

Ma, Z., J. Fei, L. Liu, X. Huang, and X. Cheng, 2013: Effects of the Cold Core Eddy on Tropical Cyclone Intensity and Structure under Idealized Air-Sea Interaction Conditions. *Monthly Weather Review*, **141**, 1285–1303.

Malkus, J. S., 1958: On the Structure and Maintenance of the Mature Hurricane Eye. *J. Meteor.*, **15**, 337–349.

Mallen, K. J., M. T. Montgomery, and B. Wang, 2005: Reexamining the Near-Core Radial Structure of the Tropical Cyclone Primary Circulation: Implications for Vortex Resiliency. *J. Atmos. Sci.*, **62**, 408–425.

Mann, M. E. and K. A. Emanuel, 2006: Atlantic Hurricane Trends Linked to Climate Change. *Eos*, **87**, 233–235.

Mei, W. and C. Pasquero, 2013: Spatial and Temporal Characterization of Sea Surface Temperature Response to Tropical Cyclones. *J. Climate*, **26**, 3745–3765.

Miller, B. I., 1958: On the Maximum Intensity of Hurricanes. *J. Meteor.*, **15**, 184–195.

Ooyama, K., 1969: Numerical simulation of the life cycle of tropical cyclones. *J. Atmos. Sci.*, **26**, 3–40.

Ooyama, K. V., 1982: Conceptual Evolution of the Theory and Modelling of the Tropical Cyclone. *J. Meteorol. Soc. Japan*, **60**, 369–379.

Persing, J. and M. T. Montgomery, 2003: Hurricane Superintensity. *J. Atmos. Sci.*, **60**, 2349–2371.

Reed, K. A. and C. Jablonowski, 2011: An Analytic Vortex Initialization Technique for Idealized Tropical Cyclone Studies in AGCMs. *Monthly Weather Review*, **139**, 689–710.

Riehl, H., 1948: A radiosonde observation in the eye of a hurricane. *Q. J. R. Meteorol. Soc.*, **74**, 194–196.

Riehl, H., 1950: A Model of Hurricane Formation. *J. Appl. Phys.*, **21**, 917–925.

Rosenthal, S. L., 1978: Numerical Simulation of Cyclone Development with Latent Heat Release by the Resolvable Scales I: Model Description and Preliminary Results. *J. Atmos. Sci.*, **35**, 258–271.

Rotunno, R. and G. H. Bryan, 2012: Effects of Parameterized Diffusion on Simulated Hurricanes. *J. Atmos. Sci.*, **69**, 2284–2299.

Rotunno, R. and K. Emanuel, 1987: An Air-Sea Interaction Theory for Tropical Cyclones. Part II: Evolutionary Study Using a Nonhydrostatic Axisymmetric Numerical Model. *J. Atmos. Sci.*, **44**, 542–561.

Schönemann, D. and T. Frisius, 2012: Dynamical system analysis of a low-order tropical cyclone model. *Tellus A*, **64**, 15 817, doi:10.3402/tellusa.v64i0.15817.

Schönemann, D. and T. Frisius, 2014: Dynamical system properties of an axisymmetric convective tropical cyclone model. *Tellus A*, **66**, 22 456, doi:10.3402/tellusa.v66.22456.

Schubert, W. H. and J. J. Hack, 1983: Transformed Eliassen Balanced Vortex Model. *J. Atmos. Sci.*, **40**, 1571–1583.

Sheets, R. C., 1969: Some Mean Hurricane Soundings. *J. Appl. Meteorol.*, **8**, 134–146.

Smith, R. K., 1980: Tropical Cyclone Eye Dynamics. *J. Atmos. Sci.*, **37**, 1227–1232.

Smith, R. K., 2003: A simple model of the hurricane boundary layer. *Q. J. R. Meteorol. Soc.*, **129**, 1007–1027.

Smith, R. K. and M. T. Montgomery, 2008: Balanced boundary layers used in hurricane models. *Q. J. R. Meteorol. Soc.*, **134**, 1385–1395.

Smith, R. K., M. T. Montgomery, and S. Vogl, 2008: A critique of Emanuels hurricane model and potential intensity theory. *Q. J. R. Meteorol. Soc.*, **134**, 551–561.

Swanson, K. L., 2008: Nonlocality of Atlantic tropical cyclone intensities. *Geochem. Geophys. Geosyst.*, **9**, Q04V01, doi:10.1029/2007GC001844.

Tang, B. and K. Emanuel, 2010: Midlevel Ventilations Constraint on Tropical Cyclone Intensity. *J. Atmos. Sci.*, **67**, 1817–1830.

Tang, B. and K. Emanuel, 2012a: A Ventilation Index for Tropical Cyclones. *Bull. Amer. Meteor. Soc.*, **93**, 1901–1912.

Tang, B. and K. Emanuel, 2012b: Sensitivity of Tropical Cyclone Intensity to Ventilation in an Axisymmetric Model. *J. Atmos. Sci.*, **69**, 2394–2413.

Wada, A., N. Usui, and K. Sato, 2012: Relationship of maximum tropical cyclone intensity to sea surface temperature and tropical cyclone heat potential in the North Pacific Ocean. *J. Geophys. Res.*, **117**, D11 118, doi:10.1029/2012JD017583.

Wang, Y., 2009: How Do Outer Spiral Rainbands Affect Tropical Cyclone Structure and Intensity? *J. Atmos. Sci.*, **66**, 1250–1273.

Wang, Y. and J. Xu, 2010: Energy Production, Frictional Dissipation, and Maximum Intensity of a Numerically Simulated Tropical Cyclone. *J. Atmos. Sci.*, **67**, 97–116.

Willoughby, H. E., H.-L. Jin, S. J. Lord, and J. M. Piotrowicz, 1984: Hurricane Structure and Evolution as Simulated by an Axisymmetric, Nonhydrostatic Numerical Model. *J. Atmos. Sci.*, **41**, 1169–1186.

Wirth, V. and T. J. Dunkerton, 2009: The Dynamics of Eye Formation and Maintenance in Axisymmetric Diabatic Vortices. *J. Atmos. Sci.*, **66**, 3601–3620.

Xu, J. and Y. Wang, 2010: Sensitivity of the Simulated Tropical Cyclone Inner-Core Size to the Initial Vortex Size. *Monthly Weather Review*, **128**, 4135–4157.

Yamasaki, 1975: A Numerical Experiment of the Interaction between Cumulus Convection and Larger-Scale Motion. *Pap. Meteor. Geophys.*, **26**, 63–91.

Yamasaki, 1977: A Preliminary Experiment of the Tropical Cyclone without Parameterizing the Effects of Cumulus Convection. **55**, 11–30.

Yanase, W., M. Satoh, H. Taniguchi, and H. Fujinami, 2012: Seasonal and Intraseasonal Modulation of Tropical Cyclogenesis Environment over the Bay of Bengal during the Extended Summer Monsoon. *J. Climate*, **25**, 2914–2930.

Yu, J., Y. Wang, and K. Hamilton, 2010: Response of Tropical Cyclone Potential Intensity to a Global Warming Scenario in the IPCC AR4 CGCMs. *J. Climate*, **23**, 1354–1373.

Zeng, Z., L. Chen, and Y. Wang, 2008: An Observational Study of Environmental Dynamical Control of Tropical Cyclone Intensity in the Atlantic. *Monthly Weather Review*, **136**, 3307–3322.

Zeng, Z., Y. Wang, and C.-C. Wu, 2007: Environmental Dynamical Control of Tropical Cyclone Intensity - An Observational Study. *Monthly Weather Review*, **135**, 38–59.

Zhang, J. A., F. D. Marks, M. Montgomery, and S. Lorsolo, 2011: An Estimation of Turbulent Characteristics in the Low-Level Region of Intense Hurricanes Allen (1980) and Hugo (1989). *Monthly Weather Review*, **139**, 1447–1462.

Zhang, J. A. and M. Montgomery, 2012: Observational Estimates of the Horizontal Eddy Diffusivity and Mixing Length in the Low-Level Region of Intense Hurricanes. *J. Atmos. Sci.*, **69**, 1306–1316.

Zhao, M. and I. M. Held, 2012: TC-Permitting GCM Simulations of Hurricane Frequency Response to Sea Surface Temperature Anomalies Projected for the Late-Twenty-First Century. *J. Climate*, **25**, 2995–3009.

Zhao, M., I. M. Held, S.-J. Lin, and G. A. Vecchi, 2009: Simulations of Global Hurricane Climatology, Interannual Variability, and Response to Global Warming Using a 50-km Resolution GCM. *J. Climate*, **22**, 6653–6678.

Danksagung

Zunächst möchte ich mich ganz herzlich bei meinem Doktorvater, Thomas Frisius, für die Unterstützung und Zusammenarbeit der vergangenen vier Jahre bedanken, die von Anfang an von gegenseitiger Wertschätzung, ehrlichem Respekt und wachsendem Vertrauen geprägt war. Ich glaube, einen besseren Doktorvater kann man sich nicht wünschen und hoffe daher, dass er sich mit meiner Adoption ebenfalls glücklich schätzt. Desweiteren möchte ich mich ebenso herzlich bei meinem Kollegen, Joachim Pelkowski, für zahlreiche Diskussionen und Gespräche und seine ebenso scharfe wie konstruktive Kritik bedanken. Ich hoffe, dass wir auch zukünftig noch das eine oder andere Mal die Mittagspause miteinander teilen werden. Außerdem möchte ich mich bei allen Mitarbeitern des SICSS-Office für ihre freundliche Art und die praktische und nach Möglichkeit unbürokratische Unterstützung, die ich durch sie in den letzten Jahren erfahren habe, bedanken.

Bei meinen Eltern bedanke ich mich für ihre warme, herzliche Art und das sichere Gefühl, immer willkommen zu sein, sowie dafür, dass sie mir zwei Geschwister als Freunde mitgegeben haben, die sich gegenseitig stützen. Schließlich will ich mich bei dem Mann bedanken, der nun schon seit einigen Jahren bereitwillig sein Leben mit mir teilt. Danke für Deine liebevolle Zuneigung, Deine Geduld und Deine emotionale Unterstützung, die mir nicht zuletzt half, die Ruhe und die Kraft aufzubringen, um dies hier zu Ende zu führen.